

# **Probing thermalization and deuteron production mechanism via fluctuations in heavy-ion collisions in STAR at RHIC.**

*By*

**DEBASISH MALLICK**

PHYS11201604003

**National Institute of Science Education and Research,  
Bhubaneswar**

*A thesis submitted  
to the Board of Studies in  
School of Physical Sciences*

*In partial fulfillment of requirements  
For the Degree of*

**DOCTOR OF PHILOSOPHY**

*of*

**HOMI BHABHA NATIONAL INSTITUTE**



**March, 2023**



# Homi Bhabha National Institute

## Recommendations of the Viva Voce Committee

As members of the Viva-Voce Committee, we certify that we have read the dissertation prepared by **Debasish Mallick** entitled “**Probing thermalization and deuteron production mechanism via fluctuations in heavy-ion collisions in STAR at RHIC.**” and recommend that it may be accepted as fulfilling the thesis requirement for the award of Degree of Doctor of Philosophy.

Signature:

Chairman - Prof. Sanjay Kumar Swain

Date:

31.03.2023

Signature:

Guide / Convener - Prof. Bedangadas Mohanty

Date:

31.03.2023

Signature:

Member 1 - Dr. Prolay Kumar Mal

Date:

31.03.2023

Signature:

Member 2 - Dr. Victor Roy

Date:

31.03.2023

Signature:

Member 3 - Dr. Arun Kumar Nayak

Date:

31.03.2023

Signature:

External Examiner - Prof. Basanta K. Nandi (IIT Mumbai)

Date:

31.03.2023

Final approval and acceptance of this thesis are contingent upon the candidate's submission of the final copies of the thesis to HBNI.

I/We hereby certify that I/We have read this thesis prepared under my/our direction and recommend that it may be accepted as fulfilling the thesis requirement.

Date : March 31, 2023

Place : Bhubaneswar

*Bedangadas Mohanty*

(Guide)

## **STATEMENT BY THE AUTHOR**

This dissertation has been submitted in partial fulfillment of requirements for an advanced degree at Homi Bhabha National Institute (HBNI) and is deposited in the library to be made available to borrowers under the rules of the HBNI.

Brief quotations from this dissertation are allowable without special permission, provided that accurate acknowledgment of the source is made. Requests for permission for extended quotation from or reproduction of this manuscript in whole or in part may be granted by the Competent Authority of HBNI when in his or her judgment the proposed use of the material is in the interests of scholarship. In all other instances, however, permission must be obtained from the author.

**Date** : March 31, 2023

**Place** : Bhubaneswar

  
(DEBASISH MALLICK)

## DECLARATION

I hereby declare that the investigation presented in the thesis has been carried out by me. The work is original and has not been submitted earlier as a whole or in part for a degree/diploma at this or any other Institution/University.

**Date** : March 31, 2023

**Place** : Bhubaneswar

  
(DEBASISH MALLICK)

# List of publications arising from the thesis

## Journal

### Published

- [1] Sourendu Gupta, Debasish Mallick, Dipak Kumar Mishra, et al. “Limits of thermalization in relativistic heavy ion collisions”. *Phys. Lett. B* 829 (2022), 137021.
- [2] Ashish Pandav, Debasish Mallick, and Bedangadas Mohanty. “Effect of limited statistics on higher order cumulants measurement in heavy-ion collision experiments”. *Nucl. Phys. A* 991 (2019), 121608. arXiv: [1809.08892 \[nucl-ex\]](#).
- [3] Ashish Pandav, Debasish Mallick, and Bedangadas Mohanty. “Search for the QCD critical point in high energy nuclear collisions”. *Prog. Part. Nucl. Phys.* 125 (2022), 103960. arXiv: [2203.07817 \[nucl-ex\]](#).

### Communicated

- [1] STAR Collaboration (PAs: Debasish Mallick, Nu Xu, and Bedangadas Mohanty). “Collision-energy Dependence of Deuteron Cumulants and Proton-deuteron Correlations in Au+Au collisions at RHIC” (Apr. 2023). arXiv: [2304.10993 \[nucl-ex\]](#).

## Analysis note in the STAR experiment

- [1] Debasish Mallick, Nu Xu, and Bedangadas Mohanty. *STAR Analysis Note of “Collision energy dependence of deuteron cumulants and proton-deuteron correlations in Au+Au collisions at RHIC”*,

(Paper draft under review in the STAR collaboration), PSN0796. [https://www.star.bnl.gov/protected/bulkcorr/dmallick/WebPage\\_Deuteron\\_analysisnote/Analysis\\_note\\_Deuteron\\_Fluctuation\\_v2.pdf](https://www.star.bnl.gov/protected/bulkcorr/dmallick/WebPage_Deuteron_analysisnote/Analysis_note_Deuteron_Fluctuation_v2.pdf).

## Conference proceedings

- [1] Debasish Mallick. “Deuteron Fluctuations and Proton–Deuteron Correlations from the STAR Experiment at  $\sqrt{s_{NN}} = 7.7\text{--}200$  GeV”. *Acta Phys. Polon. Supp.* 16.1 (2023), 80.
- [2] Sourendu Gupta, Debasish Mallick, Dipak K. Mishra, et al. “Probing thermal nature of matter formed at RHIC via fluctuations”. *Nucl. Phys. A* 1005 (2021). Ed. by Feng Liu, Enke Wang, Xin-Nian Wang, et al., 121987.
- [3] Debasish Mallick. “Measurement of Higher Moments of Net-particle Distributions in STAR”. *Springer Proc. Phys.* 261 (2021). Ed. by Prafulla Kumar Behera, Vipin Bhatnagar, Prashant Shukla, et al., 1093–1097.

## Other publications

- [1] Mohamed Abdallah et al. “Cumulants and correlation functions of net-proton, proton, and antiproton multiplicity distributions in Au+Au collisions at energies available at the BNL Relativistic Heavy Ion Collider”. *Phys. Rev. C* 104.2 (2021), 024902. arXiv: [2101.12413](https://arxiv.org/abs/2101.12413) [nucl-ex].
- [2] J. Adam et al. “Nonmonotonic Energy Dependence of Net-Proton Number Fluctuations”. *Phys. Rev. Lett.* 126.9 (2021), 092301. arXiv: [2001.02852](https://arxiv.org/abs/2001.02852) [nucl-ex].
- [3] M. S. Abdallah et al. “Measurements of Proton High Order Cumulants in  $\sqrt{s_{NN}} = 3$  GeV Au+Au Collisions and Implications for the QCD Critical Point”. *Phys. Rev. Lett.* 128.20 (2022), 202303. arXiv: [2112.00240](https://arxiv.org/abs/2112.00240) [nucl-ex].
- [4] Mohamed Abdallah et al. “Measurement of the Sixth-Order Cumulant of Net-Proton Multiplicity Distributions in Au+Au Collisions at  $\sqrt{s_{NN}} = 27, 54.4,$  and 200 GeV at RHIC”. *Phys. Rev. Lett.* 127.26 (2021), 262301. arXiv: [2105.14698](https://arxiv.org/abs/2105.14698) [nucl-ex].

- [5] M. S. Abdallah et al. “Probing strangeness canonical ensemble with  $K^-$ ,  $\phi(1020)$  and  $\Xi^-$  production in Au+Au collisions at  $\sqrt{s_{NN}}=3$  GeV”. *Phys. Lett. B* 831 (2022), 137152. arXiv: [2108.00924 \[nucl-ex\]](#).
- [6] M. S. Abdallah et al. “Light nuclei collectivity from  $\sqrt{s_{NN}} = 3$  GeV Au+Au collisions at RHIC”. *Phys. Lett. B* 827 (2022), 136941. arXiv: [2112.04066 \[nucl-ex\]](#).
- [7] M. S. Abdallah et al. “Disappearance of partonic collectivity in  $\sqrt{s_{NN}}=3$  GeV Au+Au collisions at RHIC”. *Phys. Lett. B* 827 (2022), 137003. arXiv: [2108.00908 \[nucl-ex\]](#).
- [8] Mohamed Abdallah et al. “Measurements of  $H_{\Lambda}^3$  and  $H_{\Lambda}^4$  Lifetimes and Yields in Au+Au Collisions in the High Baryon Density Region”. *Phys. Rev. Lett.* 128.20 (2022), 202301. arXiv: [2110.09513 \[nucl-ex\]](#).
- [9] Jaroslav Adam et al. “Beam energy dependence of net- $\Lambda$  fluctuations measured by the STAR experiment at the BNL Relativistic Heavy Ion Collider”. *Phys. Rev. C* 102.2 (2020), 024903. arXiv: [2001.06419 \[nucl-ex\]](#).
- [10] J. Adam et al. “Measurement of the mass difference and the binding energy of the hypertriton and antihypertriton”. *Nature Phys.* 16.4 (2020), 409–412. arXiv: [1904.10520 \[hep-ex\]](#).
- [11] Jaroslav Adam et al. “Beam energy dependence of (anti-)deuteron production in Au + Au collisions at the BNL Relativistic Heavy Ion Collider”. *Phys. Rev. C* 99.6 (2019), 064905. arXiv: [1903.11778 \[nucl-ex\]](#).
- [12] Jaroslav Adam et al. “Collision-energy dependence of second-order off-diagonal and diagonal cumulants of net-charge, net-proton, and net-kaon multiplicity distributions in Au + Au collisions”. *Phys. Rev. C* 100.1 (2019). [Erratum: *Phys. Rev. C* 105, 029901 (2022)], 014902. arXiv: [1903.05370 \[nucl-ex\]](#).
- [13] L. Adamczyk et al. “Collision Energy Dependence of Moments of Net-Kaon Multiplicity Distributions at RHIC”. *Phys. Lett. B* 785 (2018), 551–560. arXiv: [1709.00773 \[nucl-ex\]](#).
- [14] L. Adamczyk et al. “Bulk Properties of the Medium Produced in Relativistic Heavy-Ion Collisions from the Beam Energy Scan Program”. *Phys. Rev. C* 96.4 (2017), 044904. arXiv: [1701.07065 \[nucl-ex\]](#).
- [15] L. Adamczyk et al. “Global  $\Lambda$  hyperon polarization in nuclear collisions: evidence for the most vortical fluid”. *Nature* 548 (2017), 62–65. arXiv: [1701.06657 \[nucl-ex\]](#).

x

**Date** : March 31, 2023

**Place** : Bhubaneswar

*Debasish Mallik.*  
(DEBASISH MALLICK)

**DEDICATED TO**

*my family, teachers, and friends*

## **ACKNOWLEDGEMENTS**

First and foremost, the author would like to humbly acknowledge that this endeavour would not have been completed without help and support from several people.

The author would like to thank his thesis supervisor, Prof. Bedangadas Mohanty, for his guidance, continuous support, advice, and motivation throughout the Ph.D. period. The author remains very much grateful to Prof. Mohanty for giving him an opportunity to do research on the physics of the QCD phase diagram and to join a worldwide collaboration of experimental physicists working on ultra-relativistic heavy-ion collisions. His constructive criticism throughout the whole period of this research project helped the author understand the heavy-ion collision physics subject better.

It gives the author immense pleasure to thank the outstanding researchers especially Prof. Nu Xu from Lawrence Berkeley National Laboratory (LBNL), Prof. Sourendu Gupta from Tata Institute of Fundamental Research (TIFR), and Dr. Dipak Kumar Mishra from Bhabha Atomic Research Centre (BARC) for their collaboration. The author is very grateful for having learned many important aspects of heavy-ion collision physics from them and for being always supportive and helpful.

The author is very much thankful to all the members of Higher Moments Focus Group for their physics discussions and especially to Prof. Nu Xu for enthusiastically convening the meeting every week which really helped in progress of analysis of the experimental data. The author would like to thank Prof. Xiaofeng Luo from Central China Normal University (CCNU) for very helpful physics discussions and for providing kind help during the stays in China to participate in physics discussion meetings and Quark Matter 2019. I would also like to thank Prof. ShinIchi Esumi and Dr. Toshihiro Nonaka from the University of Tsukuba, Japan for many important physics discussions.

The author would like to thank all the STAR physics working group (PWG) members and conveners for their discussions and suggestions which very much helped the data analysis. The author is thankful to each and every member of the STAR Collaboration for all their help and support. The author is also thankful to all the GPC members from STAR for the deuteron higher moments paper, especially to Prof. Declan Keane for reviewing the paper very efficiently. As a Ph.D. student, it was really very inspiring to see the cooperation among the hundreds of collaboration members across the world and a successful operation of the STAR experiment programs.

The author would like to take this opportunity to thank collaborators at the Brookhaven National Laboratory (BNL). Especially many thanks to Dr. Zhangbu Xu and Dr. Lijuan Ruan for their help during visits to the BNL. Many thanks Dr. J. Laurete, Dr. G. V. Buren for many helps regarding the STAR software and data taking shifts. The author would like to thank Ms. L. Mogavero for her valuable help during my visits to BNL. Also many thanks to the RHIC operations group for their contributions to the research work carried at the STAR experiment.

The author would like to acknowledge the computing resources such as GARUDA cluster at NISER, RACF at BNL and thank the teams behind them for operations and support.

The author is very much thankful to his teachers at Utkal University, Institute of Physics (IOP), and NISER who introduced him to the basics of high-energy nuclear physics and particle physics. Also, thankful to the Director of NISER Prof. Sudhakar Panda, and ex-Directors of the institute for providing with all the helps required during the Ph.D. period. The author expresses gratitude to his doctoral committee members Prof. Sanjay Kumar Swain, Dr. Prolay Kumar Mal, Dr. Victor Roy, and Dr. Arun Kumar Nayak (IOP) for their enthusiastic support.

The author would like to thank Dr. Ranbir Singh, Dr. Varchaswi Kashyap, Dr. Chitrasen Jena, Dr. Sabita Das, Dr. Ajay K. Dash, Dr. Rihan Haque, Dr. Md Nasim, and Dr. Subhash Singha for many helpful suggestions during the research work. A big thanks to seniors Dr. Vipul Bairathi and Dr. Debadeepti Mishra for introducing the author to the STAR analysis framework.

The author would like to express special thanks to friends and colleagues at NISER, Ashish, Ashutosh, Samir, Dukhishyam, Sourav, Vijay, Mouli, Prottay, Swati for sharing their valuable time on many occasions.

Finally, I am very grateful to my parents, my brothers and sisters, and all family members for their blessings, affection, support, and for everything they have done for me.

## SYNOPSIS

Interactions among the elementary particles of the universe occur via four fundamental forces. These forces are strong, electromagnetic, weak, and gravitational interactions. The standard model of elementary particles describes three forces, except gravity. In the standard model, the theory of strong interaction is known as Quantum chromodynamics (QCD). The QCD predicts that under extreme conditions such as at very high temperatures and/or density a new phase of strongly interacting nuclear matter exists, known as Quark-Gluon-Plasma (QGP) [1], in which quarks and gluons are no longer confined within hadrons. It is believed that this state of matter also existed in just a few microseconds old early universe after the Big Bang event. It is also speculated that such state of matter may exist in the dense cores of massive astrophysical objects such as neutron stars, where lower temperature but higher density [2] conditions are achieved. To understand this state of matter, high-energy heavy-ion collisions are carried out using the Relativistic Heavy-Ion Collider (RHIC) facility at the Brookhaven National Laboratory (BNL) and measurements are performed using the detectors of the STAR experiment. Heavy-ion collision experiments have demonstrated the existence of a deconfined state of quarks and gluons [3, 4].

First principle QCD (Lattice-QCD), as well as QCD-based model calculations, suggest that higher order cumulants of conserved charge numbers (Baryon, Electric charge, and Strange quantum numbers) are sensitive observables to probe finer into the details of the phase transition and freeze-out thermodynamics of the system [5–8]. In most of the theoretical modelings of the system formed in central high-energy heavy-ion collisions, it is assumed that the system is at/near the thermodynamic equilibrium. There is no apparent physical reason or theoretical proof that the system has to attain thermal equilibrium.

Studies on the comparison of measured mean yields of several hadrons to those calculated in a statistical model of an ideal gas of hadrons and resonances (HRG) in thermal equilibrium show that for suitable choices of model parameters known as chemical freeze-out parameters, the experimental data in most central heavy-ion collisions can be explained [9, 10]. These studies imply that the system formed in most central heavy-ion collisions has reached thermal equilibrium. However, these HRG models also seem to describe yield data in  $e^+e^-$  and  $p + p(\bar{p})$  collisions, where one does not expect the thermalized matter to be formed [11–13]. Similarly, they can describe yields in highly peripheral collisions. These observations introduce uncertainty in the interpretation of the freeze-out parameters derived using yields in terms of thermal conditions.

In this thesis, by using higher order cumulants (starting from mean up to 4<sup>th</sup> order) of net-proton (a proxy for net-baryon), net-kaon (a proxy for net-strangeness), and net-charge distributions and correlations among them, we systematically studied the topic of thermalization in high-energy heavy-ion collisions [14]. We perform the test of thermal equilibrium by checking that the mean hadron yields produced in the central heavy-ion collisions, as well as grand canonical fluctuations of conserved quantities, give consistent temperature and baryon chemical potential for the last scattering surface. Extensive measurements from gold (Au) on gold nuclei collisions from the STAR experiment for the higher order cumulants of net-proton, net-charge, and net-kaon distributions and mixed cumulants between different net-particle distributions, are utilized for this study.

The susceptibility ratios corresponding to the experimental observables are calculated in the Grand Canonical Ensemble (GCE) of the HRG model. In the model calculation, the detector's acceptance and resonance decay effects are taken into account. Chemical freeze-out conditions which can characterize the thermal nature of the system are temperature  $T$ , freeze-out volume  $V$ , and the three chemical potentials  $\mu_B$ ,  $\mu_Q$ , and  $\mu_S$ . Cumulant ratios

describing up to  $3^{rd}$  order fluctuations are used to extract the freeze-out conditions while the  $4^{th}$  order fluctuation is used for independent checks of the model. The HRG model calculations are compared to those measured in central and peripheral Au+Au collisions. Further, we compare the calculations to the synthetic Au+Au central collision data generated from a hadronic transport model (UrQMD model).

We observe that for central Au+Au collisions at  $\sqrt{s_{NN}} = 200, 62.4, \text{ and } 39 \text{ GeV}$ , the cumulants and correlations up to the third order show good agreement with the HRG model calculations. In addition, the  $4^{th}$  order cumulants of net-proton, net-charge, and net-kaon also agree with the model for the best fit values of freeze-out conditions. The freeze-out conditions are consistent with those obtained from the fits of mean yield of pions, kaons, and protons. The chemical freeze-out temperatures obtained from our study vary from  $T = 138 \text{ MeV}$  at  $\sqrt{s_{NN}} = 7.7 \text{ GeV}$  to  $T = 156 \text{ MeV}$  at  $\sqrt{s_{NN}} = 200 \text{ GeV}$  [14]. At the lower collision energies, the exclusion of net-proton higher cumulants allows a fair agreement of remaining observables with the model calculations. The peripheral data and those from central collisions in the UrQMD model, do not agree with the thermal model calculations. Further, we have verified that the measured  $p_T$  distributions of pion, kaon, proton, and their anti-particles for central Au+Au collisions at  $\sqrt{s_{NN}} = 200 \text{ and } 19.6 \text{ GeV}$  are reproduced using a thermal model with the extracted thermal parameters as inputs and for suitable choices of radial flow velocities.

The observations that the fluctuations of various conserved charges as well as the means of distributions, can be described using thermal equilibrium, implies that the matter formed in central Au+Au collisions at the three highest energies of RHIC, namely  $\sqrt{s_{NN}} = 200, 62.4, \text{ and } 39 \text{ GeV}$ , have reached thermal equilibrium. Also, the observation that protons fall out of the thermal equilibrium at lower collision energies is very interesting. Departures from thermodynamic equilibrium in the final state open up new directions in the search for

a QCD critical point.

Fluctuations observables are also predicted to be sensitive to the production mechanism of light nuclei in high-energy heavy ion collisions. Despite the freeze-out temperatures being of the order of 100 MeV, objects like deuterons, tritons, and other light nuclei which have binding energies of the order of a few MeVs are produced in such collisions [15, 16]. Interestingly, the yields of light nuclei can also be explained in the thermal models with the same freeze-out temperatures extracted using hadronic yield. The production mechanism of light nuclei is commonly discussed in two approaches: *thermal model* and *coalescence model*. The thermal model treats light nuclei as any other hadrons and their masses and quantum numbers are inputs to the model. In the coalescence model, nuclei are formed by protons and neutrons which are nearby in phase space. Both approaches have been fairly successful to describe the experimental data on light nuclei [15, 17]. However, the complete picture of light nuclei production in heavy-ion collisions is still to be understood.

Recently, it has been also suggested that higher order cumulants of event-by-event deuteron number fluctuations could serve as a potential probe to test different production scenarios [18]. The higher order cumulant ratios of deuteron number in a coalescence picture are predicted to show large deviations from the thermal model baseline, which is at unity. Also, the Pearson correlation coefficient of proton and deuteron numbers is predicted to have distinct nature in two of the production scenarios. Further, the production of deuterons is expected to affect by the presence of a QCD critical point and first-order phase transition. Specific combinations of yields of protons and light nuclei are constructed to probe neutron density fluctuations [19, 20]. In addition, as the deuteron carries two baryons, higher-order cumulants of deuteron number distribution might add to our current understanding of the baryon number fluctuations in high-energy heavy ion collisions.

In this thesis, we present the first measurements of the collision energy and centrality

dependence of higher order cumulants (up to the 4<sup>th</sup> order) of deuteron number fluctuations and correlations between protons and deuterons, in Au+Au collisions from the STAR experiment. Our measurements cover a wide range of the QCD phase diagram in terms of the baryon chemical potential, *i.e.*  $\mu_B = 20$  to 420 MeV. Corresponding collision energies are  $\sqrt{s_{NN}} = 7.7, 11.5, 14.5, 19.6, 27, 39, 54.4, 62.4,$  and 200 GeV. The deuterons are identified around mid-rapidity ( $|y| < 0.5$ ) in the transverse momentum ( $p_T$ ) region of  $0.8 < p_T < 4.0 \text{ GeV}/c$  using both Time Projection Chamber (TPC) and Time-of-Flight (TOF) detectors. Protons are also identified in  $|y| < 0.5$  and using TPC only for  $0.4 < p_T < 0.8 \text{ GeV}/c$ , and using both TPC and TOF for  $0.8 < p_T < 2.0 \text{ GeV}/c$ . To suppress the effect of event-by-event initial volume fluctuations on the measured cumulants of final state particles, a correction method known as Centrality Bin-Width Correction (CBWC) [21] is applied to the deuteron cumulants and proton-deuteron correlations. The cumulants and correlations are also corrected for the finite detector efficiency effect assuming the response of the detector to be binomial in nature [22–24]. Further, the statistical uncertainties on the cumulants and correlations are obtained using a monte-Carlo re-sampling technique known as the Bootstrap method [25]. Systematic uncertainties are obtained by varying different selection criteria related to the track quality and particle identification.

We perform different model calculations for comparison with the experimental results. Using the Thermal-FIST model [26] we calculate the cumulants and correlations in grand-canonical and canonical ensemble thermal models. The canonical model of Thermal-FIST uses an additional parameter called canonical correlation volume ( $V_c$ ), over which exact conservation of baryon number is imposed. Using a hadronic transport model known as the Ultra-relativistic Quantum Molecular Dynamics (UrQMD) model combined with a phase-space coalescence mechanism [27] to form deuterons, we calculated the cumulants and correlations for central Au+Au collisions at different collision energies. In addition, we

compare the results of the toy model simulation of the coalescence process from Ref. [18] to our measurements

We observe that the cumulant ratios of deuterons in central collisions vary smoothly as a function of the collision energy and are suppressed below the Poisson baseline as the colliding energy decreases. The peripheral collision results, however, remain overall flat with  $\sqrt{s_{\text{NN}}}$ .

Anti-correlation between proton and deuteron numbers is observed across all collision energies and centralities. With lowering the  $\sqrt{s_{\text{NN}}}$ , anti-correlation becomes stronger for central Au+Au collisions. Measurements for peripheral collisions do not show any  $\sqrt{s_{\text{NN}}}$  dependence and are close to the statistical expectations. The CE thermal model qualitatively predicts with the cumulant ratios for  $\sqrt{s_{\text{NN}}}$  below 20 GeV, while the thermal model with GCE fails. The GCE model also fails to predict the observed anti-correlation between the proton and deuteron. Similarly, the coalescence-based model (UrQMD + phase-space coalescence) describes the deuteron number fluctuation and deuteron-proton correlation measurements across all collision energies. A simple toy model simulation from Ref. [18] of the coalescence process also fails to predict the proton-deuteron correlation correctly.

Further, we compare deuteron  $\kappa\sigma^2$  in central Au+Au collisions to those measured for the proton [23, 24]. The  $\kappa\sigma^2$  of protons in central collisions shows a non-monotonic behavior with respect to the collision energies, a qualitative feature that is theoretically predicted due to the presence of the QCD critical point [28]. Though deuteron carries two baryons (one proton and one neutron), the higher order cumulant ratios of deuterons do not show such dependence on  $\sqrt{s_{\text{NN}}}$ . In a statistical test using cumulants of protons and  $d/p$  yield ratio as inputs, we modeled the deuteron distribution for central Au+Au collisions and calculated the cumulant ratios of deuterons as a function of collision energy. The cumulant ratios from this modeling come out closer to the Poisson baseline values. This test suggests

that event-by-event low yield might cause the higher-order cumulants of deuterons to come close to Poisson baselines.

These observations suggest that the effect of the baryon number conservation is important for fluctuation measurements at lower collision energies and despite the low yields of deuterons, one needs the canonical ensemble in the thermal model to understand deuteron fluctuations and proton-deuteron cumulants. The observation that a simple toy model simulation of the coalescence process fails while the UrQMD+coalescence model correctly predicts the trend of the data, implies that phase-space density information of constituent nucleons is important for the deuteron formation process in the coalescence mechanism. Our measurements indeed will provide inputs for future investigations of the production mechanism and freeze-out thermodynamics of deuterons and light nuclei in general.

## References

- [1] Edward V. Shuryak. “Quantum Chromodynamics and the Theory of Superdense Matter”. *Phys. Rept.* 61 (1980), 71–158.
- [2] J. M. Lattimer and M. Prakash. “The physics of neutron stars”. *Science* 304 (2004), 536–542. arXiv: [astro-ph/0405262](#).
- [3] John Adams et al. “Experimental and theoretical challenges in the search for the quark gluon plasma: The STAR Collaboration’s critical assessment of the evidence from RHIC collisions”. *Nucl. Phys. A* 757 (2005), 102–183. arXiv: [nucl-ex/0501009](#).
- [4] Betty Abelev et al. “ $J/\psi$  suppression at forward rapidity in Pb-Pb collisions at  $\sqrt{s_{NN}} = 2.76$  TeV”. *Phys. Rev. Lett.* 109 (2012), 072301. arXiv: [1202.1383](#) [[hep-ex](#)].

- [5] S. Borsanyi, Z. Fodor, S. D. Katz, et al. “Freeze-out parameters from electric charge and baryon number fluctuations: is there consistency?” *Phys. Rev. Lett.* 113 (2014), 052301. arXiv: [1403.4576 \[hep-lat\]](#).
- [6] Misha A. Stephanov, K. Rajagopal, and Edward V. Shuryak. “Event-by-event fluctuations in heavy ion collisions and the QCD critical point”. *Phys. Rev. D* 60 (1999), 114028. arXiv: [hep-ph/9903292](#).
- [7] Frithjof Karsch and Krzysztof Redlich. “Probing freeze-out conditions in heavy ion collisions with moments of charge fluctuations”. *Phys. Lett. B* 695 (2011), 136–142. arXiv: [1007.2581 \[hep-ph\]](#).
- [8] A. Pandav, D. Mallick, and B. Mohanty. “Search for the QCD critical point in high energy nuclear collisions”. *Prog. Part. Nucl. Phys.* 125 (2022), 103960. arXiv: [2203.07817 \[nucl-ex\]](#).
- [9] J. Cleymans, H. Oeschler, K. Redlich, et al. “Comparison of chemical freeze-out criteria in heavy-ion collisions”. *Phys. Rev. C* 73 (2006), 034905. arXiv: [hep-ph/0511094](#).
- [10] Anton Andronic, Peter Braun-Munzinger, Krzysztof Redlich, et al. “Decoding the phase structure of QCD via particle production at high energy”. *Nature* 561.7723 (2018), 321–330. arXiv: [1710.09425 \[nucl-th\]](#).
- [11] Francesco Becattini. “A Thermodynamical approach to hadron production in e+ e- collisions”. *Z. Phys. C* 69.3 (1996), 485–492.
- [12] F. Becattini and Ulrich W. Heinz. “Thermal hadron production in p p and p anti-p collisions”. *Z. Phys. C* 76 (1997). [Erratum: *Z.Phys.C* 76, 578 (1997)], 269–286. arXiv: [hep-ph/9702274](#).

- [13] Sabita Das, Debadeepti Mishra, Sandeep Chatterjee, et al. “Freeze-out conditions in proton-proton collisions at the highest energies available at the BNL Relativistic Heavy Ion Collider and the CERN Large Hadron Collider”. *Phys. Rev. C* 95.1 (2017), 014912. arXiv: [1605.07748 \[nucl-th\]](#).
- [14] Sourendu Gupta, Debasish Mallick, Dipak Kumar Mishra, et al. “Limits of thermalization in relativistic heavy ion collisions”. *Phys. Lett. B* 829 (2022), 137021.
- [15] Jaroslav Adam et al. “Beam energy dependence of (anti-)deuteron production in Au + Au collisions at the BNL Relativistic Heavy Ion Collider”. *Phys. Rev. C* 99.6 (2019), 064905. arXiv: [1903.11778 \[nucl-ex\]](#).
- [16] Jaroslav Adam et al. “Production of light nuclei and anti-nuclei in pp and Pb-Pb collisions at energies available at the CERN Large Hadron Collider”. *Phys. Rev. C* 93.2 (2016), 024917. arXiv: [1506.08951 \[nucl-ex\]](#).
- [17] L. Adamczyk et al. “Measurement of elliptic flow of light nuclei at  $\sqrt{s_{NN}} = 200, 62.4, 39, 27, 19.6, 11.5, \text{ and } 7.7$  GeV at the BNL Relativistic Heavy Ion Collider”. *Phys. Rev. C* 94.3 (2016), 034908. arXiv: [1601.07052 \[nucl-ex\]](#).
- [18] Zuzana Fecková, Jan Steinheimer, Boris Tomášik, et al. “Formation of deuterons by coalescence: Consequences for deuteron number fluctuations”. *Phys. Rev. C* 93.5 (2016), 054906. arXiv: [1603.05854 \[nucl-th\]](#).
- [19] Kai-Jia Sun, Lie-Wen Chen, Che Ming Ko, et al. “Probing QCD critical fluctuations from light nuclei production in relativistic heavy-ion collisions”. *Phys. Lett. B* 774 (2017), 103–107. arXiv: [1702.07620 \[nucl-th\]](#).
- [20] Edward Shuryak and Juan M. Torres-Rincon. “Baryon clustering at the critical line and near the hypothetical critical point in heavy-ion collisions”. *Phys. Rev. C* 100.2 (2019), 024903. arXiv: [1805.04444 \[hep-ph\]](#).

- [21] Xiaofeng Luo, Ji Xu, Bedangadas Mohanty, et al. “Volume fluctuation and auto-correlation effects in the moment analysis of net-proton multiplicity distributions in heavy-ion collisions”. *J. Phys. G* 40 (2013), 105104. arXiv: [1302.2332 \[nucl-ex\]](#).
- [22] Toshihiro Nonaka, Masakiyo Kitazawa, and ShinIchi Esumi. “More efficient formulas for efficiency correction of cumulants and effect of using averaged efficiency”. *Phys. Rev. C* 95.6 (2017). [Erratum: *Phys.Rev.C* 103, 029901 (2021)], 064912. arXiv: [1702.07106 \[physics.data-an\]](#).
- [23] J. Adam et al. “Nonmonotonic Energy Dependence of Net-Proton Number Fluctuations”. *Phys. Rev. Lett.* 126.9 (2021), 092301. arXiv: [2001.02852 \[nucl-ex\]](#).
- [24] Mohamed Abdallah et al. “Cumulants and correlation functions of net-proton, proton, and antiproton multiplicity distributions in Au+Au collisions at energies available at the BNL Relativistic Heavy Ion Collider”. *Phys. Rev. C* 104.2 (2021), 024902. arXiv: [2101.12413 \[nucl-ex\]](#).
- [25] Ashish Pandav, Debasish Mallick, and Bedangadas Mohanty. “Effect of limited statistics on higher order cumulants measurement in heavy-ion collision experiments”. *Nucl. Phys. A* 991 (2019), 121608. arXiv: [1809.08892 \[nucl-ex\]](#).
- [26] Volodymyr Vovchenko and Horst Stoecker. “Thermal-FIST: A package for heavy-ion collisions and hadronic equation of state”. *Comput. Phys. Commun.* 244 (2019), 295–310. arXiv: [1901.05249 \[nucl-th\]](#).
- [27] Sukanya Sombun, Kristiya Tomuang, Ayut Limphirat, et al. “Deuteron production from phase-space coalescence in the UrQMD approach”. *Phys. Rev. C* 99.1 (2019), 014901. arXiv: [1805.11509 \[nucl-th\]](#).
- [28] M. A. Stephanov. “On the sign of kurtosis near the QCD critical point”. *Phys. Rev. Lett.* 107 (2011), 052301. arXiv: [1104.1627 \[hep-ph\]](#).

# Contents

<b>List of Figures</b>	<b>xxix</b>
<b>List of Tables</b>	<b>xxxvi</b>
<b>1 Introduction</b>	<b>1</b>
1.1 Brief Introduction to Quantum Chromodynamics . . . . .	3
1.2 Deconfinement and QCD Phase Diagram . . . . .	5
1.3 Relativistic Heavy Ion Collisions . . . . .	8
1.3.1 Space-time Evolution . . . . .	9
1.3.2 Variables of General Interest . . . . .	11
1.3.2.1 Rapidity . . . . .	12
1.3.2.2 Pseudorapidity . . . . .	12
1.3.2.3 Transverse Momentum . . . . .	13
1.3.2.4 Invariant Yield . . . . .	13
1.3.2.5 Particle Multiplicity . . . . .	13
1.3.2.6 Collision Centrality . . . . .	14
1.3.3 Experimental Signatures of Quark-Gluon Plasma . . . . .	14
1.3.3.1 Transverse Momentum Spectra and Yields . . . . .	14
1.3.3.2 Collectivity . . . . .	17
1.4 Higher Moments of Fluctuations . . . . .	19
1.4.1 Cumulants and Moments . . . . .	20
1.4.1.1 Definitions . . . . .	20
1.4.1.2 Properties of Cumulants . . . . .	23
1.4.2 Connection to the Thermodynamic Susceptibilities . . . . .	24
1.5 Thesis Physics Motivation . . . . .	26

1.5.1	Probing Light Nuclei Production via Fluctuations . . . . .	26
1.5.2	Freeze-out and Thermalization . . . . .	27
1.6	Organization of the Thesis . . . . .	29
<b>2</b>	<b>The STAR Experiment</b>	<b>37</b>
2.1	Relativistic Heavy Ion Collider (RHIC) . . . . .	37
2.2	The STAR Detector . . . . .	39
2.2.1	The Time Projection Chamber (TPC) . . . . .	42
2.2.1.1	Technical Design of TPC . . . . .	42
2.2.1.2	Track Reconstruction in TPC . . . . .	44
2.2.1.3	Particle Identification Using $dE/dx$ Measurements . . . . .	45
2.2.2	Time of Flight (TOF) Detector . . . . .	48
2.2.3	Trigger Detectors . . . . .	50
<b>3</b>	<b>Deuteron Cumulants and Proton-Deuteron Correlation in Au+Au Collisions at RHIC</b>	<b>55</b>
3.1	Introduction . . . . .	56
3.2	Data Analysis . . . . .	61
3.2.1	Data set and Trigger . . . . .	61
3.2.2	Event Selection . . . . .	62
3.2.3	Track Selection and Particle Identification . . . . .	66
3.2.4	Collision Centrality Determination . . . . .	69
3.2.4.1	MC Glauber and Two Component Models . . . . .	70
3.2.5	Efficiency Correction . . . . .	72
3.2.6	Centrality Bin-Width Correction . . . . .	74
3.2.7	Statistical and Systematic Uncertainties . . . . .	75
3.2.7.1	Statistical Uncertainties . . . . .	76
3.2.7.2	Systematic Uncertainties . . . . .	77
3.3	Results and Discussion . . . . .	78
3.3.1	Event-by-Event Deuteron Distributions . . . . .	78
3.3.2	Deuteron Cumulants . . . . .	80
3.3.3	Model Calculations . . . . .	82
3.3.3.1	Deuterons in the Thermal Model . . . . .	82

3.3.3.2	Deuterons in UrQMD + Phase-space Coalescence Model	84
3.3.4	Cumulant Ratios and Pearson Coefficient . . . . .	84
3.4	Summary . . . . .	89
3.A	Event-by-Event Deuteron Distributions . . . . .	95
<b>4</b>	<b>Limits of Thermalization in Relativistic Heavy Ion Collisions</b>	<b>99</b>
4.1	Chemical Freeze-out and Thermalization . . . . .	100
4.2	Thermodynamic Modeling of Heavy-Ion Collisions . . . . .	102
4.2.1	Hadron Resonance Gas (HRG) model . . . . .	102
4.2.2	Resonance decay contributions . . . . .	106
4.2.2.1	Single Resonance Decay . . . . .	106
4.2.2.2	Decays of Multiple Resonances . . . . .	107
4.2.2.3	Inclusion of Thermal Fluctuations . . . . .	108
4.3	Experimental Observables . . . . .	110
4.4	Analysis Method . . . . .	112
4.5	Results and Discussion . . . . .	114
4.6	Conclusion . . . . .	121
<b>5</b>	<b>Summary and Conclusions</b>	<b>129</b>



# List of Figures

1.1	List of elementary particles of the standard model, force carrying gauge bosons and Higgs boson are shown. I, II, and III represent the three generations of quarks and leptons. The figure is taken from [12]. . . . .	2
1.2	$\alpha_S(Q)$ measured values as a function of the respective energy scale $Q$ . The figure is taken from Ref. [14]. . . . .	4
1.3	Energy density and three times the pressure divided by $T^4$ (which scales as the number of degrees of freedom) as a function of the temperature from lattice QCD. Calculations performed on lattices with temporal extent $N_\tau = 4$ and 6 with three flavors of quark and vanishing quark chemical potentials. Figure taken from Ref. [22]. . . . .	6
1.4	Schematic QCD phase diagram showing different phases. Phase change from a hadron gas to QGP phase via a smooth crossover, a first-order phase transition, and a possible QCD critical point are outlined in different regions of $T$ and $\mu_B$ much of which is accessible by the current and future experimental facilities. Figure taken from Ref. [23].	7
1.5	Sketch of a ultra-relativistic collision between two nuclei. The nucleons taking part in the collision are known as participants and are shown using red color. The remnant nucleons are called spectators and are shown using yellow color. . . . .	9
1.6	Evolution of heavy-ion collision shown as different stages using a space-time diagram.	10
1.7	A schematic presentation of co-ordinate system for two colliding nuclei. . . . .	12
1.8	Yields from the statistical thermal model compared to experimental data from central Au+Au collisions at $\sqrt{s_{NN}} = 200$ GeV. Figure is taken from Ref. [39]. . . . .	15
1.9	Contours of kinetic freezeout temperature $T_{fo}$ and average radial flow velocity $\langle\beta_T\rangle$ extracted from thermal + radial flow fits of $p_T$ spectra of many light and multi-strange hadrons produced in $\sqrt{s_{NN}} = 200$ GeV Au+Au collisions. The figure is taken from Ref. [35]. . . . .	16

1.10	Schematic diagram showing the transformation of coordinate space anisotropy in the initial state into a momentum space anisotropy for non-central nucleus-nucleus collision.	17
1.11	(Top panel) $v_2$ as a function of $p_T$ and (Bottom panel) $v_2/n_q$ as a function of $(m_T - m_0)/n_q$ for $D^0$ , $K_S^0$ , $\Lambda$ , and $\Xi^-$ in 10–40% centrality Au+Au collisions at $\sqrt{s_{NN}} = 200$ GeV. Figure taken from Ref. [40].	18
1.12	Distributions showing negative skewness (in the left panel) and positive skewness (in the right panel). Source of the figure is at [44].	22
1.13	Visual example of kurtosis for seven well-known distributions from different parametric family. The figure is taken from [45].	23
1.14	Best fit values of yields from the thermal statistical model compared to experimentally measured yields in the ALICE experiment for central Pb+Pb collisions at $\sqrt{s_{NN}} = 2.76$ TeV. The figure is taken from Ref. [65].	28
2.1	Top view of the RHIC accelerator situated at the Brookhaven National Laboratory, New York, USA [2].	38
2.2	Schematic three-dimensional picture of the STAR detector layout. Primary sub-systems are outlined except the ZDC. As the VPD and the BBC detectors are placed in both east and west directions of the collision point, only one side of those are visible from this particular angle. The figure is taken from [11].	40
2.3	Schematic section cut of the STAR detector representing the co-ordinate system [12].	41
2.4	Collision event from the first gold beam-beam collisions at RHIC at 100+100 GeV/c per beam recorded by STAR TPC detector. Blue and green colored tracks carry opposite electric charge. The small visible gaps are due to the boundaries between different sectors of the TPC [13].	41
2.5	A schematic diagram (in three dimension) displaying major parts of the TPC detector [15].	42
2.6	Example of one sector of anode of TPC detector showing different sub-sectors. On the left, outer subsector is shown and the on the right the inner subsector is shown [15].	43
2.7	Ionization energy loss measured in the STAR TPC detector for different charged particles is shown as a function of rigidity ( $p/Z$ ) [20].	47
2.8	$1/\beta$ from TOF vs. rigidity (momentum/charge) at $\sqrt{s_{NN}} = 39$ GeV. The curves, from low to up, show the expected mean values of pions, kaons, and (anti-) protons, respectively. The figure is taken from [23].	49

3.1	Energy dependence of anti-proton to proton ( $\bar{p}/p$ ) and anti-deuteron to deuteron ( $\bar{d}/d$ ) ratio measured in central heavy-ion collisions in different experiments. The $\bar{d}/d$ values from STAR, PHENIX, and ALICE experiments are shown as the star, triangle, and inverted triangle markers, respectively. The curves represent thermal model calculations. Figure is taken from Ref. [4]. . . . .	57
3.2	Atomic mass number ( $A$ ) scaling of the mid-rapidity $v_2$ of $p$ , $\bar{p}$ , $d$ , $\bar{d}$ and other light-nuclei from minimum bias Au + Au collisions at $\sqrt{s_{NN}} = 7.7 - 200$ GeV. Figure is taken from Ref. [12]. . . . .	58
3.3	The energy dependence of the moments $\sigma^2/\langle n_d \rangle$ , $S\sigma$ , and $\kappa\sigma^2$ of the deuteron distribution obtained from a coalescence model in Ref. [21], where $\langle n_d \rangle$ is the mean, $\sigma$ is the width, $S$ is the skewness, and $\kappa$ is the kurtosis of deuteron distribution. . . . .	59
3.4	The energy dependence of the Pearson correlation coefficient ( $\rho(n_p, n_d)$ ) between proton and deuteron numbers calculated in the coalescence model for two different assumptions on proton and neutron distributions. The figure is taken from Ref. [21]. . . . .	60
3.5	Run-wise $\langle p_T \rangle$ . . . . .	63
3.6	Run-wise $\langle \eta \rangle$ . . . . .	63
3.7	Run-wise $\langle \phi \rangle$ . . . . .	63
3.8	Run-wise $\langle V_x \rangle$ . . . . .	63
3.9	Run-wise $\langle V_y \rangle$ . . . . .	63
3.10	Run-wise $\langle V_z \rangle$ . . . . .	63
3.11	Correlation between Refmult (from TPC) and TOFmatched tracks. Events lying below the solid red line are excluded from the analysis. . . . .	64
3.12	Time variation (in terms of event id) of signed $DCA_{xy}$ in a run at $\sqrt{s_{NN}} = 7.7$ GeV. . . . .	65
3.13	$\langle dE/dx \rangle$ and $m^2$ distribution of charged particles for $ \eta  < 1.0$ in Au+Au collisions at $\sqrt{s_{NN}} = 27$ GeV. Panel (a): The $\langle dE/dx \rangle$ distribution of charged particles from TPC as a function of rigidity ( $p/Z$ ). The curves represent the expected values of $\langle dE/dx \rangle$ calculated using the Bichsel function [27] for the corresponding particles. Panel (b): Mass square of charged particles as a function of momentum from TOF. The dashed lines represent the mass square values from the Particle Data Group (PDG) booklet [28] for the corresponding particles. . . . .	67
3.14	$Z_d$ distribution from ionization energy loss in TPC in $p_T$ range $0.8 < p_T < 1.0$ GeV/c for central Au+Au collisions at $\sqrt{s_{NN}} = 19.6$ GeV. . . . .	68

3.15	$m^2$ distribution of deuterons from TOF detector in $p_T$ range $0.8 < p_T < 1.0$ GeV/ $c$ for central Au+Au collisions at $\sqrt{s_{NN}} = 19.6$ GeV. . . . .	68
3.16	Normalised <i>RefMult-3</i> distributions in Au+Au collisions at $\sqrt{s_{NN}} = 7.7 - 200$ GeV from STAR experiment. The red dashed lines show the MC Glauber + Two-component model results. The figure is taken from Ref. [18]. . . . .	70
3.17	Impact parameter ( $b$ ) distribution calculated in MC Glauber model for Au+Au collisions at $\sqrt{s_{NN}} = 54.4$ GeV. . . . .	71
3.18	Number of participants ( $N_{part}$ ) distribution calculated in MC Glauber model for Au+Au collisions at $\sqrt{s_{NN}} = 54.4$ GeV. . . . .	71
3.19	TPC efficiency of deuterons in Au+Au collisions at $\sqrt{s_{NN}} = 7.7, 39$ and $200$ GeV for 0-5%, 30-40% and 70-80% centrality. . . . .	72
3.20	TOF matching efficiency of deuterons in Au+Au collisions at $\sqrt{s_{NN}} = 7.7, 39$ and $200$ GeV for 0-5%, 20-30% and 70-80% centrality. . . . .	73
3.21	Event-by-event deuteron number distributions for 0-5% central and 70-80% Au+Au collisions for three collision energies, $\sqrt{s_{NN}} = 7.7, 39,$ and $200$ GeV measured by STAR. The distributions are normalized to the total number of events at each $\sqrt{s_{NN}}$ . The statistical uncertainties are smaller than the marker symbols. Lines connecting the data points are shown to guide the eye. The deuteron numbers in this figure are not corrected for detection efficiency. . . . .	79
3.22	Cumulants ( $C_n, n = 1 - 4$ ) of deuteron distributions in Au+Au collisions from $\sqrt{s_{NN}} = 7.7 - 200$ GeV as a function of the average number of participant nucleons. Statistical and systematic uncertainties are shown. . . . .	80
3.23	Cumulants ( $C_n, n = 1 - 4$ ) of the deuteron distributions as a function of collision energy for central (0-5%), mid-central (30-40%), and peripheral (70-80%) Au+Au collisions were measured by STAR. Results for central, mid-central, and peripheral collisions are shown using solid circle, open cross, and open square markers, respectively. Bar and cap symbols represent the statistical and systematic uncertainties, respectively. The transverse momentum ( $p_T$ ) range for the measurements is from $0.8$ to $4$ GeV/ $c$ and the rapidity ( $y$ ) range is $-0.5 < y < 0.5$ . . . . .	81
3.24	Illustration of canonical correlation volume in the canonical ensemble of a thermal model. . . . .	83

- 3.25 Cumulant ratios of deuteron distributions and proton-deuteron Pearson co-efficient shown as a function of  $\sqrt{s_{\text{NN}}}$ . Red solid circle and open square markers represent measurements for most central (0-5%) and peripheral (70-80%) collisions, respectively. Bar and cap symbols show the statistical and systematic uncertainties, respectively. Poisson baselines (unity for cumulant ratios and zero for Pearson coefficient) are shown by the gray dashed line. UrQMD+phase-space coalescence calculations are shown using the orange color-filled band. Thermal-FIST model calculations for GCE are shown using a magenta dashed line. The cyan color-filled band represents the CE thermal model results corresponding to the range of canonical correlation volume ( $V_c$ ) from  $2dV/dy$  to  $4dV/dy$ . CE thermal model results for  $\chi^2$  minimum fit of above four observables is shown using cyan color dashed line. In panel (d), results for one of the assumptions (independent proton and neutron distributions) in the toy model simulation of a coalescence process from Ref. [21] are shown using a blue dashed line. 85
- 3.26  $\kappa\sigma^2$  of deuteron and proton distribution for most central (0-5%) Au+Au collisions. Red circle and black triangle markers represent deuteron and proton data [18], respectively. The gray dashed line is the Poisson baseline (unity).  $\kappa\sigma^2$  of deuterons show smooth dependence on the collision energies in contrast to protons. . . . . 88
- 3.1 Event-by-event deuteron number distributions for 0-5% central Au+Au collisions for different collision energies,  $\sqrt{s_{\text{NN}}} = 7.7\text{--}200$  GeV measured by STAR. For each  $\sqrt{s_{\text{NN}}}$  and centrality, the event-by-event distributions are normalized to the total number of events. Lines connecting the data points are shown to guide the eye. The statistical uncertainties are within the sizes markers. The deuteron numbers shown on the  $x$ -axis are not corrected for detection efficiency. . . . . 96
- 3.2 Event-by-event deuteron number distributions for 70-80% peripheral Au+Au collisions for different collision energies,  $\sqrt{s_{\text{NN}}} = 7.7\text{--}200$  GeV measured by STAR. For each  $\sqrt{s_{\text{NN}}}$  and centrality, the event-by-event distributions are normalized to the total number of events. Lines connecting the data points are shown to guide the eye. The statistical uncertainties are within the sizes markers. The deuteron numbers shown on the  $x$ -axis are not corrected for detection efficiency. . . . . 97

- 4.1  $\chi^2/\text{NDF}$  defined using Equation 4.30 are shown as a function of  $T$  and  $\mu_B$  to represent the nature agreement of data with HRG model expectations.  $\mu_Q$  and  $\mu_S$  are held fixed to their best fit values. Shown results correspond to thirteen observable fit for the data measured in the STAR experiment for the most central (0-5%) Au+Au collisions at energies  $\sqrt{s_{\text{NN}}} = 7.7\text{--}200$  GeV. . . . . 113
- 4.2 All observables studied are shown in Au+Au collisions at two representative collision energies  $\sqrt{s_{\text{NN}}} = 200$  GeV in panel (a) and  $\sqrt{s_{\text{NN}}} = 39$  GeV in panel (b). The difference between data and the HRG model values (from the best fit of 13 observables) divided by the statistical uncertainty in the data is plotted on the y-axis. Observables are mentioned along the x-axis. Note that the values for central collisions are much smaller than for peripheral. The latter is shown as open circles and is presented in the figure after scaling down by a factor of ten. The figure also shows a comparison of the magnitudes of systematic and statistical uncertainties. . . . . 114
- 4.3 The best-fit values and errors on the chemical freeze-out parameters of the HRG model at  $\sqrt{s_{\text{NN}}} = 7.7, 11.5, 19.6, 27, 39, 62.4,$  and  $200$  GeV are obtained by the comparison of central Au+Au collisions data with the thermal model. Open triangles show results for 13 observable fits at collision energies where the fit quality is good. Solid square markers represent results for 11 observable fits at all energies. Open circles (markers slightly displaced to the left along the x-axis for clarity of presentation) represent freeze-out conditions from [7] obtained using only the mean yields of several hadrons in the STAR experiment. Also shown using open star markers parameters at  $\sqrt{s_{\text{NN}}} = 200$  GeV obtained by the fit of the mean yields of only  $\pi^\pm, K^\pm$  and  $p(\bar{p})$  [6]. . . . . 115
- 4.4 Solid markers represent  $p_T$  distribution of pion, kaon, proton, and their anti-particles for most central Au+Au collisions at  $\sqrt{s_{\text{NN}}} = 19.6$  GeV measured in the STAR experiment [7] at RHIC. Thermal model calculations using freeze-out parameters extracted in this study and average radial flow velocity  $\langle\beta\rangle = 0.466c$  is shown using the grey shaded band. . . . . 118
- 4.5 Solid markers represent transverse momentum ( $p_T$ ) spectra of pion, kaon, proton, and their anti-particles for most central Au+Au collisions at  $\sqrt{s_{\text{NN}}} = 200$  GeV measured in the PHENIX experiment [47] at RHIC. Thermal model calculations using freeze-out parameters extracted in this study and average radial flow velocity  $\langle\beta\rangle = 0.58c$ , are shown using the grey-shaded band. . . . . 118

4.6 Comparison of freeze-out conditions from the fit of different orders of moments. Differences in freeze-out temperatures ( $\Delta T$  in the top row) and baryon chemical potential ( $\Delta\mu_B$  in the bottom row) are shown. The difference in temperature ( $\Delta T$ ) and baryon chemical potential ( $\Delta\mu_B$ ) from the second order to the first order, third order to second order, and third order to first order moments are shown as filled-circles, open-triangles, and open-squares, respectively. For central Au+Au collisions in STAR (shown in the left column), freeze-out conditions of different orders of moments show very good agreement with each other except at lower  $\sqrt{s_{NN}}$ . For peripheral Au+Au collisions in STAR (shown in the middle column) and for the UrQMD model (shown in the right column) fits of different orders of moments give very different results, implying that thermalization is not seen. . . . . 119

4.7 Freeze-out conditions in terms of temperature  $T$  and baryon chemical potential  $\mu_B$  for 0–5% most central Au+Au collision at  $\sqrt{s_{NN}} = 7.7–200$  GeV. The red circles show the  $T$  and  $\mu_B$  values obtained from thirteen observables fit while star markers represent those for eleven observables. Chemical freeze-out results using only hadron yield data are shown as dashed red line [19, 20]. Representing the smooth crossover region are the Lattice QCD results shown as green-band [48]. The dotted black line, blue square, and gray band represent the conjectured phase boundary in terms of crossover, speculated critical point, and first-order phase transition, respectively. . . . . 120

4.8	In the collision energy range at RHIC, this figure shows the regions where thermodynamic equilibrium can be verified at the chemical freeze-out surface and where it cannot. Collision energy $\sqrt{s_{NN}}$ dependence of $\chi^2/\text{NDF}$ obtained from the fits of thirteen observable sets listed in table 4.1 (shown with filled red circles) and the eleven observable sets (shown with filled blue squares). The lower panel shows the dependence on $\sqrt{s_{NN}}$ of $C_4/C_2 = \kappa\sigma^2$ for the net-proton distribution in the most central Au+Au collisions measured in the STAR experiment [4]. The inset shows the measured net-proton distribution for most central collisions at $\sqrt{s_{NN}} = 19.6$ GeV. The red line corresponds to the statistical baseline of net-proton distribution known as the Skellam distribution. The color filling in both the top and bottom panels tentatively divides the range of collision energies into regions that are clearly in agreement with the predictions of an ideal gas of resonances, and therefore cannot contain the QCD critical point (labeled “No CP”) and one which is not in agreement with such a thermodynamic model, and therefore remains open for search. This is consistent with predictions from recent lattice QCD calculations which also disfavor the high energy region for the critical point search [49, 50]. . . . .	122
-----	---	-----

## List of Tables

3.1	Collision energy, year, production tag, and triggers used. . . . .	62
3.2	Collision energy, vertex cuts, and event statistics. . . . .	64
3.3	Track selection criteria for the analysis presented in this chapter. . . . .	66

4.1	The full set of observables constructed from distributions of event-to-event fluctuations of hadrons by the STAR experiment are shown in the first row. We use 13 of these observables for the test of thermalization. The fourth-order cumulants are used for independent verification of the hypothesis of thermodynamic equilibrium. At lower collision energies where the full thermodynamic equilibrium of all listed observables is not supported, we use the 11 observable sets as an effective measure to extract the freeze-out conditions. . . . .	111
4.2	Freeze-out conditions and their uncertainties are summarized for different collision energies. For $\sqrt{s_{\text{NN}}} = 39 - 200$ GeV, the freeze-out conditions are obtained from the 13-observable fit while for $\sqrt{s_{\text{NN}}} = 27 - 7.7$ GeV, those are obtained from the 11-observable fit. . . . .	116



# Chapter 1

## Introduction

Understanding the structure and interactions of the fundamental constituents of matter in the Universe is one of the primary goals of physics. The branch of physics that broadly deals with this topic is known as particle physics. Centuries ago, the basic philosophical idea that matter is made up of tiny indivisible particles appeared in many ancient cultures such as those of Greece and India. In the early 19th century, scientist John Dalton's work laid the foundation of our modern atomic theory. With the advent of modern physics, electrons, protons, and neutrons were found to be constituents of an atom. Now we know that the protons and the neutrons in an atom are not fundamental particles like electrons. Protons and neutrons collectively known as nucleons consist of quarks that are held together by the strong force mediator particles known as gluons. The "Standard Model" of particle physics classifies all known elementary constituents of matter and systematically describes three of the four known fundamental forces (strong, electromagnetic, and weak interactions – excluding gravity).

The standard model was developed in stages by a series of theoretical and experimental discoveries in the latter half of the 20th century [1–7]. The most recent addition to this

model was the experimental discovery of the Higgs boson at CERN in the year 2012 [8, 9] theorized by Peter Higgs in 1964 [10, 11].

**Standard Model of Elementary Particles**

		three generations of matter (elementary fermions)			three generations of antimatter (elementary antifermions)			interactions / force carriers (elementary bosons)	
		I	II	III	I	II	III		
mass		$\approx 2.2 \text{ MeV}/c^2$	$\approx 1.28 \text{ GeV}/c^2$	$\approx 173.1 \text{ GeV}/c^2$	$\approx 2.2 \text{ MeV}/c^2$	$\approx 1.28 \text{ GeV}/c^2$	$\approx 173.1 \text{ GeV}/c^2$	0	$\approx 124.97 \text{ GeV}/c^2$
charge		$\frac{2}{3}$	$\frac{2}{3}$	$\frac{2}{3}$	$-\frac{2}{3}$	$-\frac{2}{3}$	$-\frac{2}{3}$	0	0
spin		$\frac{1}{2}$	$\frac{1}{2}$	$\frac{1}{2}$	$\frac{1}{2}$	$\frac{1}{2}$	$\frac{1}{2}$	1	0
		<b>u</b> up	<b>c</b> charm	<b>t</b> top	<b><math>\bar{u}</math></b> antiup	<b><math>\bar{c}</math></b> anticharm	<b><math>\bar{t}</math></b> antitop	<b>g</b> gluon	<b>H</b> higgs
	<b>QUARKS</b>	<b>d</b> down	<b>s</b> strange	<b>b</b> bottom	<b><math>\bar{d}</math></b> antidown	<b><math>\bar{s}</math></b> antistrange	<b><math>\bar{b}</math></b> antibottom	<b><math>\gamma</math></b> photon	
		$\approx 4.7 \text{ MeV}/c^2$	$\approx 96 \text{ MeV}/c^2$	$\approx 4.18 \text{ GeV}/c^2$	$\approx 4.7 \text{ MeV}/c^2$	$\approx 96 \text{ MeV}/c^2$	$\approx 4.18 \text{ GeV}/c^2$	0	
		$-\frac{1}{3}$	$-\frac{1}{3}$	$-\frac{1}{3}$	$\frac{1}{3}$	$\frac{1}{3}$	$\frac{1}{3}$	0	
		$\frac{1}{2}$	$\frac{1}{2}$	$\frac{1}{2}$	$\frac{1}{2}$	$\frac{1}{2}$	$\frac{1}{2}$	1	
		<b>e</b> electron	<b><math>\mu</math></b> muon	<b><math>\tau</math></b> tau	<b><math>e^+</math></b> positron	<b><math>\bar{\mu}</math></b> antimuon	<b><math>\bar{\tau}</math></b> antitau	<b><math>Z^0</math></b> $Z^0$ boson	
	<b>LEPTONS</b>	$\approx 0.511 \text{ MeV}/c^2$	$\approx 105.66 \text{ MeV}/c^2$	$\approx 1.7768 \text{ GeV}/c^2$	$\approx 0.511 \text{ MeV}/c^2$	$\approx 105.66 \text{ MeV}/c^2$	$\approx 1.7768 \text{ GeV}/c^2$	$\approx 91.19 \text{ GeV}/c^2$	
		-1	-1	-1	1	1	1	0	
		$\frac{1}{2}$	$\frac{1}{2}$	$\frac{1}{2}$	$\frac{1}{2}$	$\frac{1}{2}$	$\frac{1}{2}$	1	
		<b><math>\nu_e</math></b> electron neutrino	<b><math>\nu_\mu</math></b> muon neutrino	<b><math>\nu_\tau</math></b> tau neutrino	<b><math>\bar{\nu}_e</math></b> electron antineutrino	<b><math>\bar{\nu}_\mu</math></b> muon antineutrino	<b><math>\bar{\nu}_\tau</math></b> tau antineutrino	<b><math>W^+</math></b> $W^+$ boson	<b><math>W^-</math></b> $W^-$ boson
		$< 2.2 \text{ eV}/c^2$	$< 0.17 \text{ MeV}/c^2$	$< 18.2 \text{ MeV}/c^2$	$< 2.2 \text{ eV}/c^2$	$< 0.17 \text{ MeV}/c^2$	$< 18.2 \text{ MeV}/c^2$	$\approx 80.39 \text{ GeV}/c^2$	$\approx 80.39 \text{ GeV}/c^2$
		0	0	0	0	0	0	1	-1
		$\frac{1}{2}$	$\frac{1}{2}$	$\frac{1}{2}$	$\frac{1}{2}$	$\frac{1}{2}$	$\frac{1}{2}$	1	1
		<b><math>\nu_e</math></b> electron neutrino	<b><math>\nu_\mu</math></b> muon neutrino	<b><math>\nu_\tau</math></b> tau neutrino	<b><math>\bar{\nu}_e</math></b> electron antineutrino	<b><math>\bar{\nu}_\mu</math></b> muon antineutrino	<b><math>\bar{\nu}_\tau</math></b> tau antineutrino	<b><math>W^+</math></b> $W^+$ boson	<b><math>W^-</math></b> $W^-$ boson
		$< 2.2 \text{ eV}/c^2$	$< 0.17 \text{ MeV}/c^2$	$< 18.2 \text{ MeV}/c^2$	$< 2.2 \text{ eV}/c^2$	$< 0.17 \text{ MeV}/c^2$	$< 18.2 \text{ MeV}/c^2$	$\approx 80.39 \text{ GeV}/c^2$	$\approx 80.39 \text{ GeV}/c^2$
		0	0	0	0	0	0	1	-1
		$\frac{1}{2}$	$\frac{1}{2}$	$\frac{1}{2}$	$\frac{1}{2}$	$\frac{1}{2}$	$\frac{1}{2}$	1	1
		<b><math>\nu_e</math></b> electron neutrino	<b><math>\nu_\mu</math></b> muon neutrino	<b><math>\nu_\tau</math></b> tau neutrino	<b><math>\bar{\nu}_e</math></b> electron antineutrino	<b><math>\bar{\nu}_\mu</math></b> muon antineutrino	<b><math>\bar{\nu}_\tau</math></b> tau antineutrino	<b><math>W^+</math></b> $W^+$ boson	<b><math>W^-</math></b> $W^-$ boson

**GAUGE BOSONS**  
VECTOR BOSONS  
**SCALAR BOSONS**

Figure 1.1: List of elementary particles of the standard model, force carrying gauge bosons and Higgs boson are shown. I, II, and III represent the three generations of quarks and leptons. The figure is taken from [12].

Figure 1.1 shows a list of the elementary fermionic particles of matter, the force mediating gauge bosons, and the Higgs boson of the Standard Model. Fermions form the visible matter content of the Universe. The Standard Model includes 12 kinds of elementary fermionic particles (6 quarks and 6 leptons) and their corresponding antiparticles. These 12 kinds of elementary particles are grouped into three generations of four particles each. The gauge bosons are the force carriers. Gluons and photons carry the strong and electromagnetic forces, respectively. The  $Z^0$  and  $W^\pm$  bosons are the carriers of the weak force. The Higgs particle is a scalar boson and is produced by the quantum excitation of the Higgs field.

## 1.1 Brief Introduction to Quantum Chromodynamics

The theory that most accurately describes the physics of the strong interaction is known as the Quantum Chromodynamics (QCD) [13]. QCD is a non-Abelian gauge theory based on a local (gauge) symmetry group called  $SU(3)$ . QCD describes the interactions at two different length scales that is the force among the quarks and gluons responsible to form hadrons as well as the force among nucleons which bind together to form a nucleus.

Three kinds of charge in QCD responsible for interaction are usually referred to as the “color charge” by a loose analogy to the three kinds of color (red, green, and blue) perceived by human vision. Similar to the electric charges in quantum electrodynamics, the “color” charges are responsible for the QCD interactions. Baryons are made out of three quarks in a way that it is a color-neutral state. Similarly, mesons are also colorless states that carry quark and an anti-quark together. Due to their participation in strong interactions, baryons and mesons together are called hadrons. There are 8 gluons in total that are massless, flavorless, color-charged, and spin-1 particles.

QCD exhibits three salient properties: two related to the nature of interaction strength of the strong force and one related to the spontaneous symmetry breaking of chiral flavor symmetry. The coupling constant which reflects the interaction strength among various constituents can be expressed as  $\alpha_S$ ,

$$\alpha_S \approx \frac{12\pi}{(11n_c - 12N_f) \ln(Q^2/\Lambda_{QCD}^2)} , \quad (1.1)$$

where  $n_c$  is the number of color charges,  $N_f$  is the number of flavors,  $Q^2$  is the momentum transfer, and  $\Lambda_{QCD}$  is the QCD scale parameter (value ranges between 100 to 500 MeV). QCD predicts that  $\alpha_S$  decreases with increasing energy or momentum transfer ( $Q^2$ ), and vanishes at asymptotically high energies.

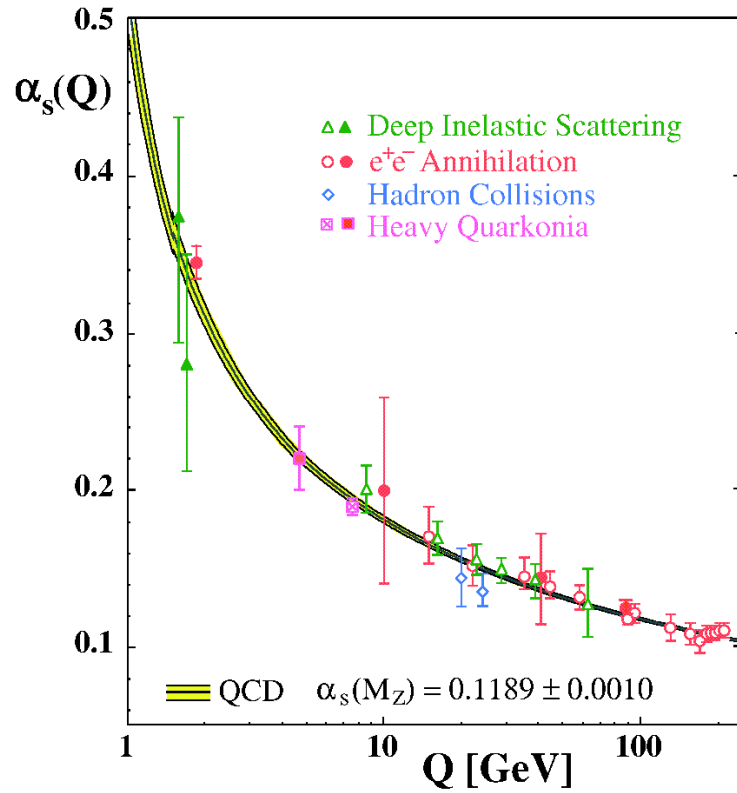


Figure 1.2:  $\alpha_s(Q)$  measured values as a function of the respective energy scale  $Q$ . The figure is taken from Ref. [14].

Figure 1.2 shows the results of  $\alpha_s(Q)$  as a function of energy scale  $Q$  from different measurements. The data are in excellent agreement with the QCD prediction, from the smallest to the largest energy scales probed by experimental data.

As the distance between two quarks increases (or momentum transfer decreases), the strength of coupling between them increases. This feature is called “Confinement”. Due to this feature color charges are always bound together to form hadrons and not found free in nature. On the other hand, as the energy scale increases and the corresponding length scale decreases, interaction strength between two color-charged particles becomes asymptotically weaker leading to quarks/gluons behaving as free non-interacting particles. This property is known as “Asymptotic Freedom” which was discovered in 1973 by David

Gross, Frank Wilczek, and David Politzer [15, 16] for which the Nobel Prize in Physics in 2004 was awarded. As a consequence of the asymptotic freedom, QCD matter at very high temperatures is speculated to be a gas consisting of free quarks and gluons.

## 1.2 Deconfinement and QCD Phase Diagram

Soon after the discovery of asymptotic freedom in non-abelian gauge theories, Collins and Perry in 1975 using the quark model predicted [17] that the superdense matter (found in neutron-star cores, exploding black holes, and the early big-bang universe) might consist of free quarks rather than hadrons. Lattice QCD (a well-established non-perturbative first principle approach to QCD [18]) predicts from hadronic matter where quarks and gluons are confined within hadrons to a deconfined state of quarks and gluons at an energy density of  $\sim 1 \text{ GeV}/fm^3$  at a critical temperature,  $T_c$  of  $\sim 170 \text{ MeV}$  [19, 20] (Note: temperature obtained for QCD with two flavors of quarks). For comparison, note that the energy density of normal cold nuclear matter is about  $0.16 \text{ GeV}/fm^3$ . With the aid of state-of-the-art computing facilities, lattice QCD calculations are able to predict  $T_c$  value with impressive precision. A recent such calculation (with three flavors of quark) of transition temperature at the zero baryon chemical potential predicts the value of  $T_c$  to be  $156.5 \pm 1.5 \text{ MeV}$  [21].

Figure 1.3 shows lattice results of the energy density and pressure (both scaled to the fourth power of temperature) as a function of temperature. The deconfining aspect of the transition at finite temperature is the sudden liberation of partonic degrees of freedom in QCD. Rapid change of bulk thermodynamic observables reflects the change in degrees of freedom. This proposed state of matter with deconfined quarks and gluons as constituents is known as Quark-Gluon Plasma (QGP). This state of matter also exhibits the so-called “Chiral Symmetry” which is spontaneously broken in the case of normal nuclear matter.

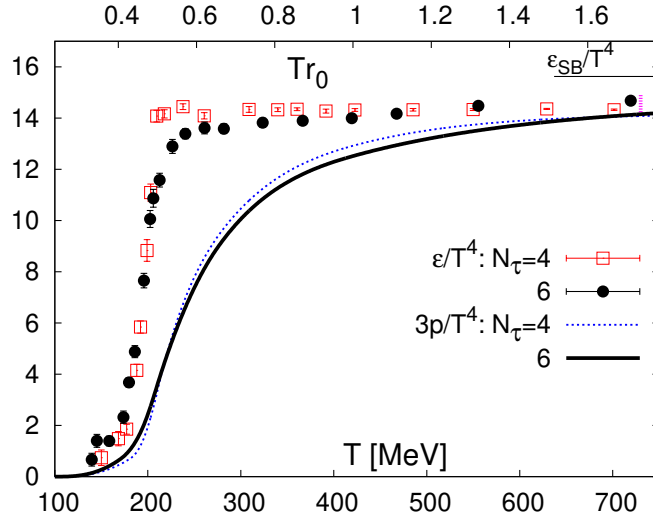


Figure 1.3: Energy density and three times the pressure divided by  $T^4$  (which scales as the number of degrees of freedom) as a function of the temperature from lattice QCD. Calculations performed on lattices with temporal extent  $N_\tau = 4$  and 6 with three flavors of quark and vanishing quark chemical potentials. Figure taken from Ref. [22].

Figure 1.4 shows a schematic phase diagram of strongly interacting matter outlined by temperature ( $T$ ) and baryon chemical potential ( $\mu_B$ ). At  $T = 0$  and  $\mu_B = 0$ , lies the QCD vacuum. Nuclear matter in the normal state is at  $T = 0$  and  $\mu_B \sim 924$  MeV [24]. Regions of very large  $T$  and  $\mu_B \sim 0$  correspond to conditions similar to the early Universe. Two distinct phases in the diagram are hadron gas, a phase where quarks and gluons are confined within hadrons, and quark-gluon plasma, a phase where quarks and gluons are deconfined. At  $\mu_B = 0$  and large  $T$ , lattice QCD calculations predict a smooth and rapid crossover between this two phases [25, 26]. Lattice QCD calculations predict a crossover till a moderate value of  $\mu_B$ . However, lattice calculations in large  $\mu_B$  regions suffer from large uncertainty because of the “sign problem” [27]. At large  $\mu_B$ , lattice QCD and QCD-based effective theory calculations indicate that the transition is of first order [28–30] in nature. The point where the first order phase transition line ends and the cross-over region starts could be the QCD

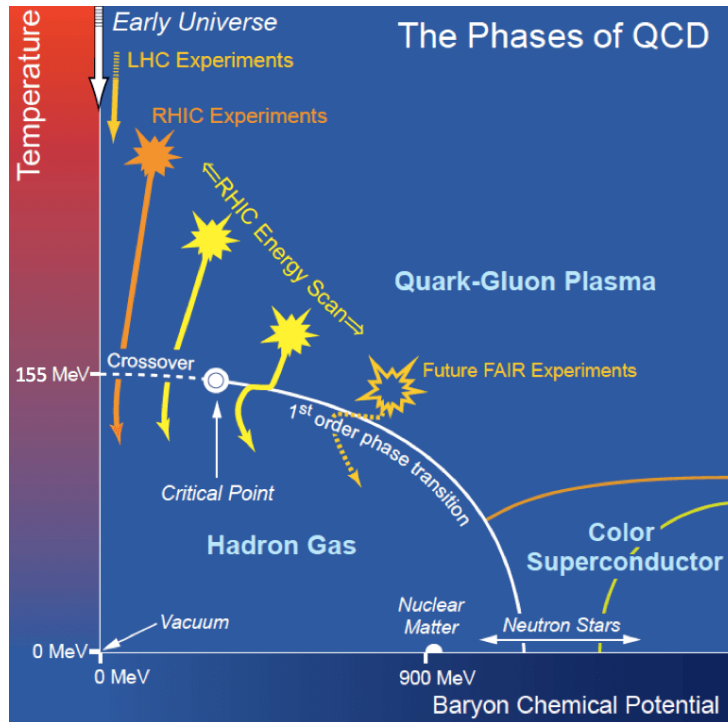


Figure 1.4: Schematic QCD phase diagram showing different phases. Phase change from a hadron gas to QGP phase via a smooth crossover, a first-order phase transition, and a possible QCD critical point are outlined in different regions of  $T$  and  $\mu_B$  much of which is accessible by the current and future experimental facilities. Figure taken from Ref. [23].

Critical Point (CP) [31]. QCD critical point is a landmark point in the QCD phase diagram. Discovery of the critical point/region will help us qualitatively predict the regions of the crossover and first-order phase transition. QCD matter at even higher density might exhibit different phase structures and discussion on them can be found in Ref. [32].

It is important to note that, to present the phase diagram in terms of the temperature and chemical potential, the assumption of thermal equilibrium is utilized. Each point in the phase diagram which has a non-zero value of  $T$  or  $\mu_B$  is a point of thermal equilibrium. The current understanding of the thermal nature of medium created in heavy-ion collisions has primarily come from the description of the experimentally measured yield of produced hadrons/light nuclei with by the different variants of statistical thermal models. In the later

sections of this chapter, we will briefly discuss this topic.

### 1.3 Relativistic Heavy Ion Collisions

As the name suggests, in relativistic heavy ion collisions, heavy nuclei (ions) are accelerated to attain relativistic energies and are collided to explore the strongly interacting matter in extreme conditions. The first experiment to perform heavy-ion collision at intermediate relativistic energies was started in the early 1970s. This was at the Bevalac experiment at Lawrence Berkeley National Laboratory (LBNL) in the USA. The Bevalac provided nuclear projectiles with an energy of about  $1A \text{ GeV}/c$  ( $A$  being the mass number of the projectile nucleus) and achieved compressed nuclear matter at a density that is a few times the normal nuclear density. Experimental programs such as Alternating Gradient Synchrotron (AGS) at Brookhaven National Laboratory (BNL), Heavy Ion Synchrotron (SIS) at Helmholtzzentrum für Schwerionenforschung (GSI), and the Super Proton Synchrotron (SPS) at European Organization for Nuclear Research (CERN) also provided colliding energy of a few GeV. Modern-day collider facilities such as the Relativistic Heavy Ion Collider (RHIC) at BNL and the Large Hadron Collider (LHC) at CERN pushed the energies of colliding heavy nuclei beams to a much higher range. Up to date, RHIC has successfully performed Au+Au, Cu+Cu, Ru+Ru, and Zr+Zr collisions at  $\sqrt{s_{\text{NN}}} = 200 \text{ GeV}$ , which is the designed top energy for heavy ion collisions. LHC has provided data for heavy-ion collisions at much higher energies such as for lead-on-lead (Pb+Pb) and xenon-on-xenon (Xe+Xe) collisions at  $\sqrt{s_{\text{NN}}} = 5.02 \text{ TeV}$  and  $5.44 \text{ TeV}$ , respectively.

### 1.3.1 Space-time Evolution

To perform relativistic heavy ion collisions, two nuclei moving in opposite directions are accelerated to nearly the speed of light. Nuclei appear as pancakes due to Lorentz contraction along the beam direction.

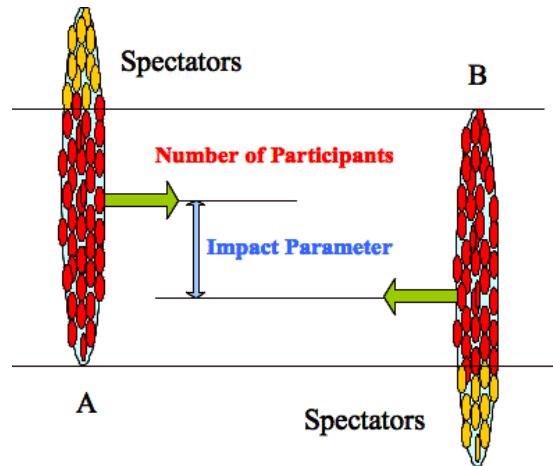


Figure 1.5: Sketch of an ultra-relativistic collision between two nuclei. The nucleons taking part in the collision are known as participants and are shown using red color. The remnant nucleons are called spectators and are shown using yellow color.

A sketch of ultra-relativistic collision between two nuclei is shown using Figure 1.5. The non-zero impact parameter of the collision characterizes the magnitude of the overlap region volume. Those nucleons (of both the nuclei) which take part in the collision are called participants, while the remaining nucleons are known as spectators. Depending on the energy density (energy/volume) deposited by the colliding nuclei in the overlap/interaction region, a deconfined medium of quarks and gluons may be produced.

Figure 1.6 shows a schematic representation of the space-time evolution of the medium created in an ultra-relativistic heavy ion collision. Consider the head-on collision of two nuclei, A and B, that are Lorentz contracted along the beam direction ( $z$ -axis), in the center-of-mass frame. Collision takes place at the point  $(z, t) = (0, 0)$ . Depending on the energy

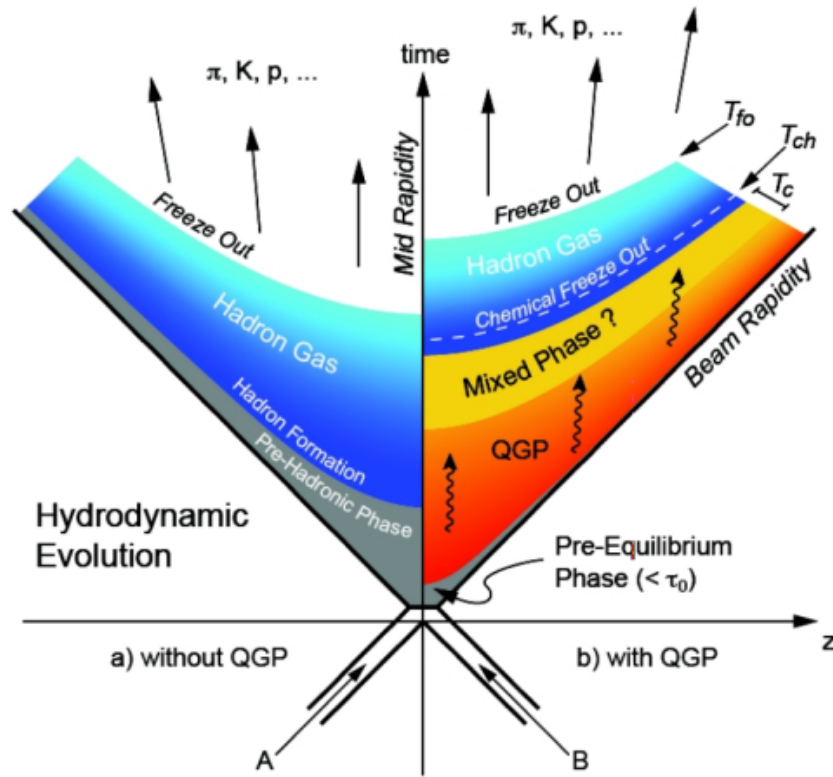


Figure 1.6: Evolution of heavy-ion collision shown as different stages using a space-time diagram.

deposited in the interaction region, at least two scenarios are possible. When the critical value required for QGP formation is not achieved, the created system can be a gas of hadrons (shown on the left-half of Figure 1.6). The other possibility is the deposition of sufficient energy per unit initial volume to produce temperature above the critical temperature  $T_c$  and a change of phase to quarks and gluons happen (shown on the right-half of the Figure 1.6). The system may not be produced into thermodynamic equilibrium. To achieve thermal equilibrium further interactions among the constituents of the medium is required. It is believed that in high energy heavy-ion collisions the interactions among quarks and gluons may bring it to local thermodynamic equilibrium even within a very small value of proper time ( $\tau_0$ ) of evolution. The medium formed in heavy-ion collisions is referred sometimes

to as a “fireball” in the literature.

The medium undergoes in a violent expansion with a speed close to that of speed of light. Relativistic hydrodynamics has been very successfully used to describe the expansion of the medium. As the fireball cools down below the critical temperature  $T_c$ , hadron formation starts. In the case of a first-order phase transition, the partonic and hadronic matter may coexist as a mixed phase. As the system of hadrons further continues to expand, at a temperature called the chemical freeze-out temperature  $T_{ch}$ , the inelastic interactions among hadrons cease, and their relative abundances become fixed. This stage in the evolution of the system is known as the “chemical freeze-out”. The expansion continues until a temperature known as the kinetic freeze-out temperature  $T_{fo}$ , where the mean free path of particles grows to similar or larger as the system size and the elastic interactions also cease. This stage is called “kinetic freeze-out”. At this last surface of scattering, finally, the particles come out of the system and stream to the detectors.

### 1.3.2 Variables of General Interest

There are a number of variables used frequently in heavy-ion collision experiments that might be of general interest and hence requires some explanation. First, it is important to note that the coordinate system in heavy-ion collision experiments is usually defined in a way that the beam axis is parallel to the  $z$ -axis. Figure 1.7 shows the typical presentation of a co-ordinate system in heavy-ion collisions.

There is also a convention that, in the collision coordinate system, the impact parameter ( $\vec{b}$ ) is along the  $\hat{x}$  direction. The primary vertex of an event is the point where a nucleus-nucleus collision happens.

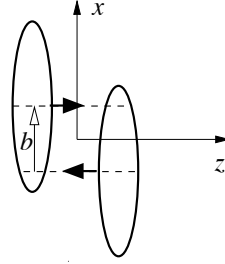


Figure 1.7: A schematic presentation of co-ordinate system for two colliding nuclei.

### 1.3.2.1 Rapidity

Rapidity,  $y$ , is defined in terms of the energy,  $E$ , and the longitudinal momentum,  $p_z$  of the particle.

$$y = \frac{1}{2} \ln \left( \frac{E + p_z c}{E - p_z c} \right), \quad (1.2)$$

where  $c$  is the velocity of light. Rapidity is a dimensionless quantity by definition. At  $p_z = 0$ ,  $y$  is zero (mid-rapidity) and at  $p_T = 0$ ,  $y$  is  $\pm\infty$ . An advantage of the rapidity variable over velocity is that it  $y$  transforms linearly, whereas the velocity transformation is done under a successive Lorentz boost which is non-linear in nature. In the former case, the shape invariance of the rapidity spectra is an advantage under Lorentz boosts. However, rapidity requires knowledge of the energy of a particle (particle identification in an experiment is needed to define  $E$ ).

### 1.3.2.2 Pseudorapidity

Pseudorapidity ( $\eta$ ) is a purely geometric approximation of the rapidity and matches with rapidity if  $\gamma = \infty$ . Measuring only the angle of the detected particle with respect to the beam axis, one can calculate  $\eta$  as,

$$\eta = -\ln \left[ \tan \left( \frac{\theta}{2} \right) \right], \quad (1.3)$$

where  $\theta$  is the angle between particle momentum and the beam axis. For  $m = 0$  or  $p \gg m$ , rapidity and pseudorapidity coincide.

### 1.3.2.3 Transverse Momentum

The momentum vector can be split into two components: longitudinal momentum, the component that is along the beam going direction, and the transverse momentum ( $p_T$ ) that is along the perpendicular direction to the beam axis. Mathematically,  $p_T = \sqrt{p_x^2 + p_y^2}$ , where  $p_x$  and  $p_y$  are components of total momentum along the  $x$  and  $y$  direction. Also the transverse momentum is invariant under Lorentz transformation.

### 1.3.2.4 Invariant Yield

The quantity  $E d^3\sigma/dp^3$ , is called the invariant (Lorentz invariant) cross-section. The invariant cross-section can be written in terms of measured invariant yield and integrated luminosity  $L_{\text{int}}$  as follows.

$$E \frac{d^3\sigma}{dp^3} = \frac{1}{L_{\text{int}}} E \frac{d^3N}{dp^3} = \frac{1}{L_{\text{int}}} \frac{1}{2\pi} \frac{d^2N}{p_T dp_T dy} \quad (1.4)$$

Invariant yield and  $L_{\text{int}}$  are measured in the experiment.

### 1.3.2.5 Particle Multiplicity

The multiplicity of a collision event is defined as the total number of particles produced in one collision. As the tracking detectors in STAR (TPC and TOF) measure only the charged particles, the name multiplicity in this thesis is used in many places to reflect the number of charged particles measured within a given acceptance for a collision event.

### 1.3.2.6 Collision Centrality

Centrality is a variable used to indicate the amount of initial overlap region when two nuclei collide. Using the impact parameter or the number of participant nucleons would be the ideal way to characterize the centrality. However, these quantities are not accessible in the experiments. Experimentally, the centrality is derived from the measured particle multiplicity distribution (Multiplicity is assumed to be a monotonic function of the impact parameter). The centrality determination technique is discussed in detail in Chapter 3.

## 1.3.3 Experimental Signatures of Quark-Gluon Plasma

The medium produced in high energy heavy ion collisions is a very short-lived, femto-scale-sized, and rapidly expanding system. The confirmation of the formation of a deconfined and local thermal equilibrated state of quarks and gluons is very challenging and requires robust experimental observables. Many signatures of QGP medium formation and related characteristic feature of the medium have been long proposed and studied [33, 34]. An older yet detailed summary of experimental measurements at the STAR experiment in the light of the search for a QGP medium can be found in Ref. [35]. In the following text, short discussion on a few widely accepted signatures of QGP medium creation are presented.

### 1.3.3.1 Transverse Momentum Spectra and Yields

The transverse momentum ( $p_T$ ) spectra of identified particles are one of the most fundamental observables in heavy-ion collisions. This can give information on particle production mechanisms and chemical/kinetic freeze-out properties. The  $p_T$  spectra are usually expressed as:

$$E \frac{d^3N}{dp^3} = \frac{1}{2\pi p_T} \frac{d^2N}{dp_T dy} , \quad (1.5)$$

where  $E$  is the particle energy and  $\frac{d^2N}{dp_T dy}$  represents the event-wise particle yield density. Transverse momentum spectra being a differential observable gives information on the dynamics of the medium. Integrated yield  $dN/dy$ , the relative abundance of yields of different particles, and mean  $p_T$  can be directly extracted from the  $p_T$  spectra measurements.

The particle yields and their ratios can probe the chemical freeze-out surface, as this is the surface where the chemical composition of the medium stops changing. With the assumption of thermal and chemical equilibrium at this stage, statistical thermal models [36–38] can constrain the system temperature and the chemical potentials.

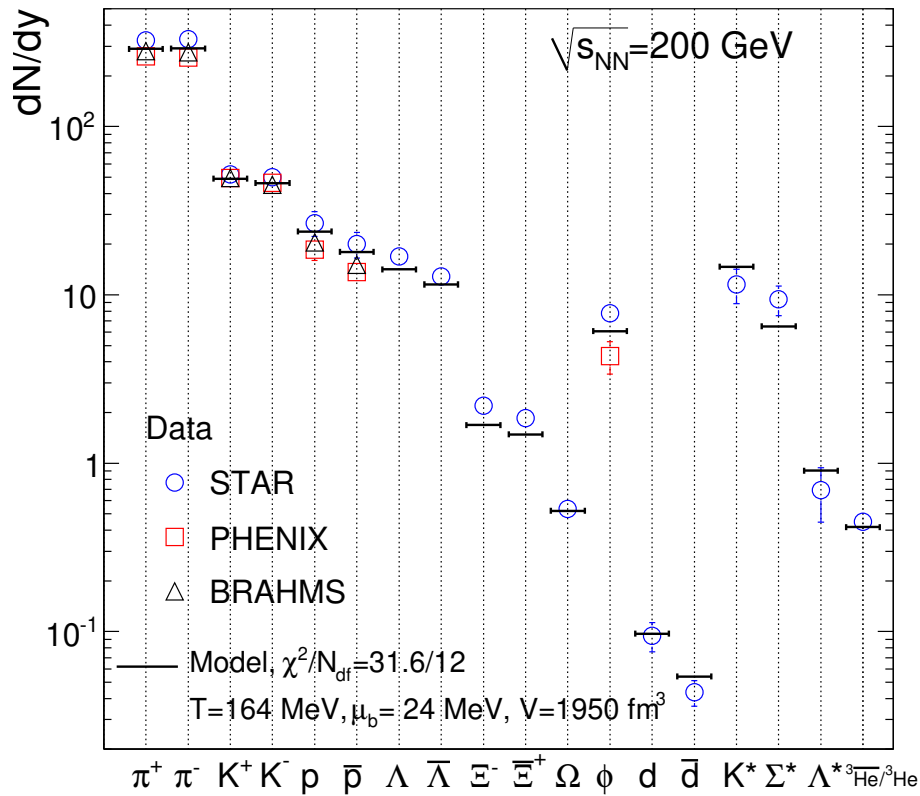


Figure 1.8: Yields from the statistical thermal model compared to experimental data from central Au+Au collisions at  $\sqrt{s_{NN}} = 200$  GeV. Figure is taken from Ref. [39].

Figure 1.8 shows comparison of the experimental  $p_T$  integrated yields of several hadrons and ratio of  ${}^3\text{He}/{}^3\text{He}$  measured for most central Au+Au collisions at  $\sqrt{s_{\text{NN}}} = 200$  GeV in the experiments at RHIC [39]. The horizontal lines are the statistical model best fit values. Model parameters are the chemical freezeout temperature,  $T_{ch} = 164 \pm 4$  MeV, baryon chemical potential,  $\mu_B = 24 \pm 4$  MeV, and strangeness saturation factor,  $\gamma_S = 0.99 \pm 0.07$  [35]. The temperature deduced from the fits is similar to the value predicted by lattice QCD for a QGP to hadron gas transition. The value of the strangeness saturation factor (which is a non-equilibrium parameter) is close to 1, which implies that the strange sector in the matter formed in most central Au+Au collisions at  $\sqrt{s_{\text{NN}}} = 200$  GeV in RHIC also might be in thermal equilibrium.

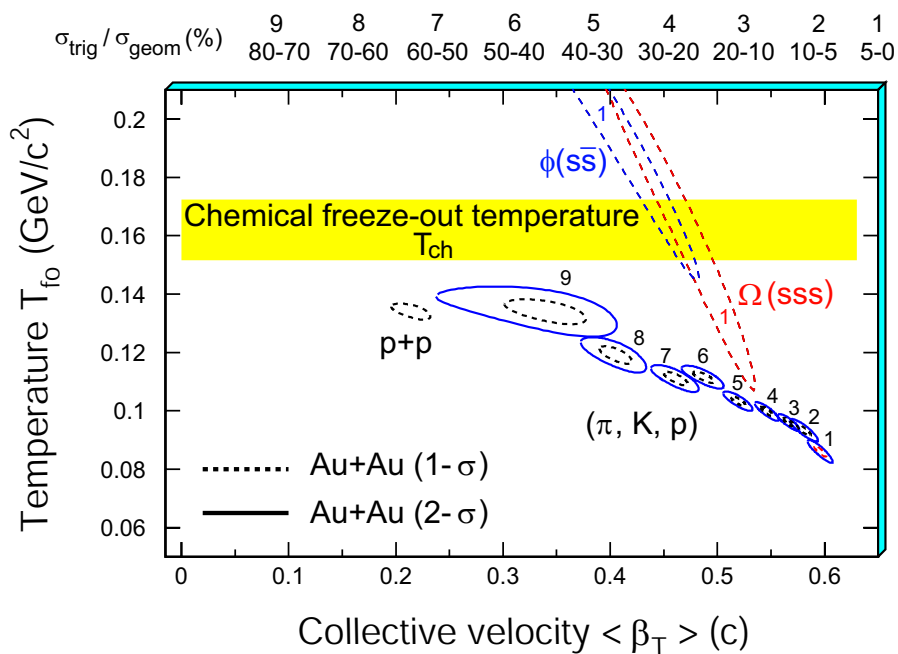


Figure 1.9: Contours of kinetic freezeout temperature  $T_{fo}$  and average radial flow velocity  $\langle \beta_T \rangle$  extracted from thermal + radial flow fits of  $p_T$  spectra of many light and multi-strange hadrons produced in  $\sqrt{s_{\text{NN}}} = 200$  GeV Au+Au collisions. The figure is taken from Ref. [35].

Transverse momentum distributions are important observables to probe the kinetic

freeze-out surface of the medium as these distributions become fixed at this surface. The measured particle spectra of various hadron species are compared to those obtained from a blast-wave model with a certain flow profile of the medium and the model parameters being the kinetic freezeout temperature  $T_{f0}$  and average radial flow velocity  $\langle\beta_T\rangle$ .

Figure 1.9 shows results for these parameters shown for different collision centralities and different produced particle species for Au on Au collisions at  $\sqrt{s_{NN}} = 200$  GeV. From peripheral to central collisions, the temperature of the system grows cooler at kinetic freezeout and develops stronger collective flow. This indicates the system created in central collisions expands faster than in peripheral collisions. The  $\phi$  and  $\Omega$  hadrons which do not contain open  $u$  and  $d$  quarks were predicted to have diminished hadronic interactions. However, these particles show substantial radial flow velocities that might come from their greater sensitivity to collective behavior during earlier partonic stages [35].

### 1.3.3.2 Collectivity

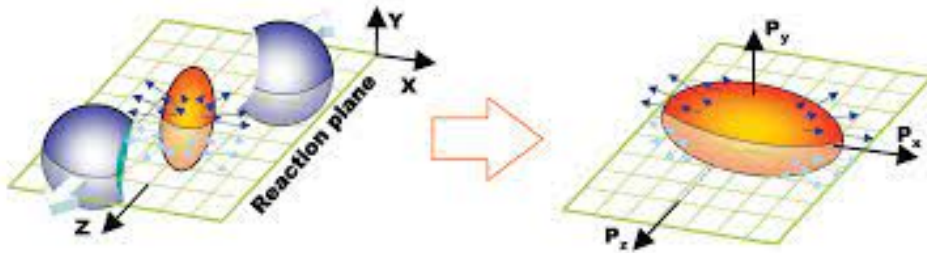


Figure 1.10: Schematic diagram showing the transformation of coordinate space anisotropy in the initial state into a momentum space anisotropy for non-central nucleus-nucleus collision.

In non-central nucleus-nucleus collisions, the overlap region is spatially asymmetric with an almond-like shape as shown in Figure 1.10. The system is surrounded by a vacuum and the interactions among constituents of the system generate a pressure gradient from

the dense center to the boundary. The pressure gradient along the short axis is larger than that along the longer axis, transforming initial spatial asymmetry into momentum anisotropy. The azimuthal distribution of final state particles may shed light about the early-state pressure achieved in such collisions.

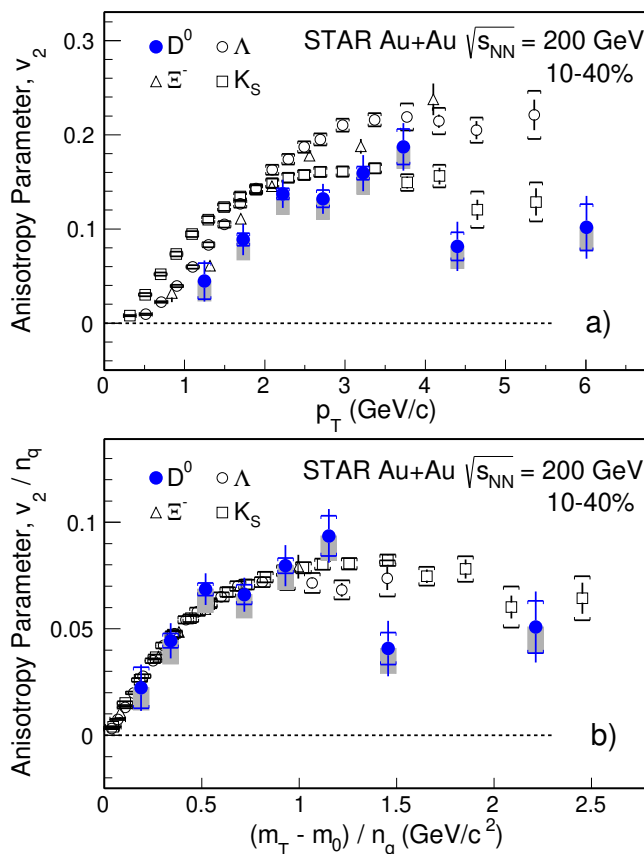


Figure 1.11: (Top panel)  $v_2$  as a function of  $p_T$  and (Bottom panel)  $v_2/n_q$  as a function of  $(m_T - m_0)/n_q$  for  $D^0$ ,  $K_S^0$ ,  $\Lambda$ , and  $\Xi^-$  in 10–40% centrality Au+Au collisions at  $\sqrt{s_{NN}} = 200$  GeV. Figure taken from Ref. [40].

The azimuthal angle distribution of final state particles can be decomposed via Fourier expansion. The expansion coefficients of the Fourier series characterise the different

harmonics of the flow.

$$E \frac{d^3 N}{dp^3} = \frac{1}{2\pi p_T} \frac{d^2 N}{dp_T dy} \left( 1 + \sum_{n=1}^{\infty} 2v_n \cos [n(\phi - \psi_{rp})] \right), \quad (1.6)$$

where  $v_n$  is the  $n^{\text{th}}$  harmonic coefficient,  $\phi$  is the azimuthal angle of the particle, and  $\psi_{rp}$  is the reaction plane angle subtended by the impact parameter vector in the plane transverse to the beam direction. The coefficients  $v_1$  and  $v_2$  are known as the directed flow and elliptic flow, respectively.

Figure 1.11 (top panel) shows that the particles have large elliptic flow values [40]. Even the charm meson  $D^0$  shows collectivity similar to those for lower mass hadrons. The mass ordering observed in the region  $p_T < 2 \text{ GeV}/c$ , is a characteristic of the hydrodynamic evolution of the QGP medium [41]. Elliptic flow values scaled to the number of constituent quarks are shown in the bottom panel of Figure 1.11. Scaled  $v_2$  of all hadrons falls on the same universal trend at least up to  $(m_T - m_0)/n_q < 1 \text{ GeV}/c^2$ , which is a strong piece of evidence for the formation of a hydrodynamically expanding QGP phase with partonic degrees of freedom.

## 1.4 Higher Moments of Fluctuations

In the theory of statistics [42], moments of a distributions are understood to describe its location and dispersion. The first moment is the mean. The mean of a distribution is the one of primary locations for a distribution. Next-order moments, in general, are defined around the mean value. They are called central moments. The second central moment,  $\sigma^2$ , is well known as variance and used to characterize the width of a distribution. The skewness ( $S$ ) and kurtosis ( $\kappa$ ) are used to measure the tailedness and peaked-ness from the mean value, respectively. Apart from the moments, measures such as the so-called cumulants are better observables that are more useful from a theoretical standpoint. In heavy-ion collision

physics, the cumulants (and their ratios) of QCD conserved charges, such as net-baryon, net-charge, and net-strangeness are suggested to probe the QCD phase transitions. In this section, we will discuss the definitions and properties of the moments and cumulants, and their connections to the thermodynamics of the system formed in heavy-ion collisions.

## 1.4.1 Cumulants and Moments

### 1.4.1.1 Definitions

Starting from the cumulant-generating function [43] of any probability distribution, all order cumulants can be obtained. Let  $f(X)$  be a probability density distribution of a random variable  $X$ . The cumulant generating function (the natural logarithm of the moment generating function) is defined as:

$$K(t) = \log E(e^{tX}), \quad (1.7)$$

where  $E$  is the expectation operator often symbolized by angular brackets  $\langle \dots \rangle$ , such that  $E(e^{tX}) = \langle e^{tX} \rangle \equiv \int_{-\infty}^{+\infty} e^{tX} f(X) dX$ , for a real-valued continuous probability density function  $f(X)$ , and  $t$  is an auxiliary variable.

Any  $n^{th}$  order cumulant,  $C_n$ , can be obtained by differentiating the above expression  $n$  times and evaluating the result at zero:

$$C_n = K^{(n)}(t=0) = \left. \frac{\partial^n K(t)}{\partial t^n} \right|_{t=0} \quad (1.8)$$

The moment-generating function for moments about zero can be written in the series form as:

$$M(t) = E(e^{tX}) = 1 + \sum_{n=1}^{\infty} \langle X^n \rangle \frac{t^n}{n!} \quad (1.9)$$

Consequently, the  $n^{th}$  order moments about zero,  $\mu'_n = \langle X^n \rangle$  can be obtained as:

$$\mu'_n = \langle X^n \rangle = M^{(n)}(t=0) = \left. \frac{\partial^n M(t)}{\partial t^n} \right|_{t=0} \quad (1.10)$$

Using the expressions for generating functions, cumulants of any order can be derived. Below, we write the expressions for cumulants up to 4<sup>th</sup> order in terms of moments about zero and in terms of central moments (moments about the mean),  $\mu_n = \langle (X - \langle X \rangle)^n \rangle = \langle (\delta X)^n \rangle$ .

$$C_1 = \mu'_1 = \langle X \rangle, \quad (1.11)$$

$$C_2 = \mu'_2 - \mu_1'^2 = \langle (X - \langle X \rangle)^2 \rangle, \quad (1.12)$$

$$C_3 = \mu'_3 - 3\mu'_2\mu'_1 + 2\mu_1'^3 = \langle (X - \langle X \rangle)^3 \rangle, \quad (1.13)$$

$$C_4 = \mu'_4 - 4\mu'_3\mu'_1 - 3\mu_2'^2 + 12\mu_2'\mu_1'^2 - 6\mu_1'^4 \quad (1.14)$$

$$= \langle (X - \langle X \rangle)^4 \rangle - 3\langle (X - \langle X \rangle)^2 \rangle^2 \quad (1.15)$$

Similarly, mixed cumulants representing the correlations among different variables can also be defined. Let us consider two random variables  $X$  and  $Y$ , then the mixed cumulant can be defined as:

$$C_{1X,1Y} = \langle \delta X \delta Y \rangle = \langle XY \rangle - \langle X \rangle \langle Y \rangle. \quad (1.16)$$

Further, higher-order mixed cumulants can be written as:

$$C_{1X,2Y} = \langle \delta X (\delta Y)^2 \rangle, \quad (1.17)$$

$$C_{2X,2Y} = \langle (\delta X)^2 (\delta Y)^2 \rangle - 2\langle \delta X \delta Y \rangle^2 - \langle (\delta X)^2 \rangle \langle (\delta Y)^2 \rangle, \quad (1.18)$$

$$C_{1X,3Y} = \langle (\delta X) (\delta Y)^3 \rangle - 3\langle \delta X \delta Y \rangle \langle (\delta Y)^2 \rangle, \quad (1.19)$$

where the  $\delta X = X - \langle X \rangle$  and  $\delta Y = Y - \langle Y \rangle$ .

Usually, to describe the shape of the distributions the central moments are found to be more useful than the moments about zero. The second central moment (known as the variance  $\sigma^2$ ) is a measure of the width of a distribution. Skewness ( $S$ ) is defined as the ratio of third order central moment to the third power of  $\sigma$ . Similarly, kurtosis ( $\kappa$ ) is defined as

the ratio of fourth order cumulant to the square of second order cumulant. They can be defined as:

$$\sigma^2 = \langle(\delta X)^2\rangle = C_2 \quad (1.20)$$

$$S = \frac{\langle(\delta X)^3\rangle}{\sigma^3} = \frac{C_3}{C_2^{3/2}} \quad (1.21)$$

$$\kappa = \frac{\langle(\delta X)^4\rangle}{\sigma^4} - 3 = \frac{C_4}{C_2^2} \quad (1.22)$$

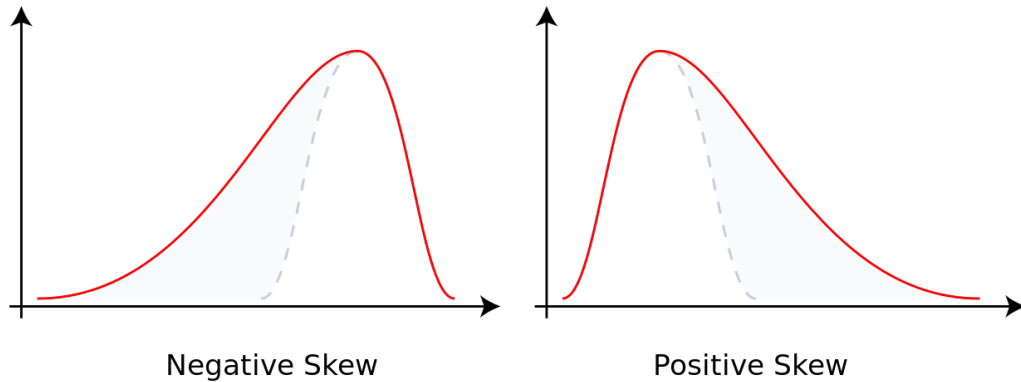


Figure 1.12: Distributions showing negative skewness (in the left panel) and positive skewness (in the right panel). Source of the figure is at [44].

Figure 1.12 is a visual example showing two kinds of skewness (+ve and -ve) for distributions. The distribution shown in the left panel has a longer tail to the left and the bulk of the distribution is tilted to the right side, which gives a negative skewness. The distribution shown in the right panel has a longer right tail and the bulk is tilted towards the left giving rise to a positive skewness. If a distribution is relatively even in concentration on both sides of the mean, the skewness will be zero, however, not necessarily imply a symmetric distribution.

Figure 1.13 shows the kurtosis of distributions that are symmetric and with unity variance and zero mean and skewness. As can be seen, the distributions with a sharper

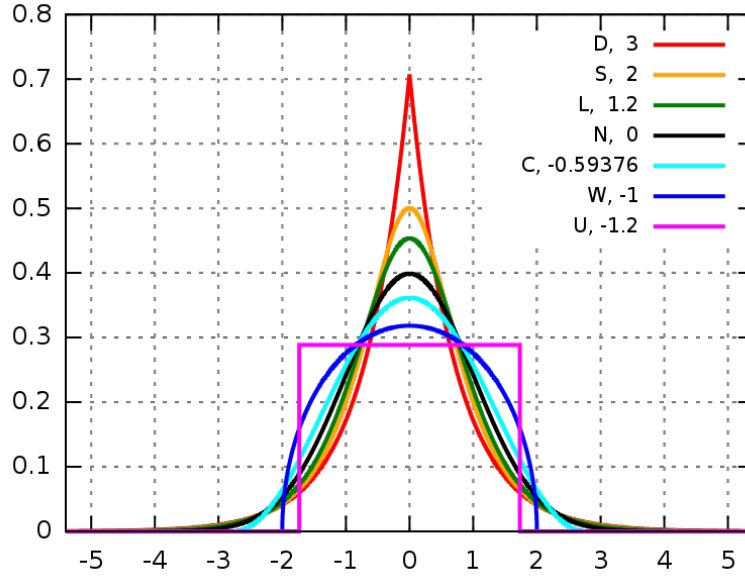


Figure 1.13: Visual example of kurtosis for seven well-known distributions from different parametric family. The figure is taken from [45].

peak have a larger value of kurtosis. The values of kurtosis for Laplace distribution (shown using red curve), normal distribution (shown using black curve) and uniform distribution (shown using magenta curve) are 3, 0, and -1.2, respectively.

For normal distributions, both, the skewness and the kurtosis are equal to zero. Therefore the higher order moments are useful to measure the non-gaussianity.

#### 1.4.1.2 Properties of Cumulants

We will introduce a few important properties of cumulants which will be used in our following analysis. The cumulants enjoy the following properties:

1. Translation-invariance: If  $C_n$  is the  $n^{\text{th}}$  order cumulant of the probability distribution of the random variable  $X$ , then for any constant  $c$  (i.e. not random),

$$C_n(X + c) = C_n(X), \quad n > 1. \quad (1.23)$$

while for  $n = 1$ , we have  $C_n(X + c) = C_n(X) + c$ . In other words, shifting a random variable (adding  $c$ ) by a constant, shifts the first cumulant (the mean) and doesn't affect higher orders.

2. Homogeneity: For any constant  $c$  we have,

$$C_n(cX) = c^n C_n(X) \quad (1.24)$$

This means the  $n^{\text{th}}$  order cumulant is homogeneous of degree  $n$ .

3. Additivity: If two random variables  $X$  and  $Y$  are independent we have,

$$C_n(X + Y) = C_n(X) + C_n(Y) , \quad (1.25)$$

*i.e* cumulant of any order is cumulative – hence the name [46].

## 1.4.2 Connection to the Thermodynamic Susceptibilities

Conserved charge number susceptibilities that are calculable in theoretical models are related to their cumulants. The susceptibility of  $n^{\text{th}}$  order,  $\chi_X^{(n)}$ , is defined as the derivative of free energy density or pressure ( $P$ ), of a thermodynamic system at a given temperature ( $T$ ) with respect to the chemical potential ( $\mu$ ). For example, susceptibilities corresponding to conserved charges of QCD such as net-baryon, net-charge, and net-strangeness numbers in lattice QCD and Hadron Resonance Gas (HRG) model can be obtained as [47, 48],

$$\chi_X^{(n)} = \frac{d^n [P/T^4]}{d(\mu_X/T)^n} , \quad (1.26)$$

where  $P/T^4$  and  $\mu/T$  are dimensionless pressure and reduced chemical potential, respectively. Index  $X$  corresponds to any conserved charges.

In a grand canonical ensemble, the thermodynamic pressure ( $P$ ) can be obtained from the logarithm of the partition function in the limit of large volume as,

$$\frac{P}{T^4} = \frac{1}{VT^3} \ln Z(T, \mu, V) \quad (1.27)$$

Cumulants of the conserved charge multiplicity distribution can be related to the corresponding number susceptibilities as follows.

$$C_n^X = VT^3 \chi_X^{(n)} \quad (1.28)$$

As can be seen from the above equation, cumulants of extensive quantities directly depend on the system volume. It is very difficult to determine the volume experimentally, therefore one uses the ratios as suggested in [49].

$$\frac{C_2}{C_1} = \frac{\sigma^2}{M} = \frac{\chi^{(2)}}{\chi^{(1)}}, \quad \frac{C_3}{C_2} = S\sigma = \frac{\chi^{(3)}}{\chi^{(2)}}, \quad \text{and} \quad \frac{C_4}{C_2} = \kappa\sigma^2 = \frac{\chi^{(4)}}{\chi^{(2)}} \quad (1.29)$$

The above relations are useful for a direct comparison of the experimental measurements to corresponding susceptibilities that are calculated in lattice-QCD, HRG, and various QCD-based models. Such comparisons, however, are subjected to certain caveats. Experimental measurements are within certain acceptance in the phase space and measure fluctuations in proxies (detectable charged particles) of conserved charges. In addition, the experimental measurements might contain effects from finite volume and global charge conservation that should be accounted for in theory calculations.

Lattice QCD [50], as well as several QCD-based theory calculations [51, 52], suggest that higher order cumulants of event-by-event fluctuations of conserved charges in QCD are sensitive observables to search for signals of QCD crossover. Similarly, to search for the QCD critical point, higher-order cumulants of several observables have been proposed [53, 54]. The quartic cumulant of event-by-event net-proton distributions has gained special interest due to its strong sensitivity to the critical correlation length [55]. A qualitative feature near the CP is a non-monotonic energy dependence of the normalized kurtosis of net-proton distribution [56].

## 1.5 Thesis Physics Motivation

### 1.5.1 Probing Light Nuclei Production via Fluctuations

Fluctuation observables are predicted to be sensitive to the production mechanism of light nuclei in high-energy heavy ion collisions. Despite the freeze-out temperatures being of the order of 100 MeV, objects like deuterons, tritons, and other light nuclei which have binding energies of the order of a few MeVs are produced in such collisions [57, 58]. Interestingly, the yields of light nuclei can also be explained in the thermal models with the same freeze-out temperatures extracted using hadronic yield. The production mechanism of light nuclei is commonly discussed in two approaches: *thermal model* and *coalescence model*. The thermal model treats light nuclei as any other hadrons and their masses and quantum numbers are inputs to the model. In the coalescence model, nuclei are formed by protons and neutrons which are nearby in phase space. Both approaches have been fairly successful to describe the experimental data on light nuclei [57, 59]. However, the complete picture of light nuclei production in heavy-ion collisions is still to be understood.

Recently, it has been suggested that higher order cumulants of deuteron number could serve as a potential probe to test different production scenarios [60]. Cumulant ratios of deuteron number in a coalescence picture are predicted to show excess above the grand-canonical thermal model baseline, which is at unity. Also, the Pearson correlation coefficient of proton and deuteron numbers is predicted to have distinct nature in two of the production scenarios. Further, deuteron production is expected to be sensitive to a QCD critical point and first-order phase transition via enhancement of pre-clusters [61, 62]. Specific combinations of yields of proton, deuteron, and triton are constructed to probe neutron density fluctuations [63] that might arise due to phase transitions. As deuteron carries two baryons, their cumulants might add to our current understanding of baryon

number fluctuations in high-energy heavy ion collisions.

We performed the first measurements of cumulants of deuteron number up to 4<sup>th</sup> order and proton-deuteron correlation in Au+Au collisions for a wide range of collision energies by utilizing the data taken in phase-I of the Beam Energy Scan (BES-I) program at RHIC. These measurements are also compared with corresponding calculations from different production models of light nuclei. This study is presented in detail in Chapter 3 of this thesis.

### 1.5.2 Freeze-out and Thermalization

At the core of the searches for different phase structures in the QCD phase diagram, lies one of the most exploited assumptions, that is the system formed in heavy-ion collisions is at/near the thermal equilibrium at the chemical-freezeout surface. Lattice QCD for example calculates all possible thermodynamic observables with an assumption of a thermalized fireball characterized only by temperature and baryonic chemical potential. Similarly, freeze-out curves deduced from hadron abundances are interpreted as the true temperature and chemical potential of the thermodynamic equilibrium of the fireball. However, there is no apparent physical reason or theoretical proof that the system formed in heavy-ion collisions has to attain thermal equilibrium [64].

Figure 1.14 shows the comparison of measured yields in the ALICE experiment with the best fit values of those calculated in a statistical thermal model [65]. Data and the thermal model show impressive agreement. Yield values that range over nine orders of magnitude, including those of strange and non-strange mesons, strange and multi-strange baryons as well as light nuclei and hypernuclei can be explained purely from the effect of thermal equilibrium. A similar agreement between the thermal model and data has been observed in a wide range of collision energies [66, 67]. Further, the thermal models with

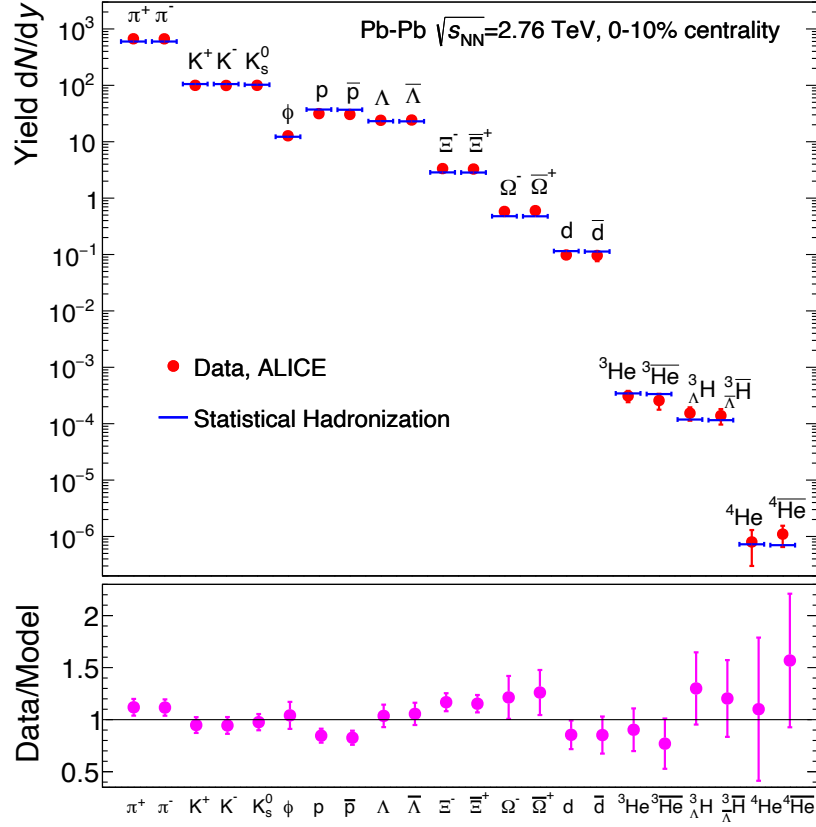


Figure 1.14: Best fit values of yields from the thermal statistical model compared to experimentally measured yields in the ALICE experiment for central Pb+Pb collisions at  $\sqrt{s_{NN}} = 2.76$  TeV. The figure is taken from Ref. [65].

blast-wave type radial flow feature also work well to explain the measured  $p_T$  spectra of several particle species. The kinetic-freezeout temperature and average radial flow velocity extracted from such a comparison are shown earlier in the text in Figure 1.9.

At the same time, mean yields in small systems such as  $e^+e^-$  and  $p + p(\bar{p})$  collisions at relatively lower  $\sqrt{s_{NN}}$ , where one does not expect the thermalized matter to be formed [68–70] can also be explained by the thermal model. Similarly, the mean yields of produced particles in highly peripheral collisions can also be described using thermal models. These observations introduce ambiguity in the interpretation of the freeze-out parameters as

thermodynamic conditions. We ask for much stricter criteria for defining the thermal equilibrium of the system. Ideally for a system in thermal equilibrium, in addition to the mean, the higher orders of the moments of the multiplicity distribution of produced particles should also show agreement with thermal models.

We perform a test by asking whether a common thermodynamic equilibrium description of fluctuations in addition to the mean particle number is possible in heavy-ion collisions [71]. Higher moments of a distribution probe the finer into the thermodynamics of a system. If the medium is thermalized well enough, not only the mean but the higher-order cumulants, which represent the tails of a distribution can also be explained by only thermodynamic effects. This study is presented in detail in Chapter 4 of the thesis.

## 1.6 Organization of the Thesis

The topics reported here broadly deals with the study of fluctuations and correlation observables to understand the chemical freeze-out, thermalization, and the production mechanism of light nuclei in high-energy heavy ion collisions. The data analyzed and presented in this thesis is recorded by the STAR detector at RHIC over many years. The collider facility RHIC and the different parts of the STAR are discussed in detail in Chapter 2. In Chapter 3, data analysis methods used to measure the higher moments of deuteron fluctuations and correlation in Au+Au collisions is discussed in detail. The results on deuteron cumulants up to 4<sup>th</sup> order, their ratios, and proton-deuteron correlations are presented. The measurements are compared to calculations from a thermal model in both grand-canonical and canonical ensemble set-ups, the Ultra-relativistic Quantum Molecular Dynamics (UrQMD) model combined with a phase-space coalescence mechanism, and a coalescence toy model simulation. In Chapter 4, we present a study on the test for a

common thermal description of fluctuations in addition to the mean particle number. A huge set of measurements from the STAR experiment are utilized to test the thermalization of matter formed at RHIC in Au+Au collisions at  $\sqrt{s_{\text{NN}}} = 7.7$  to 200 GeV. Transport model calculations are also tested for the stability of the thermal model results. The physics implications of thermalization and deviations from the thermal equilibrium in the context of the search for the QCD critical point are discussed. Finally, in Chapter 5 we present a summary and the conclusions.

## Bibliography

- [1] Chen-Ning Yang and Robert L. Mills. “Conservation of Isotopic Spin and Isotopic Gauge Invariance”. *Phys. Rev.* 96 (1954). Ed. by Jong-Ping Hsu and D. Fine, 191–195.
- [2] C. S. Wu, E. Ambler, R. W. Hayward, et al. “Experimental Test of Parity Conservation in  $\beta$  Decay”. *Phys. Rev.* 105 (1957), 1413–1414.
- [3] S. L. Glashow. “Partial Symmetries of Weak Interactions”. *Nucl. Phys.* 22 (1961), 579–588.
- [4] Abdus Salam and John Clive Ward. “Electromagnetic and weak interactions”. *Phys. Lett.* 13 (1964), 168–171.
- [5] Steven Weinberg. “A Model of Leptons”. *Phys. Rev. Lett.* 19 (1967), 1264–1266.
- [6] F. Abe et al. “Observation of top quark production in  $\bar{p}p$  collisions”. *Phys. Rev. Lett.* 74 (1995), 2626–2631. arXiv: [hep-ex/9503002](#).
- [7] K. Kodama et al. “Observation of tau neutrino interactions”. *Phys. Lett. B* 504 (2001), 218–224. arXiv: [hep-ex/0012035](#).
- [8] Georges Aad et al. “Observation of a new particle in the search for the Standard Model Higgs boson with the ATLAS detector at the LHC”. *Phys. Lett. B* 716 (2012), 1–29. arXiv: [1207.7214 \[hep-ex\]](#).

- [9] Serguei Chatrchyan et al. “Observation of a New Boson at a Mass of 125 GeV with the CMS Experiment at the LHC”. *Phys. Lett. B* 716 (2012), 30–61. arXiv: [1207.7235](https://arxiv.org/abs/1207.7235) [hep-ex].
- [10] Peter W. Higgs. “Broken symmetries, massless particles and gauge fields”. *Phys. Lett.* 12 (1964), 132–133.
- [11] Peter W. Higgs. “Broken Symmetries and the Masses of Gauge Bosons”. *Phys. Rev. Lett.* 13 (1964). Ed. by J. C. Taylor, 508–509.
- [12] [https://en.wikipedia.org/wiki/Standard\\_Model](https://en.wikipedia.org/wiki/Standard_Model).
- [13] P M Zerwas and H A Kastrup. *QCD — 20 Years Later*. WORLD SCIENTIFIC, 1993. eprint: <https://www.worldscientific.com/doi/pdf/10.1142/1755>.
- [14] Siegfried Bethke. “Experimental tests of asymptotic freedom”. *Prog. Part. Nucl. Phys.* 58 (2007), 351–386. arXiv: [hep-ex/0606035](https://arxiv.org/abs/hep-ex/0606035).
- [15] David J. Gross and Frank Wilczek. “Ultraviolet Behavior of Nonabelian Gauge Theories”. *Phys. Rev. Lett.* 30 (1973). Ed. by J. C. Taylor, 1343–1346.
- [16] H. David Politzer. “Reliable Perturbative Results for Strong Interactions?” *Phys. Rev. Lett.* 30 (1973). Ed. by J. C. Taylor, 1346–1349.
- [17] John C. Collins and M. J. Perry. “Superdense Matter: Neutrons Or Asymptotically Free Quarks?” *Phys. Rev. Lett.* 34 (1975), 1353.
- [18] Rajan Gupta. “Introduction to lattice QCD: Course”. *Les Houches Summer School in Theoretical Physics, Session 68: Probing the Standard Model of Particle Interactions*. July 1997, 83–219. arXiv: [hep-lat/9807028](https://arxiv.org/abs/hep-lat/9807028).
- [19] Frithjof Karsch. “Lattice results on QCD thermodynamics”. *Nucl. Phys. A* 698 (2002). Ed. by T. J. Hallman, D. E. Kharzeev, J. T. Mitchell, et al., 199–208. arXiv: [hep-ph/0103314](https://arxiv.org/abs/hep-ph/0103314).
- [20] Sourendu Gupta, Xiaofeng Luo, Bedangadas Mohanty, et al. “Scale for the Phase Diagram of Quantum Chromodynamics”. *Science* 332 (2011), 1525–1528. arXiv: [1105.3934](https://arxiv.org/abs/1105.3934) [hep-ph].
- [21] A. Bazavov et al. “Chiral crossover in QCD at zero and non-zero chemical potentials”. *Phys. Lett. B* 795 (2019), 15–21. arXiv: [1812.08235](https://arxiv.org/abs/1812.08235) [hep-lat].

- [22] M. Cheng et al. “The QCD equation of state with almost physical quark masses”. *Phys. Rev. D* 77 (2008), 014511. arXiv: [0710.0354 \[hep-lat\]](#).
- [23] Yasuyuki Akiba et al. “The Hot QCD White Paper: Exploring the Phases of QCD at RHIC and the LHC” (Feb. 2015). arXiv: [1502.02730 \[nucl-ex\]](#).
- [24] Kenji Fukushima and Tetsuo Hatsuda. “The phase diagram of dense QCD”. *Rept. Prog. Phys.* 74 (2011), 014001. arXiv: [1005.4814 \[hep-ph\]](#).
- [25] Frank R. Brown, Frank P. Butler, Hong Chen, et al. “On the existence of a phase transition for QCD with three light quarks”. *Phys. Rev. Lett.* 65 (1990), 2491–2494.
- [26] Y. Aoki, G. Endrodi, Z. Fodor, et al. “The Order of the quantum chromodynamics transition predicted by the standard model of particle physics”. *Nature* 443 (2006), 675–678. arXiv: [hep-lat/0611014](#).
- [27] Owe Philipsen. “Lattice calculations at non-zero chemical potential: The QCD phase diagram”. *PoS CONFINEMENT8* (2008), 011.
- [28] Shinji Ejiri. “Canonical partition function and finite density phase transition in lattice QCD”. *Phys. Rev. D* 78 (2008), 074507. arXiv: [0804.3227 \[hep-lat\]](#).
- [29] Yoshitaka Hatta and Takashi Ikeda. “Universality, the QCD critical / tricritical point and the quark number susceptibility”. *Phys. Rev. D* 67 (2003), 014028. arXiv: [hep-ph/0210284](#).
- [30] E. Scott Bowman and Joseph I. Kapusta. “Critical Points in the Linear Sigma Model with Quarks”. *Phys. Rev. C* 79 (2009), 015202. arXiv: [0810.0042 \[nucl-th\]](#).
- [31] Mikhail A. Stephanov. “QCD phase diagram and the critical point”. *Prog. Theor. Phys. Suppl.* 153 (2004). Ed. by Berndt Muller and C. I. Tan, 139–156. arXiv: [hep-ph/0402115](#).
- [32] Krishna Rajagopal and Frank Wilczek. “The Condensed matter physics of QCD”. *At the frontier of particle physics. Handbook of QCD. Vol. 1-3*. Ed. by M. Shifman and Boris Ioffe. Nov. 2000, pp. 2061–2151. arXiv: [hep-ph/0011333](#).
- [33] John W. Harris and Berndt Muller. “The Search for the quark - gluon plasma”. *Ann. Rev. Nucl. Part. Sci.* 46 (1996), 71–107. arXiv: [hep-ph/9602235](#).

- [34] S. A. Bass, M. Gyulassy, Horst Stoecker, et al. “Signatures of quark gluon plasma formation in high-energy heavy ion collisions: A Critical review”. *J. Phys. G* 25 (1999), R1–R57. arXiv: [hep-ph/9810281](https://arxiv.org/abs/hep-ph/9810281).
- [35] John Adams et al. “Experimental and theoretical challenges in the search for the quark gluon plasma: The STAR Collaboration’s critical assessment of the evidence from RHIC collisions”. *Nucl. Phys. A* 757 (2005), 102–183. arXiv: [nucl-ex/0501009](https://arxiv.org/abs/nucl-ex/0501009).
- [36] J. Cleymans and K. Redlich. “Chemical and thermal freezeout parameters from 1-A/GeV to 200-A/GeV”. *Phys. Rev. C* 60 (1999), 054908. arXiv: [nucl-th/9903063](https://arxiv.org/abs/nucl-th/9903063).
- [37] P. Braun-Munzinger, D. Magestro, K. Redlich, et al. “Hadron production in Au - Au collisions at RHIC”. *Phys. Lett. B* 518 (2001), 41–46. arXiv: [hep-ph/0105229](https://arxiv.org/abs/hep-ph/0105229).
- [38] Nu Xu and Masashi Kaneta. “Hadron freezeout conditions in high-energy nuclear collisions”. *Nucl. Phys. A* 698 (2002). Ed. by T. J. Hallman, D. E. Kharzeev, J. T. Mitchell, et al., 306–313. arXiv: [nucl-ex/0104021](https://arxiv.org/abs/nucl-ex/0104021).
- [39] A. Andronic, P. Braun-Munzinger, J. Stachel, et al. “Production of light nuclei, hypernuclei and their antiparticles in relativistic nuclear collisions”. *Phys. Lett. B* 697 (2011), 203–207. arXiv: [1010.2995 \[nucl-th\]](https://arxiv.org/abs/1010.2995).
- [40] L. Adamczyk et al. “Measurement of  $D^0$  Azimuthal Anisotropy at Midrapidity in Au+Au Collisions at  $\sqrt{s_{NN}}=200$  GeV”. *Phys. Rev. Lett.* 118.21 (2017), 212301. arXiv: [1701.06060 \[nucl-ex\]](https://arxiv.org/abs/1701.06060).
- [41] P. Huovinen, P. F. Kolb, Ulrich W. Heinz, et al. “Radial and elliptic flow at RHIC: Further predictions”. *Phys. Lett. B* 503 (2001), 58–64. arXiv: [hep-ph/0101136](https://arxiv.org/abs/hep-ph/0101136).
- [42] Maurice. G Kendall. *The Advanced Theory Of Statistics. Vol. 1-3, CHARLES GRIF-FIN.*
- [43] Anders Hald. “The Early History of the Cumulants and the Gram-Charlier Series”. *International Statistical Review / Revue Internationale de Statistique* 68.2 (2000), 137–153.
- [44] <https://en.wikipedia.org/wiki/Skewness>.
- [45] <https://en.wikipedia.org/wiki/Kurtosis>.

- [46] R. A. Fisher and J. Wishart. “The Derivation of the Pattern Formulae of Two-Way Partitions from those of Simpler Patterns”. *Proceedings of the London Mathematical Society* s2-33.1 (Jan. 1932), 195–208. eprint: <https://academic.oup.com/plms/article-pdf/s2-33/1/195/4369165/s2-33-1-195.pdf>.
- [47] R. V. Gavai and Sourendu Gupta. “Lattice QCD predictions for shapes of event distributions along the freezeout curve in heavy-ion collisions”. *Phys. Lett. B* 696 (2011), 459–463. arXiv: [1001.3796 \[hep-lat\]](https://arxiv.org/abs/1001.3796).
- [48] Frithjof Karsch and Krzysztof Redlich. “Probing freeze-out conditions in heavy ion collisions with moments of charge fluctuations”. *Phys. Lett. B* 695 (2011), 136–142. arXiv: [1007.2581 \[hep-ph\]](https://arxiv.org/abs/1007.2581).
- [49] Sourendu Gupta. “Finding the critical end point of QCD: Lattice and experiment”. *PoS CPOD2009* (2009). Ed. by Marcy Chaloupka, 025. arXiv: [0909.4630 \[nucl-ex\]](https://arxiv.org/abs/0909.4630).
- [50] Szabolcs Borsanyi, Zoltan Fodor, Jana N. Guenther, et al. “Higher order fluctuations and correlations of conserved charges from lattice QCD”. *JHEP* 10 (2018), 205. arXiv: [1805.04445 \[hep-lat\]](https://arxiv.org/abs/1805.04445).
- [51] B. Friman, F. Karsch, K. Redlich, et al. “Fluctuations as probe of the QCD phase transition and freeze-out in heavy ion collisions at LHC and RHIC”. *Eur. Phys. J. C* 71 (2011), 1694. arXiv: [1103.3511 \[hep-ph\]](https://arxiv.org/abs/1103.3511).
- [52] Wei-jie Fu, Xiaofeng Luo, Jan M. Pawłowski, et al. “Hyper-order baryon number fluctuations at finite temperature and density”. *Phys. Rev. D* 104.9 (2021), 094047. arXiv: [2101.06035 \[hep-ph\]](https://arxiv.org/abs/2101.06035).
- [53] Misha A. Stephanov, K. Rajagopal, and Edward V. Shuryak. “Event-by-event fluctuations in heavy ion collisions and the QCD critical point”. *Phys. Rev. D* 60 (1999), 114028. arXiv: [hep-ph/9903292](https://arxiv.org/abs/hep-ph/9903292).
- [54] Christiana Athanasiou, Krishna Rajagopal, and Misha Stephanov. “Using Higher Moments of Fluctuations and their Ratios in the Search for the QCD Critical Point”. *Phys. Rev. D* 82 (2010), 074008. arXiv: [1006.4636 \[hep-ph\]](https://arxiv.org/abs/1006.4636).
- [55] M. A. Stephanov. “Non-Gaussian fluctuations near the QCD critical point”. *Phys. Rev. Lett.* 102 (2009), 032301. arXiv: [0809.3450 \[hep-ph\]](https://arxiv.org/abs/0809.3450).

- [56] M. A. Stephanov. “On the sign of kurtosis near the QCD critical point”. *Phys. Rev. Lett.* 107 (2011), 052301. arXiv: [1104.1627 \[hep-ph\]](#).
- [57] Jaroslav Adam et al. “Beam energy dependence of (anti-)deuteron production in Au + Au collisions at the BNL Relativistic Heavy Ion Collider”. *Phys. Rev. C* 99.6 (2019), 064905. arXiv: [1903.11778 \[nucl-ex\]](#).
- [58] Jaroslav Adam et al. “Production of light nuclei and anti-nuclei in pp and Pb-Pb collisions at energies available at the CERN Large Hadron Collider”. *Phys. Rev. C* 93.2 (2016), 024917. arXiv: [1506.08951 \[nucl-ex\]](#).
- [59] L. Adamczyk et al. “Measurement of elliptic flow of light nuclei at  $\sqrt{s_{NN}} = 200, 62.4, 39, 27, 19.6, 11.5, \text{ and } 7.7$  GeV at the BNL Relativistic Heavy Ion Collider”. *Phys. Rev. C* 94.3 (2016), 034908. arXiv: [1601.07052 \[nucl-ex\]](#).
- [60] Zuzana Fecková, Jan Steinheimer, Boris Tomášik, et al. “Formation of deuterons by coalescence: Consequences for deuteron number fluctuations”. *Phys. Rev. C* 93.5 (2016), 054906. arXiv: [1603.05854 \[nucl-th\]](#).
- [61] Edward Shuryak and Juan M. Torres-Rincon. “Baryon clustering at the critical line and near the hypothetical critical point in heavy-ion collisions”. *Phys. Rev. C* 100.2 (2019), 024903. arXiv: [1805.04444 \[hep-ph\]](#).
- [62] Edward Shuryak and Juan M. Torres-Rincon. “Baryon preclustering at the freeze-out of heavy-ion collisions and light-nuclei production”. *Phys. Rev. C* 101.3 (2020), 034914. arXiv: [1910.08119 \[nucl-th\]](#).
- [63] Kai-Jia Sun, Lie-Wen Chen, Che Ming Ko, et al. “Probing QCD critical fluctuations from light nuclei production in relativistic heavy-ion collisions”. *Phys. Lett. B* 774 (2017), 103–107. arXiv: [1702.07620 \[nucl-th\]](#).
- [64] Rajiv V. Gavai. “The QCD critical point: an exciting Odyssey in the Femto-world”. *Contemp. Phys.* 57.3 (2016), 350–365.
- [65] Anton Andronic, Peter Braun-Munzinger, Krzysztof Redlich, et al. “Decoding the phase structure of QCD via particle production at high energy”. *Nature* 561.7723 (2018), 321–330. arXiv: [1710.09425 \[nucl-th\]](#).
- [66] J. Cleymans, H. Oeschler, K. Redlich, et al. “Comparison of chemical freeze-out criteria in heavy-ion collisions”. *Phys. Rev. C* 73 (2006), 034905. arXiv: [hep-ph/0511094](#).

- [67] A. Andronic, P. Braun-Munzinger, and J. Stachel. “Hadron production in central nucleus-nucleus collisions at chemical freeze-out”. *Nucl. Phys. A* 772 (2006), 167–199. arXiv: [nucl-th/0511071](#).
- [68] Francesco Becattini. “A Thermodynamical approach to hadron production in e+ e- collisions”. *Z. Phys. C* 69.3 (1996), 485–492.
- [69] F. Becattini and Ulrich W. Heinz. “Thermal hadron production in p p and p anti-p collisions”. *Z. Phys. C* 76 (1997). [Erratum: *Z.Phys.C* 76, 578 (1997)], 269–286. arXiv: [hep-ph/9702274](#).
- [70] Sabita Das, Debadepti Mishra, Sandeep Chatterjee, et al. “Freeze-out conditions in proton-proton collisions at the highest energies available at the BNL Relativistic Heavy Ion Collider and the CERN Large Hadron Collider”. *Phys. Rev. C* 95.1 (2017), 014912. arXiv: [1605.07748 \[nucl-th\]](#).
- [71] Sourendu Gupta, Debasish Mallick, Dipak Kumar Mishra, et al. “Limits of thermalization in relativistic heavy ion collisions”. *Phys. Lett. B* 829 (2022), 137021.

# Chapter 2

## The STAR Experiment

### 2.1 Relativistic Heavy Ion Collider (RHIC)

In the Brookhaven National Laboratory, New York, USA, the collider facility known as the Relativistic Heavy Ion Collider (RHIC) [1] was designed to collide heavy-ion/proton beams at ultra-relativistic energies. The purpose was to study the matter created in the early universe. RHIC is a unique and versatile collider capable of providing a variety of ion beams in a broad range of energies. The first runs started in the year 2000. Since then, RHIC has been used to collide various beam species (proton, deuteron, helium, aluminum, copper, Ruthenium, Zirconium, gold, and uranium) at a number of collision energies ( $\sqrt{s_{NN}} = 3$  up to 200 GeV). RHIC has also provided beams for polarized proton-proton collision at  $\sqrt{s} = 500$  GeV to study the spin structure of the nucleon.

An aerial view of RHIC with different components is shown in Figure 2.1. The RHIC is a ring accelerator. RHIC design includes two approximately circular rings situated underground that are rotating in opposite directions. The circumference of each ring is approximately 3.8 Km. Clockwise circulating ions (called the “blue beam”) can collide

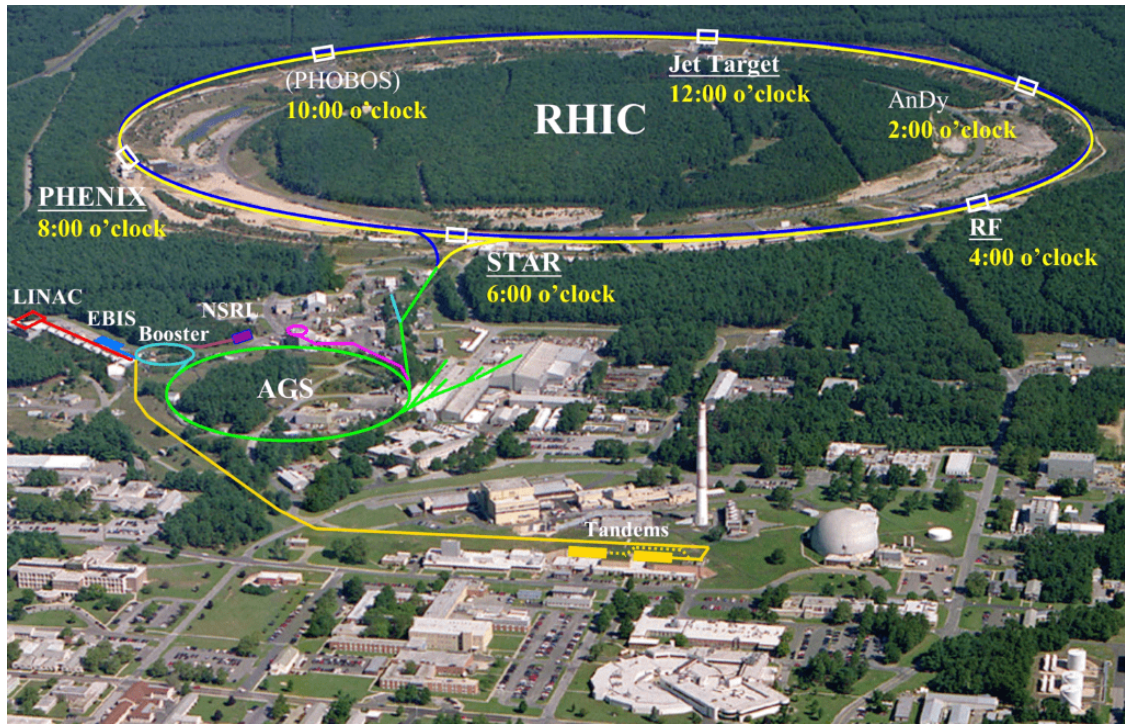


Figure 2.1: Top view of the RHIC accelerator situated at the Brookhaven National Laboratory, New York, USA [2].

with counterclockwise circulating ions (called the “yellow beam”) at 6 different fixed interaction regions.

Starting from a Tandem Van de Graaff accelerator till the Alternating Gradient Synchrotron (AGS), heavy ions are guided and accelerated to be finally injected into RHIC rings. The details of the RHIC project can be found in Ref. [3]. Ions are injected in bunches ( $\sim 10^9$  ions per beam bunch) in resonant cavities of radiofrequency electromagnetic fields. Electric fields accelerate these bunches of ions. A large array of powerful dipolar magnets [4] guide the beam around the collider ring. Independent magnet systems for the two rings allow the tuning of the beam bunches to achieve equal rotation frequencies of ions/particles. RHIC rings accelerate the beam up to desired energies and store them for collision data recording. When the beam luminosity drops below a certain level, and the

desired interaction rate is not achieved then the beams are released from the rings (beam dumping) and new beam bunches are fed into the RHIC rings.

Four main experiments that are located at these interaction points are Solenoidal Tracker At RHIC (STAR) [5], Pioneering High Energy Nuclear Interaction eXperiment (PHENIX) [6], Broad RAnge Hadron Magnetic Spectrometers (BRAHMS) [7], and PHOBOS (named after the largest natural satellite of Mars) [8]. Using the analogy of a 12-hour analog clock BRAHMS, STAR, PHENIX, and PHOBOS can be thought to be located at the 2 o'clock, 6 o'clock, 8 o'clock, and 10 o'clock positions of RHIC. Currently, the STAR experiment is operational at RHIC. Recently, the STAR experiment has successfully completed data taking of much-sought phase II of the Beam Energy Scan (BES-II) program. A makeover of the PHENIX experiment for hard probe physics (jets, quarkonia, and heavy-flavor) study is coming up with upgrades and is known as the sPHENIX detector [9]. sPHENIX will begin collecting data in the year 2023. PHOBOS and BRAHMS completed their operation in the year 2005 and 2006, respectively.

The data analysis work we present in this thesis is performed with the data recorded by the STAR detector located in RHIC. Currently, nearly 700 collaborators affiliated with 71 institutions from 14 different countries constitute the STAR experiment collaboration [10]. STAR collaboration works to record, store, maintain, and analyze collision data. STAR collaboration also develops and maintains the complicated detector system.

## 2.2 The STAR Detector

The STAR detector [5] at RHIC was built to map the QCD phase diagram by studying matter in extreme conditions such as at high energy/baryonic density and to search for the signatures of QGP. To accomplish this, STAR was designed to primarily measure charged

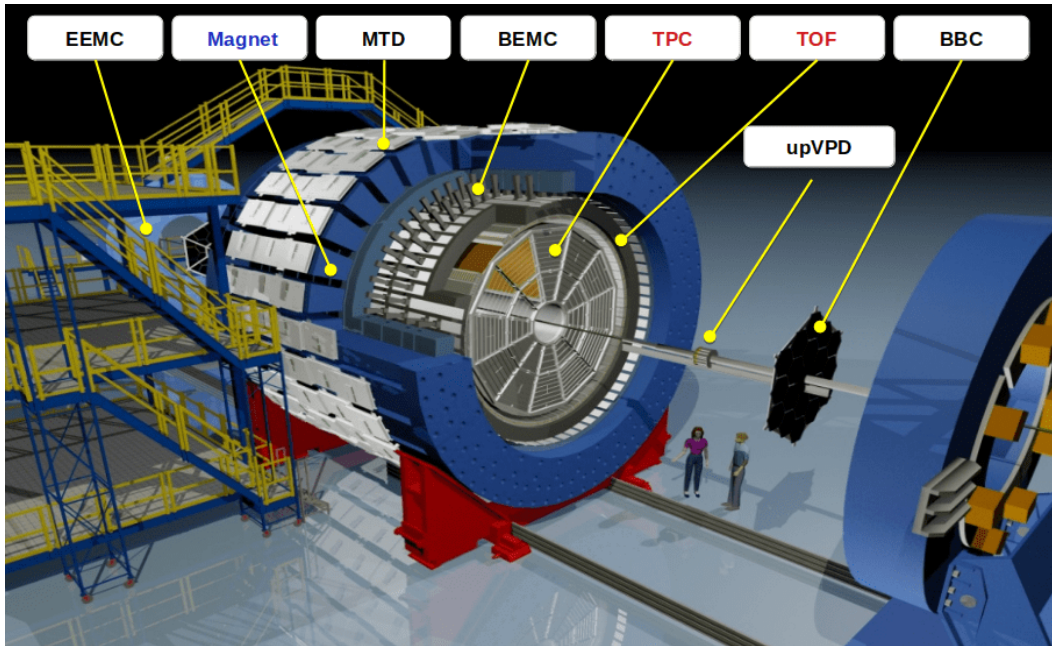


Figure 2.2: Schematic three-dimensional picture of the STAR detector layout. Primary sub-systems are outlined except the ZDC. As the VPD and the BBC detectors are placed in both east and west directions of the collision point, only one side of those are visible from this particular angle. The figure is taken from [11].

hadrons with high-precision tracking, their momenta, and the identification of different particles.

STAR is a cylindrical shaped “barrel” detector. Most of the sub-systems of the STAR detector are located in such a way to cover the mid-rapidity. A 3D schematic model of the detector, a schematic picture representing the coordinate system, and an event display can all be seen in Figures 2.2, 2.3, and 2.4, respectively.

STAR detector is very large in size and comprise of complex subsystems. Due to limitations in the text length here, we will briefly discuss only a few sub-systems of the STAR detector. The Time Projection Chamber (TPC), Time-of-Flight (TOF), and trigger detectors are the main components used in this analysis. In the following subsection, these detector systems are discussed.

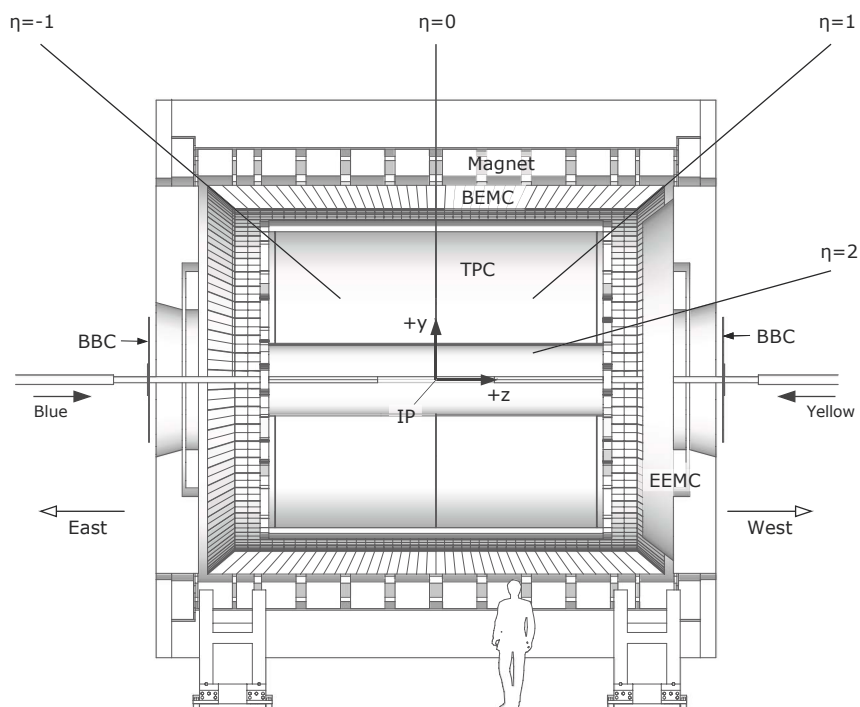


Figure 2.3: Schematic section cut of the STAR detector representing the co-ordinate system [12].

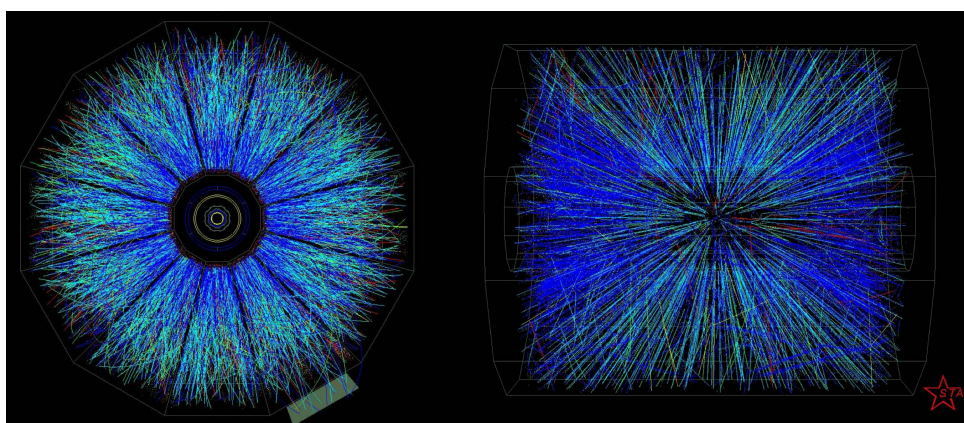


Figure 2.4: Collision event from the first gold beam-beam collisions at RHIC at  $100+100$  GeV/ $c$  per beam recorded by STAR TPC detector. Blue and green colored tracks carry opposite electric charge. The small visible gaps are due to the boundaries between different sectors of the TPC [13].

## 2.2.1 The Time Projection Chamber (TPC)

The TPC is a mid-rapidity cylindrically-symmetric detector that sits in the heart of the STAR detector covering the beam-beam interaction point [14, 15]. TPC sub-system is one of the most important detector in the STAR experiment. TPC registers hits of charged tracks, measures momenta, and identifies the particle species from ionization energy losses ( $dE/dx$ ). This covers a pseudo-rapidity region of  $|\eta| < 1.8$  and the full azimuth. It can measure the momenta of particles from 100 MeV/ $c$  to 30 GeV/ $c$  and identify particle species over a momentum range from 100 MeV/ $c$  to greater than 1 GeV/ $c$ .

### 2.2.1.1 Technical Design of TPC

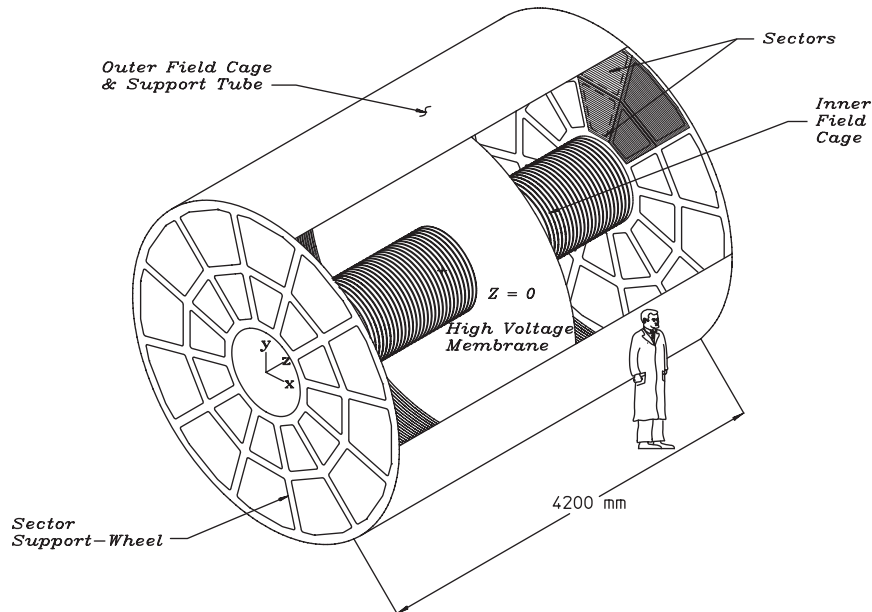


Figure 2.5: A schematic diagram (in three dimension) displaying major parts of the TPC detector [15].

Figure 2.5 shows the schematic diagram of STAR TPC. It is in the form of a cylinder

of 4.2m in length and 4m in diameter. A central membrane divides the detector into equal halves on the east and west sides. This membrane is kept at a voltage of  $\sim 28\text{kV}$  with respect to the detection planes and serves as the cathode. An uniform electric field of  $135\text{V/cm}$  is applied inside the TPC in the direction pointing away from the end caps. The readout systems are connected to the end caps which are at the ground potential. These endcaps serve as anodes. A solenoidal magnet provides a uniform magnetic field of strength  $0.5\text{T}$  along the beam direction ( $z$ -axis). The TPC is filled with P10 gas (90%  $\text{Ar}$  and 10%  $\text{CH}_4$ ). The composition of gas provides a fast drift velocity to electrons that maximizes even for a lower value of the electric field. Uniformity of the electric field is critical for the uniform electron drift and is maintained by a chain of 183 resistors and equipotential rings along the concentric field cage cylinders [15]. TPC gas is regulated at a pressure of 2 mbar above the atmospheric pressure and prevented from being contaminated with outside air.

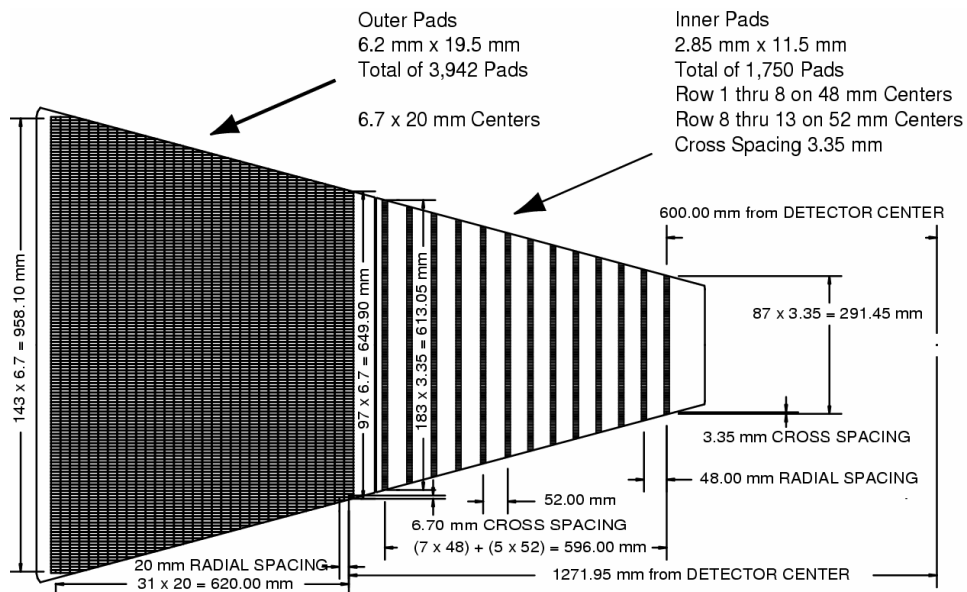


Figure 2.6: Example of one sector of anode of TPC detector showing different sub-sectors. On the left, outer subsector is shown and the on the right the inner subsector is shown [15].

The MWPC chambers contain of three wire planes and a pad plane each. Each endcap has 12 readout sectors. A sector is further divided into inner and outer subsectors. The inner sector is close to the interaction region and meets with a high density of particles. Each inner sector consists of a large number of small pads. These pads are distributed in 13 pad rows. This results in a better resolution of the track position and provides better ability to separate two tracks in case of track merging or splitting. The pads of the outer sectors are densely packed in 32 rows per sector to optimize the measurement of energy loss by ionization in a region with lower particle densities. One full sector of the anode pad plane is shown in Figure 2.6. A track in the TPC therefore can have a maximum of 45 hits if it crosses all 45 (13+32) pad rows.

### 2.2.1.2 Track Reconstruction in TPC

As a charged particle traverses in the TPC, it ionizes the atoms and molecules of the gas and leaves a cluster of electrons. Under the influence of the electric field, electrons drift towards anode (anode carry high voltages) and produce showers of charge via further ionization. Due to image charge principle, signals arise on the other side of the TPC pad row. The signal from the pads is amplified and digitized by Analog to Digital Converters (ADCs) and then given into the DAQ.

The  $x - y$  position of a ionization cluster is obtained by detecting the signal in adjacent pads (along a single pad row). The  $z$ -position can be found by measuring the drift time from the origin of a cluster to the end cap and the average drift velocity. The magnetic field bends the track into the shape of a helix. An algorithm known as Time Projection Chamber Tracker (TPCT) is employed to reconstruct the tracks by a helical function fit of the hits in TPC. Charged particle track in the magnetic field is a helix to first order. However, track shape can also deviate from a helix due to the incremental loss of energy and multiple

Coulomb scatterings. Information of track from TPC combined with those from other inner detectors (SVT, SSD) are applied to refit by making use of the Kalman Fit Method [16] to find a global track. The global tracks are extrapolated to fit back to a most probable common origin, which is the primary vertex of a collision. The typical value of primary vertex resolution is  $\sim 350 \mu\text{m}$  with more than 1000 tracks. Tracks which have distance of closest approach from the primary vertex of collision within 3 cm, are then refitted. In this case, the primary vertex position is additional fit point in space. These tracks are known as primary tracks.

Charged particle multiplicity measured by the TPC detector is utilized to define the collision centrality. Centrality is a measure to classify events according to the amount of overlap region among two colliding nuclei in a collision. Final state multiplicity is used as a proxy of initial overlap to classify events into different centralities. Good quality charged primary tracks measured by TPC in the acceptance  $|\eta| < 1.0$  are compared to those simulated using the Monte-Carlo Glauber model [17] (model used to simulate the initial geometry of two colliding nuclei) to determine the centrality. Further details on the centrality determination are discussed in Chapter 3.

### 2.2.1.3 Particle Identification Using $dE/dx$ Measurements

Identification of the charged particles can be performed using TPC from the measurement of energy loss ( $dE/dx$ ) of tracks due to interactions with the gaseous medium. Ionization process being stochastic in nature, the ionization fluctuations are large as the energy loss is measured over a short length. Therefore, the accuracy of the average  $dE/dx$  measurement is limited. Instead, we estimate the most probable  $dE/dx$ . Approximately, 30% of the biggest ionization clusters are removed from the calculation of most probable  $dE/dx$ . The truncated mean of  $dE/dx$  of the only remaining clusters is taken into calculation. This

truncated mean is assigned as the default value of  $dE/dx$  for a track. For Run-14 and later, the default  $dE/dx$  in STAR was assigned to the “most probable” value <sup>1</sup>, which is the most probable value from a maximum likelihood fit.

The Bethe-Bloch equation expresses the mean value of ionization energy loss of a charged particle per distance it travelled through detector active matter,  $\langle dE/dx \rangle$ , to its velocity [18] as:

$$\left\langle -\frac{dE}{dx} \right\rangle = Kz^2 \frac{Z}{A} \frac{1}{\beta^2} \left[ \frac{1}{2} \ln \frac{2m_e c^2 \beta^2 \gamma^2 T_{max}}{I^2} - \beta^2 - \frac{\delta(\beta\gamma)}{2} \right], \quad (2.1)$$

where  $m_e$  is the mass of the electron,  $c$  is the speed of light,  $\beta = v/c$ ,  $z$  is the charge of the incident particle.  $I$  is the average ionization energy of the material,  $T_{max}$  is the maximum kinetic energy that a free electron gets in an interaction,  $\delta$  is a correction related to the electron density, and  $\beta\gamma = p/mc$ , where  $p$  is the momentum and  $m$  is the mass of the charged particle. From the above equation we see that the  $dE/dx$  is mass dependent and there useful to identify different particles.

Hans Bichsel determined a more accurate parameterization of the energy loss referred to as “Bichsel curves” [19], an extension of the Bethe-Bloch formula [18]. In STAR the values used for the 70%- truncated mean and most probable mean that are defined above, are based on the Bichsel functions as opposed to the Bethe-Bloch functions.

Figure 2.7 shows these curves on top of the measurements from the STAR experiment. Different bands correspond to different particle species. The  $dE/dx$  resolution of a track that crosses 40 pad rows is 8% [15]. This makes  $\pi/K$  band separation possible up to  $p \sim 0.7$  GeV/ $c$  and proton band separation from  $\pi/K$  up to  $p \sim 1.1$  GeV/ $c$ . The separation of bands can be described quantitatively by a variable  $n\sigma$  defined using the measured and the

<sup>1</sup>For more information on  $dE/dx$  calculation in the STAR experiment, analyzers can refer to Yuri Fisyak’s talk <https://drupal.star.bnl.gov/STAR/system/files/bug2465.pdf>

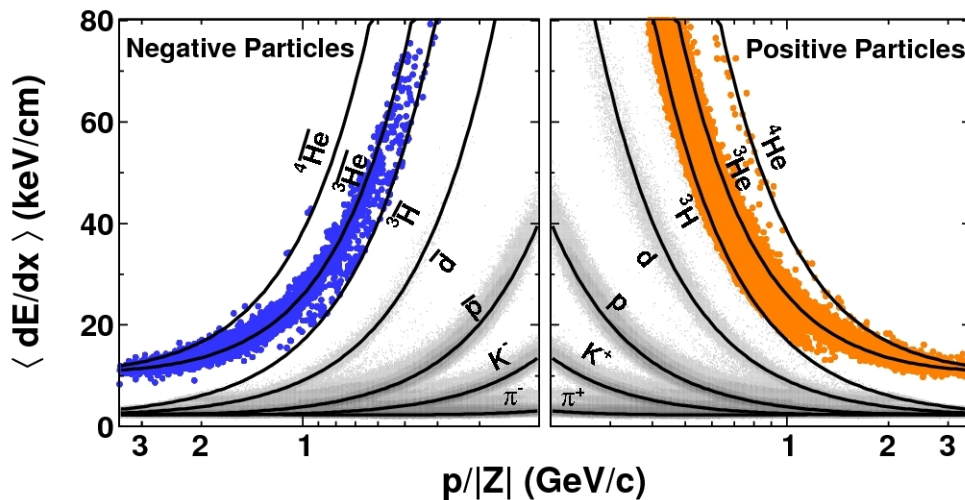


Figure 2.7: Ionization energy loss measured in the STAR TPC detector for different charged particles is shown as a function of rigidity ( $p/Z$ ) [20].

expected values of ionization energy loss. The  $n\sigma_X$  is defined as:

$$n\sigma_X = \frac{1}{R} \log \frac{\langle dE/dx \rangle|_{X, \text{measured}}}{\langle dE/dx \rangle|_{X, \text{predicted}}}, \quad (2.2)$$

where  $X$  is the particle type ( $e$ ,  $\pi$ ,  $K$  or  $p$ ),  $\langle dE/dx \rangle|_{X, \text{measured}}$  is the measured energy loss of a track,  $\langle dE/dx \rangle|_{X, \text{predicted}}$  is the theoretical value for mean energy loss for a particle species type  $X$  at any given value of  $p$ , and  $R$  is the  $dE/dx$  resolution.

Similarly, another variable  $Z_X$  is also used sometimes to identify the particles and is defined as

$$Z_X = \ln \frac{\langle dE/dx \rangle|_{X, \text{measured}}}{\langle dE/dx \rangle|_{X, \text{predicted}}} \quad (2.3)$$

This  $Z$  variable is used to identify deuterons for this analysis. Details of the identification technique using the  $Z$  variable are explained in Chapter 3.

### 2.2.2 Time of Flight (TOF) Detector

STAR Time-of-Flight (TOF) [21] system enables extending the particle identification in the experiment to higher momentum region,  $p_T$  ( $>1.0$  GeV/ $c$ ). TOF detector covers a pseudo-rapidity region of  $|\eta| < 0.9$  and the full azimuth. TOF system consists of a total of 120 trays installed at the outside barrel of the TPC (with 60 on the east side and 60 on the west side). Each tray is 2.4 m long, 21.3 cm wide, and 8.5 cm deep and covers 6 degrees in the azimuth. TOF in STAR uses Multigap Resistive Plate Chamber (MRPC) [22] technology. There are 32 MRPC modules in each tray, placed along the beam ( $z$ ) direction. An MRPC basically consists of a stack of resistive plates with a series of uniform gaps filled with Freon gas. It works in avalanche mode. Across the outermost plates a high voltage is applied. As a charged particle passes through a module, it generates avalanches in the gaseous gaps. The sum of signals from the avalanches in all these gaps is the total signal. This technology and design gives the total time of flight of a track as,  $\Delta t = t_{start} - t_{stop}$ , a resolution of approximately 80 ps, making the TOF a very fast detector.

Using the measured track path length,  $L$ , (using information from TPC and extrapolating to the TOF and the primary vertex) and the flight time,  $t$ , of a particle from the primary vertex, we can directly calculate the velocity of the particles and their mass.

$$\beta = \frac{v}{c} = \frac{L}{ct}, \quad (2.4)$$

where  $c$  is the light velocity.

Figure 2.8 shows the  $1/\beta$  of a track as a function of its rigidity (momentum/charge). The inverse velocity shows distinct bands corresponding to different masses *i.e.* for particle species. Comparing Figures 2.7 and 2.8 reveals that the TOF detector provides much better separation between different particle species than the TPC for a given momentum. Then,

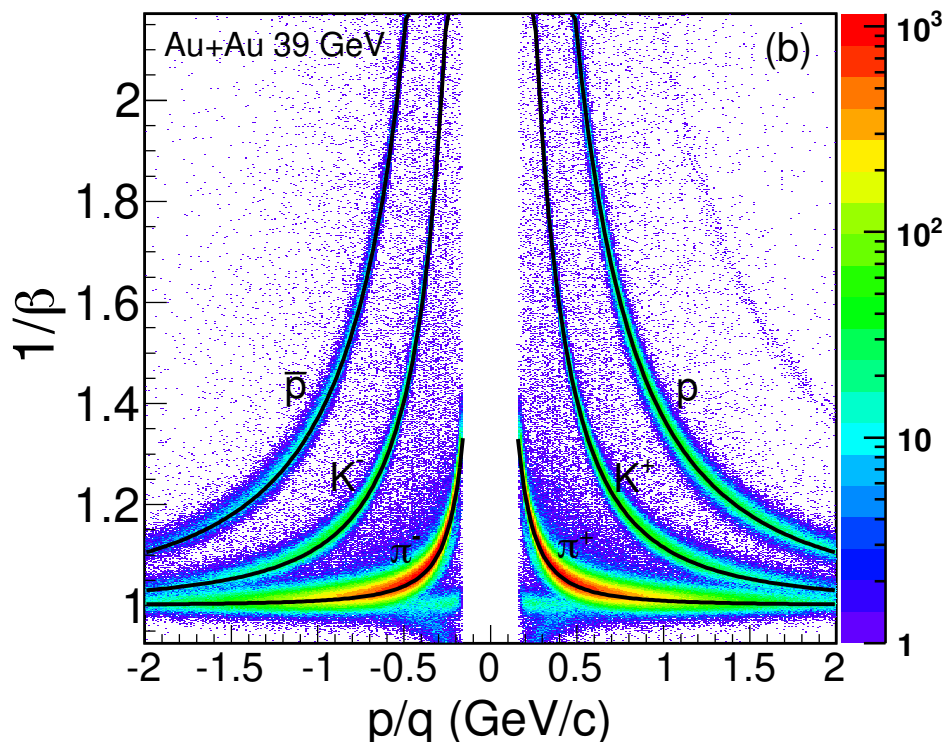


Figure 2.8:  $1/\beta$  from TOF vs. rigidity (momentum/charge) at  $\sqrt{s_{NN}} = 39$  GeV. The curves, from low to up, show the expected mean values of pions, kaons, and (anti-) protons, respectively. The figure is taken from [23].

since  $\beta = p/E$  and  $E = \sqrt{p^2 + m^2}$ , particle mass can be related to its velocity as:

$$m^2 = \left( \frac{1}{\beta^2} - 1 \right) \times p^2 = \left( \frac{c^2 t^2}{L^2} - 1 \right) \times p^2. \quad (2.5)$$

Using  $m^2$  values particles can be identified with good purity in the higher momentum region. Details of the identification of proton and deuteron using  $m^2$  are explained in Chapter 3.

Due to a relatively slower response of the TPC detector, there are possibilities that charged tracks from a previous event are added to the multiplicity of a subsequent event. These events which contain residual tracks from previous events are called pile-up events and can affect higher moment observables [24]. TOF being a fast detector, is also utilized to

remove pile-up events. By requiring an approximately linear correlation between charged particle multiplicities measured from TPC and the fast TOF detector, pile-up events are removed from the analysis. Details on this technique are discussed in Chapter 3.

### 2.2.3 Trigger Detectors

The trigger system [25–27] in STAR observes every RHIC crossing and applies certain criteria to whether or not to accept a collision event and initiate recording the data. Interaction rates at RHIC for the highest luminosity of beams can approach  $\sim 10$  MHz. The major part of the STAR data is recorded by the slow detectors, which operate at rates of  $\sim 100$  Hz. Therefore, the trigger system takes input from fast detectors to control the event selection to be recorded by the much slower tracking detectors. The Zero Degree Calorimeters (ZDC), the Beam Beam counters (BBC), the Vertex Position Detectors (VPD), and the ElectroMagnetic Calorimeters (EMC) are the primary trigger detectors at STAR.

In order to provide some universal characteristics to a collision, a detector subsystem, namely a pair of ZDCs [28] is utilized. On both the sides (east and west) of center of STAR, the ZDC detectors are situated at a distance of  $\pm 18$  m. They cover an angle of  $\theta < 2$  mrad w.r.t. to the  $z$ -axis. ZDC on each side of the collision consists of three modules. Each module in ZDC contains a series of tungsten plates alternating with layers of wavelength-shifting fibers. The fibers are then joined to a photomultiplier tube (PMT). The ZDCs are primarily hadronic calorimeters and measure deposited energy by the spectator neutrons of colliding nuclei. The real nucleus-nucleus collisions are distinguished from the background events by requiring coincidence in ZDCs along the two beam directions. Apart from being useful as an event trigger, ZDC is used as a luminosity monitor at the collision in heavy ion colliders [29]. Using the estimate of beam luminosity from ZDC, associated corrections to the multiplicity distributions are performed while defining the collision centralities.

The BBC is in a hexagonal array structure of scintillators. It is located on both east and west sides of the interaction region at a distance of 3.7m close to the beam direction. BBC tiles give full azimuth coverage in the pseudorapidity range of  $3.4 < \eta < 5.0$  [30]. The timing difference between the two counters is used to get information on the primary vertex position. Coincidence signals on both sides of the BBC are also used to reject background events.

The VPD [31, 32] system is made up of 19 lead converters together with plastic scintillators with photo-multiplier tube readout situated at 5.7 m on both sides of STAR center. It covers the pseudo-rapidity range of  $4.24 < |\eta| < 5.1$ . Similar to BBC, coincident hits in both the east and west VPDs are required to select minimum bias events. VPD can also provide  $z$ -component of the collision vertex, with a better timing resolution than BBC.

The calorimeter system in the STAR experiment consists of a full Barrel Electromagnetic Calorimeter (BEMC) [33], single Endcap Electromagnetic Calorimeter (EEMC) [34]. Electromagnetic calorimeters are used to trigger events with rare probes and high  $p_T$  processes. Such events can be associated with high electromagnetic energy deposition in the EMC towers or patches by jets, leading hadrons, direct photons, and heavy quarks. EMCs are also used to characterize ultra-peripheral collision events.

## Bibliography

- [1] *RHIC webpage*. <https://www.bnl.gov/rhic/>.
- [2] *RHIC Accelerator complex*. <https://www.bnl.gov/rhic/complex.php>.
- [3] M. Harrison, T. Ludlam, and S. Ozaki. “RHIC project overview”. *Nucl. Instrum. Meth. A* 499 (2003), 235–244.
- [4] M. Anerella et al. “The RHIC magnet system”. *Nucl. Instrum. Meth. A* 499 (2003), 280–315.

- [5] K. H. Ackermann et al. “STAR detector overview”. *Nucl. Instrum. Meth. A* 499 (2003), 624–632.
- [6] K. Adcox et al. “PHENIX detector overview”. *Nucl. Instrum. Meth. A* 499 (2003), 469–479.
- [7] M Adamczyk et al. “The BRAHMS experiment at RHIC”. *Nucl. Instrum. Meth. A* 499 (2003), 437–468.
- [8] B. B Back et al. “The PHOBOS detector at RHIC”. *Nucl. Instrum. Meth. A* 499 (2003), 603–623.
- [9] Megan Connors. “Design, status and schedule of the sPHENIX experiment at RHIC”. *Nucl. Phys. A* 967 (2017). Ed. by Ulrich Heinz, Olga Evdokimov, and Peter Jacobs, 548–551.
- [10] *STAR Experiment Webpage*. <https://www.star.bnl.gov>.
- [11] *3D picture of STAR detector by Alex Schmah (STAR Collaboration) and Maria*.
- [12] L. Adamczyk et al. “Longitudinal and transverse spin asymmetries for inclusive jet production at mid-rapidity in polarized  $p + p$  collisions at  $\sqrt{s} = 200$  GeV”. *Phys. Rev. D* 86 (2012), 032006. arXiv: [1205.2735 \[nucl-ex\]](https://arxiv.org/abs/1205.2735).
- [13] <https://www.star.bnl.gov/public/imagelib/collisions2001/>.
- [14] J. H. Thomas. “A TPC for measuring high multiplicity events at RHIC”. *Nucl. Instrum. Meth. A* 478 (2002). Ed. by M. Jeitler, M. Krammer, G. Neuhofer, et al., 166–169.
- [15] M. Anderson et al. “The Star time projection chamber: A Unique tool for studying high multiplicity events at RHIC”. *Nucl. Instrum. Meth. A* 499 (2003), 659–678. arXiv: [nuc1-ex/0301015](https://arxiv.org/abs/nuc1-ex/0301015).
- [16] D. Liko. *STAR Note 00087, 1 (1992)*.
- [17] Michael L. Miller, Klaus Reygers, Stephen J. Sanders, et al. “Glauber modeling in high energy nuclear collisions”. *Ann. Rev. Nucl. Part. Sci.* 57 (2007), 205–243. arXiv: [nuc1-ex/0701025](https://arxiv.org/abs/nuc1-ex/0701025).
- [18] W. M. Yao et al. “Review of Particle Physics”. *J. Phys. G* 33 (2006), 1–1232.
- [19] H. Bichsel. “A method to improve tracking and particle identification in TPCs and silicon detectors”. *Nucl. Instrum. Meth. A* 562 (2006), 154–197.

- [20] H. Agakishiev et al. “Observation of the antimatter helium-4 nucleus”. *Nature* 473 (2011). [Erratum: *Nature* 475, 412 (2011)], 353. arXiv: [1103.3312 \[nucl-ex\]](#).
- [21] B. Bonner, H. Chen, G. Eppley, et al. “A single Time-of-Flight tray based on multigap resistive plate chambers for the STAR experiment at RHIC”. *Nucl. Instrum. Meth. A* 508 (2003). Ed. by P. Fonte, M. Fraga, S. P. Ratti, et al., 181–184.
- [22] E. Cerron Zeballos, I. Crotty, D. Hatzifotiadou, et al. “A New type of resistive plate chamber: The Multigap RPC”. *Nucl. Instrum. Meth. A* 374 (1996), 132–136.
- [23] L. Adamczyk et al. “Bulk Properties of the Medium Produced in Relativistic Heavy-Ion Collisions from the Beam Energy Scan Program”. *Phys. Rev. C* 96.4 (2017), 044904. arXiv: [1701.07065 \[nucl-ex\]](#).
- [24] P. Garg and D. K. Mishra. “Higher moments of net-proton multiplicity distributions in a heavy-ion event pile-up scenario”. *Phys. Rev. C* 96.4 (2017), 044908. arXiv: [1705.01256 \[nucl-th\]](#).
- [25] C. Adler et al. “The STAR level-3 trigger system”. *Nucl. Instrum. Meth. A* 499 (2003), 778–791.
- [26] F. S. Bieser et al. “The STAR trigger”. *Nucl. Instrum. Meth. A* 499 (2003), 766–777.
- [27] E. G. Judd et al. “The evolution of the STAR Trigger System”. *Nucl. Instrum. Meth. A* 902 (2018), 228–237.
- [28] Clemens Adler, Alexei Denisov, Edmundo Garcia, et al. “The RHIC zero degree calorimeter”. *Nucl. Instrum. Meth. A* 470 (2001), 488–499. arXiv: [nucl-ex/0008005](#).
- [29] Anthony J. Baltz, Chellis Chasman, and Sebastian N. White. “Correlated forward - backward dissociation and neutron spectra as luminosity monitor in heavy ion colliders”. *Nucl. Instrum. Meth. A* 417 (1998), 1–8. arXiv: [nucl-ex/9801002](#).
- [30] J. Kiryluk. “Local polarimetry for proton beams with the STAR beam beam counters”. *16th International Spin Physics Symposium (SPIN 2004)*. Jan. 2005, 718–721. arXiv: [hep-ex/0501072](#).
- [31] W. J. Llope et al. “The TOFp/pVPD time-of-flight system for STAR”. *Nucl. Instrum. Meth. A* 522 (2004), 252–273. arXiv: [nucl-ex/0308022](#).

- [32] W. J. Llope et al. “The STAR Vertex Position Detector”. *Nucl. Instrum. Meth. A* 759 (2014), 23–28. arXiv: [1403.6855 \[physics.ins-det\]](#).
- [33] M. Beddo et al. “The STAR barrel electromagnetic calorimeter”. *Nucl. Instrum. Meth. A* 499 (2003), 725–739.
- [34] C. E. Allgower et al. “The STAR endcap electromagnetic calorimeter”. *Nucl. Instrum. Meth. A* 499 (2003), 740–750.

## Chapter 3

# Deuteron Cumulants and Proton-Deuteron Correlation in Au+Au Collisions at RHIC

In this chapter, we report the first measurement of cumulants of event-by-event deuteron number distribution and proton-deuteron correlations as a function of collision energy and centrality measured in Au+Au collisions using the STAR detector at RHIC. The measurement is performed at nine different collision energies which were recorded in the phase-I of the Beam Energy Scan program conducted in the STAR experiment at RHIC and helps cover a wide range of baryon chemical potential ( $\mu_B$  nearly from 20 to 420 MeV) in the QCD phase diagram. Deuterons and protons are identified using the TPC and TOF detectors to ensure good purity and efficiency. Measured cumulants and correlations are corrected for detector inefficiencies and centrality bin-width effect. Statistical and systematic uncertainties are estimated using methods discussed in this chapter. Finally, measurements are compared to statistical baselines and calculations from a thermal model in

both GCE and CE setups, a coalescence toy model, and a UrQMD+phase-space coalescence model. These systematic measurements along with different model calculations help us to understand the nature of the deuteron fluctuations in the coalescence model and different ensembles of the thermal model and ultimately shed light on their production mechanism in heavy-ion collisions.

This chapter begins with Section 3.1 with a brief introduction to light nuclei production in heavy-ion collisions. The physics motivation for the measurement of higher moments of deuteron number fluctuation and proton-deuteron correlation is discussed. Section 3.2 describes the experimental data analysis methods. This includes details of the data set, selection criteria for good events and tracks, particle identification, collision centrality determination, detector efficiency correction, and the estimation of uncertainties in the measurements. Results from the measurement, model calculations, and corresponding physics discussion are presented in Section 3.3. Finally, in Section 3.4, we summarize the analysis results presented in this chapter.

### 3.1 Introduction

Light nuclei (lighter than Lithium) in the Universe are believed to be created in primordial nucleosynthesis [1], which happened within a few minutes from the Big Bang when the Universe was cold enough for deuteron to survive. However, high energy heavy-ion collisions where the fireball created freezes out at a temperature of nearly 100 MeV, also copiously produce light nuclei [2–5]. Study of the production mechanism of light nuclei in such collisions is of immense interest in the community [6–10].

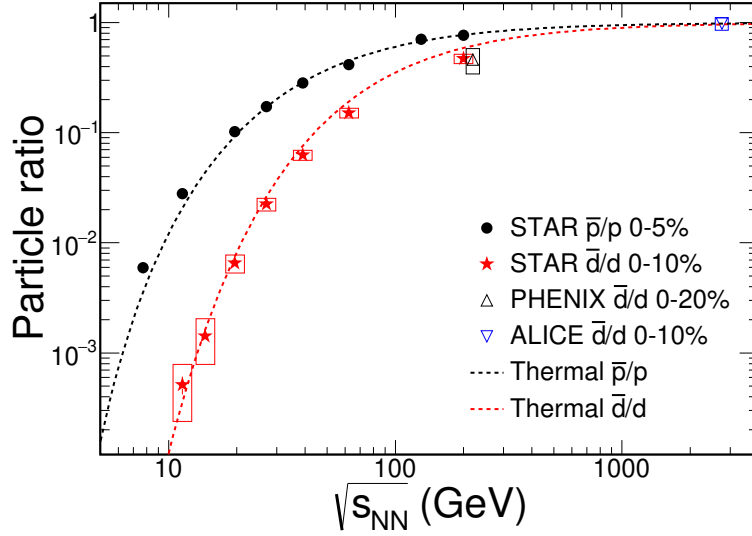


Figure 3.1: Energy dependence of anti-proton to proton ( $\bar{p}/p$ ) and anti-deuteron to deuteron ( $\bar{d}/d$ ) ratio measured in central heavy-ion collisions in different experiments. The  $\bar{d}/d$  values from STAR, PHENIX, and ALICE experiments are shown as the star, triangle, and inverted triangle markers, respectively. The curves represent thermal model calculations. Figure is taken from Ref. [4].

## Light Nuclei Production in Heavy Ion Collisions

The possible production mechanism of light nuclei includes (a) a statistical thermal model and (b) the late-stage coalescence of nucleons.

In the thermal model, degeneracy ( $g$ ), mass ( $m$ ), conserved quantum numbers ( $B$ ,  $S$ , and  $Q$ ), and thermodynamic conditions such as temperature ( $T$ ) and chemical potentials ( $\mu$ ) of conserved charges are the inputs to the calculation. In this picture, light nuclei are treated as point particles and are formed at the chemical freeze-out surface like any other hadrons. The measured yields of light nuclei can be explained by chemical freeze-out temperature obtained from the fit of hadronic yields that is at  $T \sim 156$  MeV for ALICE collision energy [11]. The anti-deuteron to deuteron yield ratio ( $\bar{d}/d$ ) measured in a range of collision energies are shown in Figure 3.1 (taken from Ref. [4]) along with thermal model calculations. Thermal model calculations are performed using a parametrization of

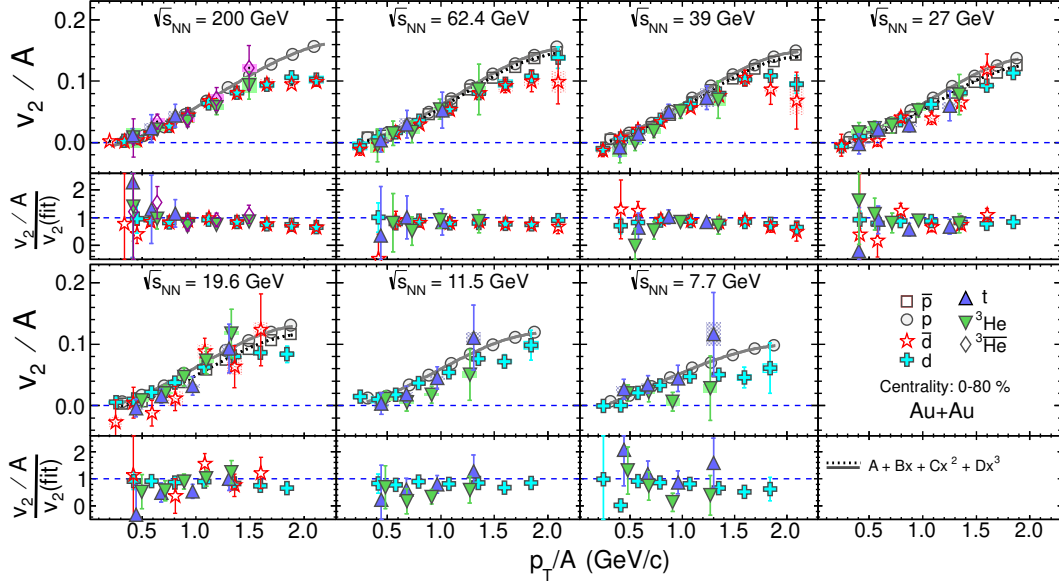


Figure 3.2: Atomic mass number ( $A$ ) scaling of the mid-rapidity  $v_2$  of  $p$ ,  $\bar{p}$ ,  $d$ ,  $\bar{d}$  and other light-nuclei from minimum bias Au + Au collisions at  $\sqrt{s_{NN}} = 7.7 - 200$  GeV. Figure is taken from Ref. [12].

$T$  and  $\mu_B$  established in [11] from the fit of hadronic yields. We observe that the thermal model fairly explains the ratio over a large range of collision energies.

In the coalescence model, nuclei are formed in the late stage of the fireball by coalescing protons and neutrons that are nearby in phase space and possess similar momenta. The invariant yield of light nuclei can be written in terms of those of proton and neutron, and a constant called, coalescence parameter  $B_A$  (where  $A$  is the mass number of the light nuclei) which shows collision energy, centrality, transverse momentum, and light-nuclei species dependence. Figure 3.2 (taken from Ref. [12]) shows the azimuthal anisotropy ( $v_2$ ) scaled to the mass number ( $A$ ) for the light-nuclei measurement in the STAR experiment.  $v_2/A$  as a function of  $p_T/A$  for all light nuclei are similar and closely follow the values for (anti-)proton for  $p_T < 3$  GeV/c, following the predictions from a nucleon coalescence picture (also supports a picture where light nuclei flow arises from parton level collectivity).

Though both the production scenarios to a satisfactory extent are able to explain the experimental data on light nuclei production and their elliptic flow, a complete understanding of the production mechanism of light nuclei is still missing.

### Fluctuations: Probe of Production Mechanism

Higher-order moments of particle distributions are known to probe finer into the thermodynamics of a system. Fluctuations of several quantities have been used extensively in heavy-ion collisions to search for the signals of QCD phase transitions and crossover as well as to extract the chemical freeze-out parameters [13–20].

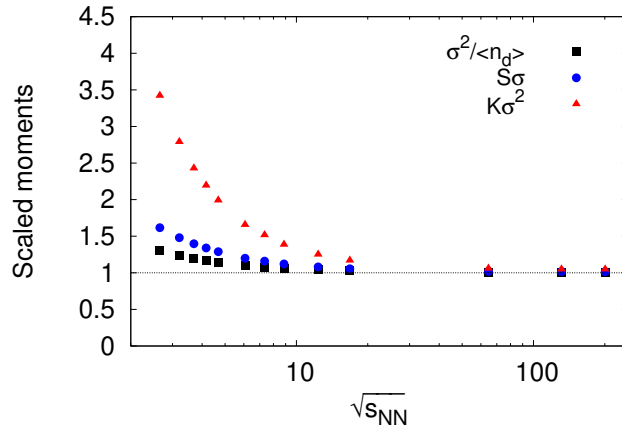


Figure 3.3: The energy dependence of the moments  $\sigma^2 / \langle n_d \rangle$ ,  $S\sigma$ , and  $\kappa\sigma^2$  of the deuteron distribution obtained from a coalescence model in Ref. [21], where  $\langle n_d \rangle$  is the mean,  $\sigma$  is the width,  $S$  is the skewness, and  $\kappa$  is the kurtosis of deuteron distribution.

Recently, it has been suggested that higher order cumulants of deuteron number fluctuations could serve as potential probes to its production mechanism [21]. Utilizing the current understanding of the fact that in low energy nuclear collisions at RHIC, at mid-rapidity, one achieves a higher number density of protons and neutrons and a larger value of the coalescence parameter  $B_2$ , the higher order cumulant ratios of deuteron number in a

coalescence picture are predicted to show large excess above the grand canonical thermal model baseline (which is at unity). These predictions are shown in Figure 3.3.

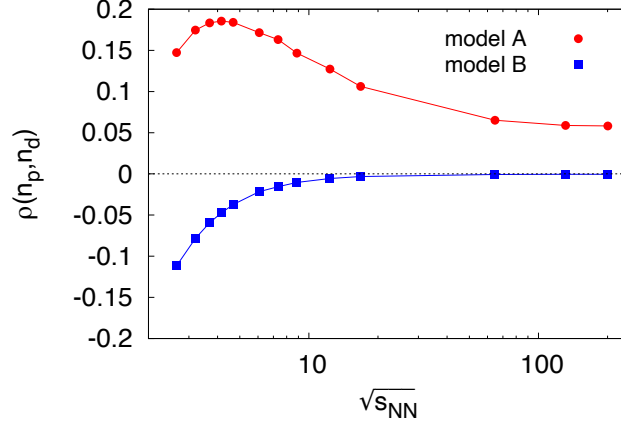


Figure 3.4: The energy dependence of the Pearson correlation coefficient ( $\rho(n_p, n_d)$ ) between proton and deuteron numbers calculated in the coalescence model for two different assumptions on proton and neutron distributions. The figure is taken from Ref. [21].

Further, under two assumptions such as fully correlated (called model A) and uncorrelated (called model B) proton and neutron number distributions, the Pearson correlation coefficient between proton and deuteron numbers gives distinct signs. In a grand canonical ensemble thermal model, one expects this correlation coefficient to be zero. Figure 3.4 shows the  $\sqrt{s_{NN}}$  dependence of the Pearson correlation coefficient of proton and deuteron numbers for these assumptions suggesting that the correlation observable might distinguish between two commonly used assumptions in the coalescence models. Note that, these predictions of the coalescence process do not take into account the phase space density of the final state nucleons and the effect of the law of global baryon number conservation [21].

In addition, higher moments of deuteron number fluctuation might be sensitive to signals of critical point and first-order phase transition. Indeed, the deuteron production

is predicted to be affected by the enhanced pre-clustering of nucleons at the chemical freeze-out due to increased strength of nucleon-nucleon interaction potential near a phase transition [22, 23]. Also, to probe neutron density fluctuations at the kinetic freeze-out induced by phase transitions, a combination of yields of the proton, deuteron, and triton is constructed [24] and has been measured by the STAR experiment that shows excess over the coalescence baseline in central Au+Au collisions at  $\sqrt{s_{NN}} = 19.6$  and 27 GeV [25]. As deuteron carries a proton and a neutron, fluctuations of deuteron will add to our current understanding of baryon number fluctuations in heavy ion collisions.

## 3.2 Data Analysis

In this section, several steps involved in the measurement of deuteron cumulants and proton-deuteron correlation using the STAR detector are presented. Starting from the good event and track selection, particle identification using TPC and TOF detectors to efficiency correction method and estimation of uncertainties will be discussed in this section.

### 3.2.1 Data set and Trigger

The data set used in this analysis consists of Au+Au collisions at nine energies:  $\sqrt{s_{NN}} = 7.7, 11.5, 14.5, 19.6, 27, 39, 54.4, 62.4, 200$  GeV. Data were taken with the STAR detector at RHIC from the year 2010 to 2017 in phase-I of the Beam Energy Scan program. Dataset corresponds to the minimum bias (MB) trigger, which requires a coincidence of two Zero-Degree Calorimeters (ZDCs) and/or Beam-Beam Counters (BBCs). It also requires the Vertex Position Detectors (VPDs) to cut on the online vertex-Z position of events. The collision energy, year of production, production tag, and trigger ids are listed in table 3.1.

Table 3.1: Collision energy, year, production tag, and triggers used.

$\sqrt{s_{NN}}$ (GeV)	Year	Production Tag	Triggers
7.7	2010	P10ih	290001, 290004
11.5	2010	P10ih	310014
14.5	2014	P14ii	440005, 440015, 440006, 440016
19.6	2011	P11id	340001, 340011, 340021
27	2011	P11id	360001
39	2010	P10ih	280001
54.4	2017	P18ic	580001, 580021
62.4	2010	P10ik	270001, 270011, 270021
200	2010	P10ik	260001, 260011, 260021, 260031

### 3.2.2 Event Selection

The primary vertex of a collision event is determined using the TPC detector sub-system and is considered to be the most common origin of the tracks emerging from the collision. For the analyzed events, it is required to have their z-coordinate of the primary vertex ( $V_z$ ) within  $\pm 30$  cm ( $\pm 40$  cm for  $\sqrt{s_{NN}} = 7.7$  GeV to achieve good event statistics) from the nominal center of the TPC along the beam line. These criteria are optimized to achieve high event statistics while keeping uniformity in the efficiency and acceptance of the detector. To remove background events (which involve beam-pipe and beam-gas interactions), transverse x-y coordinates of the primary vertex ( $V_x, V_y$ ) are required to satisfy  $V_r = \sqrt{V_x^2 + V_y^2} < 2$  cm. For  $\sqrt{s_{NN}} \geq 39$  GeV, where the beam luminosity is higher, pile-up events are removed using additional criteria on vertices determined using the VPD and TPC detectors, *i.e.*,  $|V_{pd}V_z - V_z| < 3$  cm.

#### Run-by-run QA:

Collision data sets are recorded as different runs. A “run” is a certain continuous period of data taken by the detector, while the time duration is arbitrary in nature and depends on the detector availability, beam luminosity conditions, etc. To ensure good quality of

the data throughout different run periods runs where the averaged value of track and event variables show statistically significant deviation from their global averages, are removed as bad runs. For instance, the run-by-run QA of track quantities such as  $p_T$ ,  $\eta$ , and  $\phi$  and event quantities such as  $V_x$ ,  $V_y$ , and  $V_z$  are shown for  $\sqrt{s_{NN}} = 54.4$  GeV using Figure 3.5 to Figure 3.10. Runs lying outside  $\pm 3\sigma$  are removed as bad runs. A similar QA study for several other variables is done to remove bad runs from the analysis.

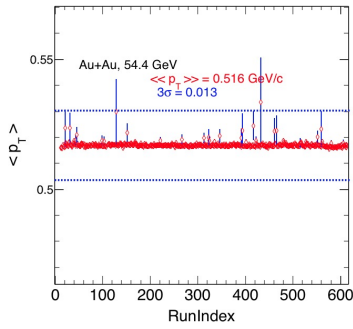
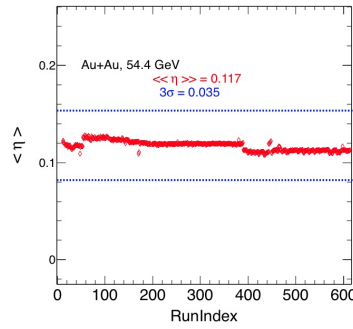
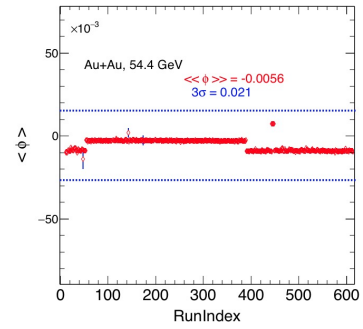
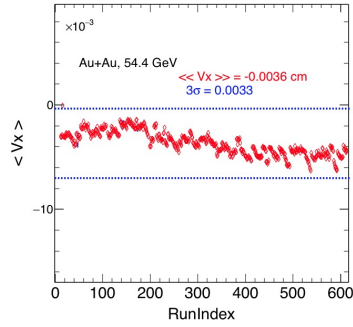
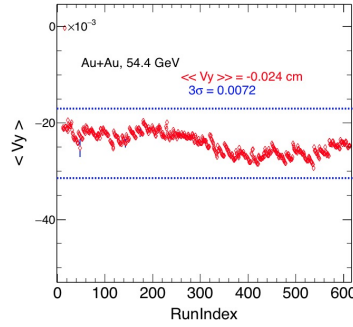
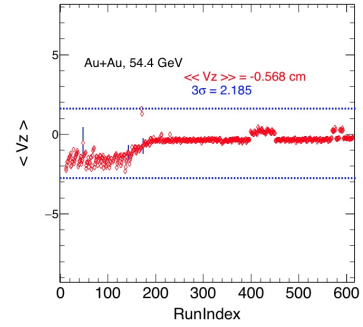
Figure 3.5: Run-wise  $\langle p_T \rangle$ Figure 3.6: Run-wise  $\langle \eta \rangle$ Figure 3.7: Run-wise  $\langle \phi \rangle$ Figure 3.8: Run-wise  $\langle V_x \rangle$ Figure 3.9: Run-wise  $\langle V_y \rangle$ Figure 3.10: Run-wise  $\langle V_z \rangle$ 

Table 3.2 summarises the collision energies, vertex cuts, and the analyzed good event statistics.

**Pile-up Events:** Due to a relatively slower response of the TPC detector, there are possibilities that charged tracks from a previous event are added to the multiplicity of a

Table 3.2: Collision energy, vertex cuts, and event statistics.

$\sqrt{s_{NN}}$ (GeV)	$ V_z $ (cm.)	$V_r$ (cm.)	$ V_z - VpdV_z $ (cm.)	Events ( $\times 10^6$ )
7.7	<40	<2	–	2.2
11.5	<30	<2	–	6.6
14.5	<30	<1	–	11.7
19.6	<30	<2	–	14.1
27	<30	<2	–	29.4
39	<30	<2	<3	82.8
54.4	<30	<2	<3	520
62.4	<30	<2	<3	37.2
200	<30	<2	<3	217

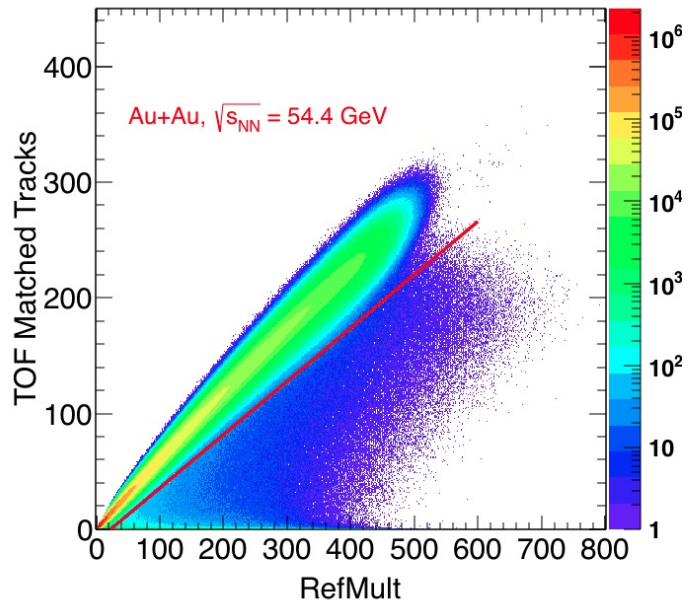


Figure 3.11: Correlation between Refmult (from TPC) and TOFmatched tracks. Events lying below the solid red line are excluded from the analysis.

subsequent event. These events which contain residual tracks from previous events are called pile-up events and can affect several physics observables. Pile-up events are further excluded by requiring an approximately linear correlation between charged particle multiplicity measured in TPC (called Refmult) and matched tracks in TOF (called TOF-

matched) detectors. For instance, at  $\sqrt{s_{NN}} = 54.4$  GeV, events which satisfy the relation:  $TOF_{matched} > 0.46 \times Ref_{mult} - 10$ , are selected for the analysis (shown using Figure 3.11). These selection criteria each  $\sqrt{s_{NN}}$  are studied and used in the previous studies in STAR [17, 18, 26].

### Signed- $DCA_{xy}$ Study:

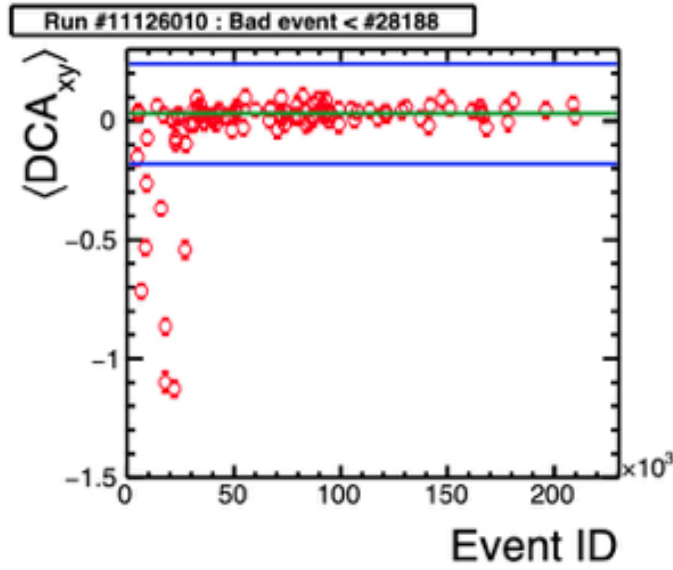


Figure 3.12: Time variation (in terms of event id) of signed  $DCA_{xy}$  in a run at  $\sqrt{s_{NN}} = 7.7$  GeV.

It was recently noted in the STAR experiment, that the cumulants of net-proton, were found sensitive to a few particular runs. A detailed study showed that tracks have strange variations on their signed  $DCA_{xy}$  values during these run periods. It is understood to be caused by the space charge build-up effect in the TPC mostly during the early part of a run that started just after a new beam is injected into the collider ring. These bad events/runs were removed from the net-proton kurtosis measurement and subsequent higher moments analyses in STAR [18, 26]. They are also removed from this analysis. An example of one such run is shown in Figure 3.12.

### 3.2.3 Track Selection and Particle Identification

In the present analysis, only primary tracks are selected for all the data sets. To select good-quality tracks various quality cuts are applied. The track quality cuts are presented in Table 3.3. All the tracks are taken within mid-rapidity  $|y| < 0.5$ .

Table 3.3: Track selection criteria for the analysis presented in this chapter.

Cut description	Values
Rapidity ( $ y $ )	$< 0.5$
Dca	$< 1$ cm
nHitsFit	$> 20$
nHitsFit/nHitsPoss	$> 0.52$
nHitsdEdx	$> 5$
$p_T$	$> 0.1$ GeV/c

Primary tracks have been selected by requiring the distance of the closest approach (DCA) from the primary vertex to be less than 1 cm. The minimum number of fit points (nHitsFit) for track reconstruction in TPC is required to be greater than 20. In addition, the minimum number of points used to measure ionization energy loss ( $dE/dx$ ) by the track is greater than 5. To minimize the split track effect, the number of points for a track reconstruction is required to be more than half of the number of total possible hit points (nHitsPoss) for a track in TPC. Each track can have a maximum of 45 hits in the TPC.

For particle identification, both TPC and TOF detectors are used in this analysis. TPC is used to measure the momentum and ionization energy loss ( $dE/dx$ ), and to reconstruct the trajectory of a charged particle. Measurements of  $dE/dx$  of charged tracks TPC are utilized to identify particles. Panel (a) of Figure 3.13 shows the measured  $\langle dE/dx \rangle$  vs. rigidity (i.e. momentum/charge) of charged tracks in  $|\eta| < 1.0$ . It can be seen that in the low momentum region, protons and deuterons can be identified very well using TPC. For

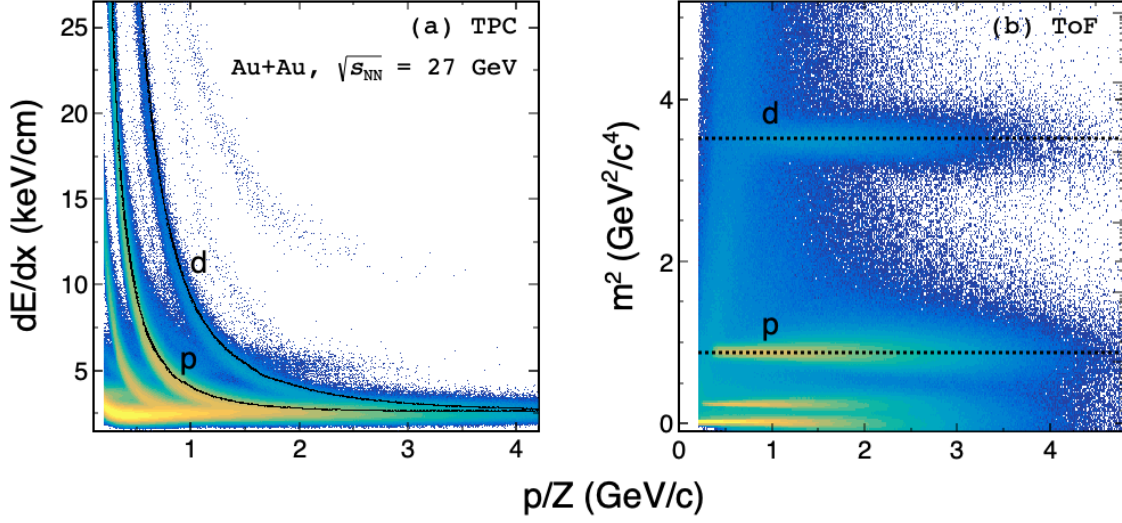


Figure 3.13:  $\langle dE/dx \rangle$  and  $m^2$  distribution of charged particles for  $|\eta| < 1.0$  in Au+Au collisions at  $\sqrt{s_{NN}} = 27$  GeV. Panel (a): The  $\langle dE/dx \rangle$  distribution of charged particles from TPC as a function of rigidity ( $p/Z$ ). The curves represent the expected values of  $\langle dE/dx \rangle$  calculated using the Bichsel function [27] for the corresponding particles. Panel (b): Mass square of charged particles as a function of momentum from TOF. The dashed lines represent the mass square values from the Particle Data Group (PDG) booklet [28] for the corresponding particles.

higher momentum regions, the TOF detector is used.

In order to identify deuterons in TPC, a variable is constructed in the STAR experiment, defined as:

$$Z_d = \ln \left[ \frac{\langle dE/dx \rangle_{\text{measured}}}{\langle dE/dx \rangle_{\text{predicted}}} \right], \quad (3.1)$$

where  $\langle dE/dx \rangle_{\text{measured}}$  is the measured mean energy loss of a track and  $\langle dE/dx \rangle_{\text{predicted}}$  is the mean energy loss predicted by Bichsel function [27] for a particle type.

TOF detector provides the information of flight time of a track from the primary vertex of the collision. With the time of flight and length of track information, mass of a particle can be written as follows.

$$m^2 = p^2 \left( \frac{c^2 t^2}{L^2} - 1 \right), \quad (3.2)$$

where  $t$ ,  $L$ , and  $c$  are the flight time of a particle, track length, and speed of light. Panel (b)

of Figure 3.13 shows the  $m^2$  values calculated using the flight time of tracks measured by the TOF detector. Clear separation of  $m^2$  bands allows the identification of particles in the higher momentum region.

For deuteron identification, TPC and TOF detectors are simultaneously utilized in the transverse momentum region of  $0.4 < p_T < 0.8$  GeV/ $c$ . Good quality tracks with  $|Z_d| < 0.2$  and  $3.0 < m^2 < 4.0$  GeV<sup>2</sup>/ $c^4$  are identified as deuterons.

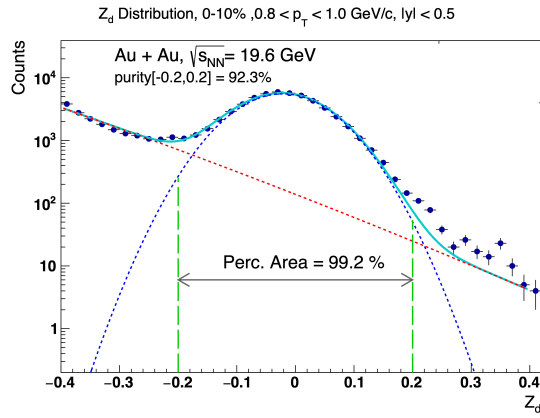


Figure 3.14:  $Z_d$  distribution from ionization energy loss in TPC in  $p_T$  range  $0.8 < p_T < 1.0$  GeV/ $c$  for central Au+Au collisions at  $\sqrt{s_{NN}} = 19.6$  GeV.

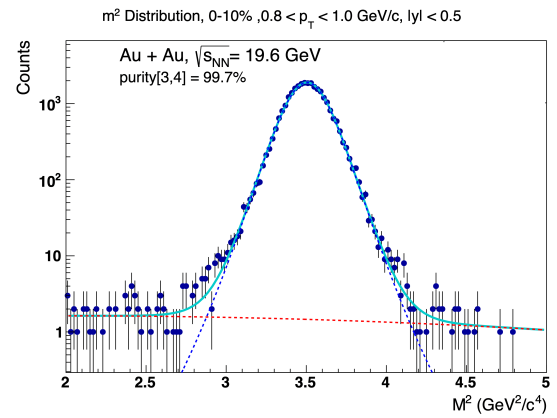


Figure 3.15:  $m^2$  distribution of deuterons from TOF detector in  $p_T$  range  $0.8 < p_T < 1.0$  GeV/ $c$  for central Au+Au collisions at  $\sqrt{s_{NN}} = 19.6$  GeV.

For instance, Figures 3.14 and 3.15 show the  $Z_d$  and  $m^2$  distributions at  $\sqrt{s_{NN}} = 19.6$  GeV. Similarly, protons are identified by a cut of  $|n\sigma_{proton}| < 2.0$  (using TPC only) for  $0.4 < p_T < 0.8$  GeV/ $c$  and by both cuts  $|n\sigma_{proton}| < 2.0$  and  $0.6 < m^2 < 1.2$  GeV<sup>2</sup>/ $c^4$  (using both TPC and TOF) for  $0.8 < p_T < 2.0$  GeV/ $c$ , where  $n\sigma$  is the measure of the deviation of measured  $dE/dx$  from Bichsel predictions in terms of  $dE/dx$  resolution  $\sigma$ . Protons and deuterons are identified in the rapidity region  $-0.5 < y < 0.5$ . By using TPC and TOF, the purity of deuterons is found above 98% for the measured  $p_T$  region. The purity of the proton sample has been studied previously in STAR and is above 97% [17].

### 3.2.4 Collision Centrality Determination

The centrality of nucleus-nucleus collisions characterizes the initial geometry of the collision. The initial system shape and size determine the initial energy density that is put into the system. The impact parameter of a heavy ion collision is not measurable in the experiments. Events are classified into different centrality classes depending on the multiplicity of produced particles. In some cases, the energy deposited by the spectators and/or produced particles is utilized to infer the initial geometry of the collisions.

In this analysis, the efficiency-uncorrected charged particle multiplicity measured by the TPC is used to define centrality. The multiplicity is selected in such a way that it consists mostly of pions and kaons. This removes the trivial self-correlation between particles used to define centrality and the particles used to calculate the cumulants. This definition of selecting charged particle multiplicity (uncorrected for track reconstruction efficiency and acceptance) is known by the name of *RefMult-3* in the STAR experiment. *RefMult-3* is selected with conditions:  $|\eta| < 1.0$ ,  $p_T > 0.1 \text{ GeV}/c$ ,  $dca < 3.0 \text{ cm}$ ,  $n\text{HitsFit} > 10$ ,  $n\sigma_{proton} < -3.0$ , and  $m^2 < 0.4 \text{ GeV}^2/c^4$ .

The multiplicity of an event should not depend on the location of the collision in the TPC. But due to variations in the acceptance of the TPC detector along the  $z$ -direction, measured multiplicity varies with  $V_z$  window. Also, the multiplicity distributions are found to vary with the luminosity of the colliding beam. Necessary corrections are performed to remove these trivial dependencies. The *RefMult-3* distribution is then compared to simulations obtained using a Monte-Carlo Glauber (MC Glauber) model [29, 30] combined with the Two-component particle production model [31]. Figure 3.16 shows the *RefMult-3* distributions for collision energies  $\sqrt{s_{NN}} = 7.7 - 200 \text{ GeV}$ .

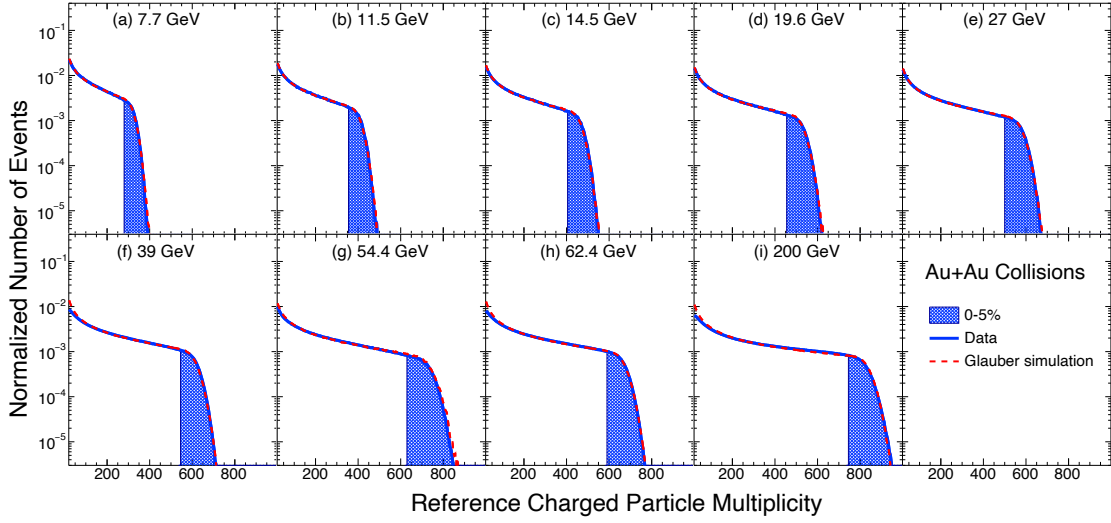


Figure 3.16: Normalised  $RefMult-3$  distributions in Au+Au collisions at  $\sqrt{s_{NN}} = 7.7 - 200$  GeV from STAR experiment. The red dashed lines show the MC Glauber + Two-component model results. The figure is taken from Ref. [18].

### 3.2.4.1 MC Glauber and Two Component Models

The Glauber model provides a quantitative picture of the geometry of the initial collision. The nucleon density profile in each collision is randomly generated using the Wood-Saxon profile [30]. The nucleon-nucleon inelastic cross-section ( $\sigma_{inel}(pp)$ ) is given as an input which is an energy-dependent quantity. The initial geometrical configuration of a collision can be characterized by the number of participant nucleons ( $N_{part}$ ), the number of binary collisions ( $N_{coll}$ ), and the impact parameter ( $b$ ). For instance, Figures 3.17 and 3.18 show the impact parameter and  $N_{part}$  distributions from the MC Glauber model for Au+Au collisions at  $\sqrt{s_{NN}} = 54.4$  GeV.

The particle production is described using the Two-component model [31]. In this model, the total energy available for particle production is approximated as  $E_{tot} \propto xE_{hard} + (1-x)E_{soft}$ , where the value of  $x$  determines the relative contributions from hard and soft processes to the particle production. Using the above approximation, the produced charged

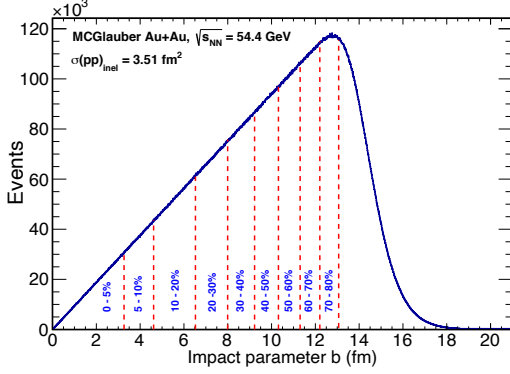


Figure 3.17: Impact parameter ( $b$ ) distribution calculated in MC Glauber model for Au+Au collisions at  $\sqrt{s_{NN}} = 54.4$  GeV.

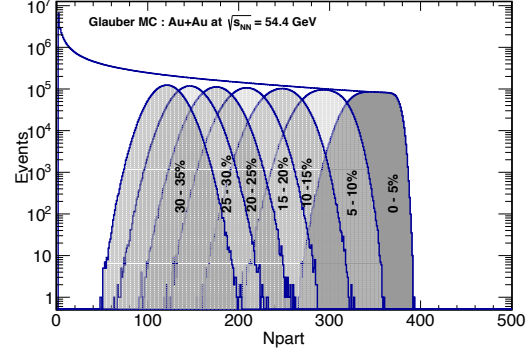


Figure 3.18: Number of participants ( $N_{part}$ ) distribution calculated in MC Glauber model for Au+Au collisions at  $\sqrt{s_{NN}} = 54.4$  GeV.

particle number is written as,

$$\frac{dN_{ch}}{d\eta} = n_{pp} \left[ x N_{coll} + (1-x) \frac{N_{part}}{2} \right], \quad (3.3)$$

where the  $n_{pp}$  is the multiplicity from  $p + p$  collisions at the same center-of-mass energy as in the heavy-ion collision of interest.

The event-by-event fluctuation in multiplicity is taken care of by convolution of the above relation with Negative-Binomial distribution where  $n_{pp}$  is sampled randomly as follows.

$$P(n_{pp}; \langle n_{pp} \rangle, k) = \frac{\Gamma(n_{pp} + k)}{\Gamma(n_{pp} + 1) \times \Gamma(k)} \times \left( \frac{\langle n_{pp} \rangle}{k} \right)^{n_{pp}} \times \left( 1 + \frac{\langle n_{pp} \rangle}{k} \right)^{-(n_{pp}+k)} \quad (3.4)$$

The simulated charged particle multiplicity from the MC Glauber model + Two-component model is compared to multiplicity from experimental data and  $\chi^2$  minimization is performed by varying the parameters  $\langle n_{pp} \rangle$ ,  $k$ , and  $x$ . Cuts on the multiplicity to classify the events into different centrality classes are obtained by finding the 0-5%, 5-10%, and so on, from the MC Glauber multiplicity distribution.

### 3.2.5 Efficiency Correction

The primary correction to the raw data is for the detector efficiency of reconstructing particle tracks. Efficiencies are determined by embedding Monte Carlo tracks simulated using the GEANT model of the STAR detector into real events at the raw data level. It is defined as the ratio of the distribution of reconstructed and simulated original Monte Carlo tracks as a function of  $p_T$ . Efficiency also has collision centrality dependence. For a given centrality, efficiencies for deuteron and proton are calculated in their respective rapidity acceptance intervals.

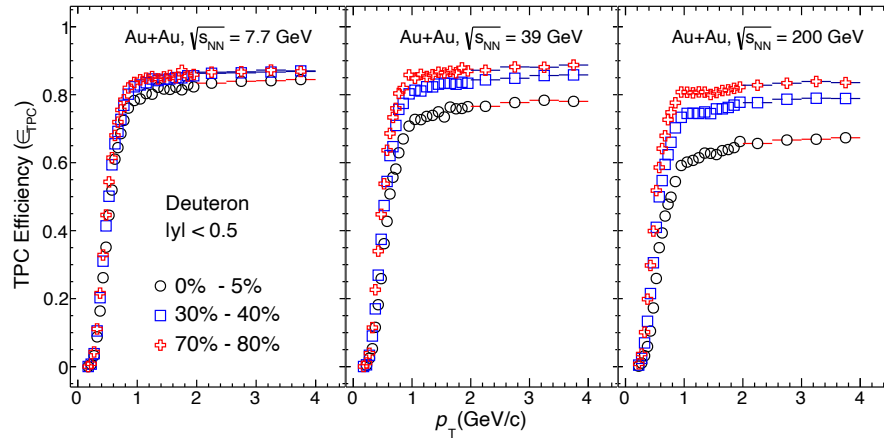


Figure 3.19: TPC efficiency of deuterons in Au+Au collisions at  $\sqrt{s_{NN}} = 7.7, 39$  and  $200$  GeV for 0-5%, 30-40% and 70-80% centrality.

Particles are identified using both TPC and TOF detectors. TOF matching efficiency correction is done with a data-driven technique. For a given particle species, TOF matching efficiency is defined as the ratio of the number of tracks detected in the TOF to the number of total tracks in the TPC within the same acceptance. Figures 3.19 and 3.20 show TPC reconstruction efficiency and TOF matching efficiency for deuterons at  $\sqrt{s_{NN}} = 7.7, 39,$  and  $200$  GeV as a function of  $p_T$ .

The calculation of  $p_T$  integrated efficiency requires the knowledge of the proper weight

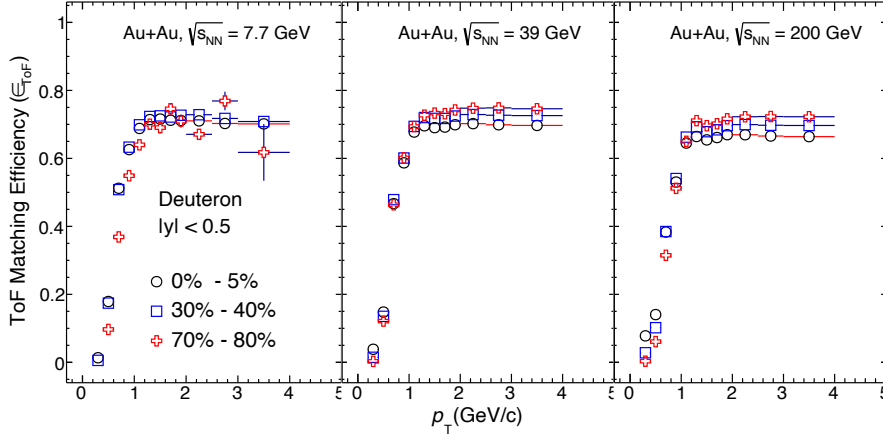


Figure 3.20: TOF matching efficiency of deuterons in Au+Au collisions at  $\sqrt{s_{NN}} = 7.7, 39$  and 200 GeV for 0-5%, 20-30% and 70-80% centrality.

factor of each  $p_T$  bin. The corrected  $p_T$  spectra for deuterons in a given centrality are used as weights to obtain the averaged efficiency as,

$$\epsilon = \frac{\int_a^b \epsilon'(p_T) f(p_T) p_T dp_T}{\int_a^b f(p_T) p_T dp_T}, \quad (3.5)$$

where the transverse momentum dependent efficiency  $\epsilon'(p_T)$  is from embedding simulation for TPC and is from the data-driven method for the TOF detector.  $f(p_T)$  is the corrected  $p_T$  spectra measured in the STAR experiment [4]. The total efficiency in a given interval of  $p_T$  becomes  $\epsilon_{TPC} \times \epsilon_{TOF}$ , where  $\epsilon_{TOF}$  is the TOF matching efficiency.

Efficiency correction of cumulants is performed by assuming a Binomial response of the detectors. Response of a particle detector can be modeled via Binomial distribution  $B_{\epsilon, N}(n)$ , where  $\epsilon$  (probability of success) is the efficiency parameter and  $N$  (number of trials) is the number of particles falling on the detector, and  $n$  (number of successes) is the number of particles measured. The probability distribution of the measured particle number can be related to the true number distribution as

$$\tilde{P}(n) = \sum_{N=n}^{\infty} P(N) B_{\epsilon, N}(n). \quad (3.6)$$

Mean and moments of fluctuations of measured particle number can be derived from a cumulant generating function [32, 33] of the probability distribution defined using 3.6. The calculations become a bit more complicated in the experiments where one needs to define the joint probability distribution of different species of particles which can come from a number of acceptance windows ( $p_T$  and/or  $y$ ). For example, in this analysis, the efficiency correction of proton-deuteron correlation involves three different efficiencies *i.e.* one for deuteron and two for protons (as they are identified in two different  $p_T$  windows).

Efficiency correction for the multi-variate case can be very computing-intensive. In Ref. [34] using a cumulant expansion method, analytic expressions for efficiency correction were derived which reduces the numerical cost. The analytic procedure is further simplified in Ref. [35]. Cumulants and mixed cumulants are obtained in terms of cumulants and moments of an observable  $q_{(r,s)}$  defined as,

$$q_{(r,s)} = \sum_{i=1}^M (a_i^r / \epsilon_i^s) n_i, \quad (3.7)$$

where,  $n_i$  is the measured number of particles in  $i^{th}$  efficiency bin and  $a_i$ ,  $\epsilon_i$  represents the quantum charge number, efficiency in the  $i^{th}$  bin, respectively.  $M$  is the total number of efficiency bins. The efficiency corrected cumulants in terms of the cumulants and mixed cumulants of the above observable are presented in Ref. [35].

### 3.2.6 Centrality Bin-Width Correction

Events are classified into different centrality bins by finding out the 0-5%, 5-10%, and so on, of the multiplicity distribution. Within one centrality class (say 0-5%), the deuteron distribution is contributed from a range of multiplicity bins. Cumulants vary over the multiplicity bins within a given centrality class. To account for the accurate mean of the number of particles, calculations of higher-order cumulants (second order and higher) are

performed in the smallest possible multiplicity bin such that in multiplicity bins of unity width and then cumulants for a centrality class (say, 0-5%) are calculated by the weighted averaging of cumulants from different multiplicity bins belonging to that centrality class. This correction also suppresses the effect of initial volume fluctuations on the measured cumulants of final state particles [36].

$$C_n = \sum_{r=1}^N \omega_r C_{n,r}, \quad (n = 2, 3, 4) \quad (3.8)$$

where

$$\omega_r = \frac{n_r}{\sum n_r}, \quad (3.9)$$

where the  $n_r$  is the number of events in  $r^{th}$  multiplicity and the corresponding weight factor is  $\omega_r = \frac{n_r}{\sum n_r}$ . The first order cumulant  $C_1$  is the mean number and remains unchanged with the above correction.

Similarly, statistical uncertainty for a cumulant in a given centrality class can be written in terms of uncertainties coming from multiplicity bins as follows.

$$\sigma^2(C_n) = \sum_{r=1}^N \omega_r^2 \sigma^2(C_{n,r}) \quad (n = 1, 2, 3, 4), \quad (3.10)$$

where  $\sigma(C_{n,r})$  is the statistical uncertainty on the cumulant  $C_n$  in the  $r$ -th multiplicity bin. All results of higher-order cumulants and Pearson correlation coefficient presented here are centrality bin-width corrected.

### 3.2.7 Statistical and Systematic Uncertainties

Experimental uncertainties on the measured cumulants come from two different kinds of sources. Limited statistics in the experiments result in statistical uncertainties while the incomplete knowledge of the experimental artifacts gives rise to systematic uncertainties.

Details of both kinds of uncertainty estimation on cumulants are discussed in the text that follows.

### 3.2.7.1 Statistical Uncertainties

As higher-order cumulant measurements are statistics hungry, proper estimation of the statistical uncertainties is very important. We performed a detailed study of the different methods for statistical uncertainty estimation and the effects of limited statistics on higher-order cumulants measurement and it led to a publication [37]. It is found that the standard method for uncertainty propagation (called Delta Theorem Method) and Bootstrap method (a Monte Carlo re-sampling technique) are both efficient methods for uncertainty estimation on higher order cumulants and predict similar values [33, 37].

For the measurements presented in this chapter, we estimate the statistical uncertainties using the Bootstrap method. In the Bootstrap method, random selection of the entries (with replacement) from the original sample is done to construct Bootstrap samples (each Bootstrap sample has the same number of entries as the original sample) over which the variance of an estimator is calculated [38]. Suppose there is a statistic  $t$  calculated from a sample ( $S$ ). Let the estimator of the statistic  $t$  be denoted by  $\hat{e}$ . We want to estimate uncertainty on the measured value of  $t$ . In the bootstrap method, the steps involved are as follows:

- Given a parent sample ( $S$ ) consisting of  $n$  number of entries, construct  $B$  number of independent bootstrap samples  $X_1^*, X_2^*, X_3^*, \dots, X_B^*$ , each consisting of  $n$  entries that are randomly drawn from the parent sample  $S$  with replacement.
- Evaluate the estimator of the statistic in each of the bootstrap samples,

$$\hat{e}_b^* = \hat{e}(X_b^*) \quad b = 1, 2, 3, \dots, B. \quad (3.11)$$

- The sampling variance of the estimator is given as follows.

$$Var(\hat{e}) = \frac{1}{B-1} \sum_{b=1}^B \left( \bar{e} - \hat{e}_b^* \right)^2, \quad (3.12)$$

where  $\bar{e}^* = \frac{1}{B} \sum_{b=1}^B (\hat{e}_b^*)$ .

The sufficient value of  $B$  for an accurate estimation of uncertainty varies from case to case depending upon the initial sample size and order of cumulants. However, in general, the larger value of  $B$  estimates the uncertainty better. Detailed discussion on the different uncertainty methods is presented in Ref. [37].

### 3.2.7.2 Systematic Uncertainties

Sources of systematic uncertainties can be broadly classified into three categories such as those arising from (a) quality criteria for good primary track selection, (b) particle identification, and (c) uncertainty in the estimation of detection efficiency. In this analysis, by varying the distance of the closest approach of tracks to the primary vertex, the number of fit points used for track reconstruction, TPC and TOF selection criteria for particle identification, and the efficiency, we estimate the systematic uncertainties. The variations (with default values mentioned using blue color) considered are summarised below.

- Dca < 0.8 cm, 0.9 cm, 1.0 cm, 1.1 cm and 1.2 cm
- nHitsFit > 15, 18, 20, 22, 25
- $|Z_d| < 0.16, 0.18, 0.20, 0.22, 0.24$
- For deuteron:  $m^2$  (GeV<sup>2</sup>/c<sup>4</sup>) between (2.9, 3.9), (2.95, 3.95), (3.0, 4.0), (3.05, 4.05), (3.1, 4.1)
- $|n\sigma_{proton}| < 1.6, 1.8, 2.0, 2.2, 2.4$

- For proton:  $m^2$  ( $\text{GeV}^2/c^4$ ) between (0.5, 1.1), (0.55, 1.15), (0.6, 1.2), (0.65, 1.25), (0.7, 1.3)
- Efficiency: +5% of default, default, -5% of default

As can be seen, each of the sources like DCA, nHitsFit,  $|n\sigma|$ ,  $mass^2$ , efficiency has several variations. First, we calculate the average contribution from each source. Let's suppose we took  $n_{var}$  number of variations of a source (for example, for DCA, we took 4 variations for the systematics), then the contribution to systematic uncertainty can be found as Equation 3.13.

$$\sigma_{source} = \sqrt{\frac{1}{n_{var}} \sum_{i=1}^{n_{var}} (Y_{var,i} - Y_{Default})^2} \quad (3.13)$$

Contributions from each of these sources are considered to be independent of each other. Systematic uncertainty can be written as

$$\sigma_{sys} = \sqrt{\sigma_{DCA}^2 + \sigma_{nHitsFit}^2 + \sigma_{|Z_d|}^2 + \sigma_{mass^2}^2 + \sigma_{eff}^2} \quad (3.14)$$

The typical values of percentage relative systematic uncertainties ( $\sigma(Y)_{sys}/Y(default)$ ), for example, in 0-5% central collisions at  $\sqrt{s_{NN}} = 7.7$  GeV are below 2% for  $C_2/C_1$  and  $C_3/C_2$  and is of the order of 7% for  $C_4/C_2$  and Pearson co-efficient. Those values are below 2% for  $C_2/C_1$ ,  $C_3/C_2$ , and  $C_4/C_2$  and is around 6% for Pearson co-efficient at  $\sqrt{s_{NN}} = 200$  GeV.

## 3.3 Results and Discussion

### 3.3.1 Event-by-Event Deuteron Distributions

Deuteron distributions for 0-5% and 70-80% centrality at  $\sqrt{s_{NN}} = 7.7, 39,$  and 200 GeV are shown in Figure 3.21. The deuteron number in an event is the multiplicity of the deuteron

selected in the acceptance of our measurement *i.e.* within  $0.8 < p_T < 4.0$  GeV/ $c$  and  $|y| < 0.5$ . These numbers are not corrected for detection efficiency. The distributions are normalized with the number of events in a given centrality.

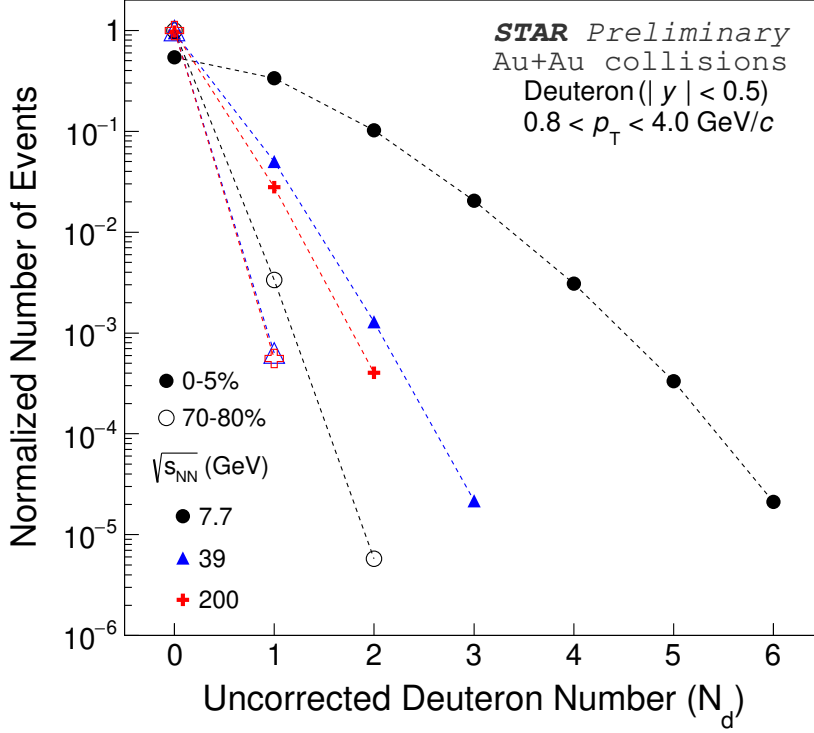


Figure 3.21: Event-by-event deuteron number distributions for 0-5% central and 70-80% Au+Au collisions for three collision energies,  $\sqrt{s_{NN}} = 7.7, 39,$  and  $200$  GeV measured by STAR. The distributions are normalized to the total number of events at each  $\sqrt{s_{NN}}$ . The statistical uncertainties are smaller than the marker symbols. Lines connecting the data points are shown to guide the eye. The deuteron numbers in this figure are not corrected for detection efficiency.

The mean and width of the distributions increase from higher to lower collision energies. This can be understood as the effect of the high number density of nucleons caused by increased baryon stopping in mid-rapidity towards lower collision energies. The larger width of a distribution contributes to larger statistical uncertainties on mean and higher-order moments. At higher  $\sqrt{s_{NN}}$  and in peripheral collisions deuterons are produced in small numbers.

### 3.3.2 Deuteron Cumulants

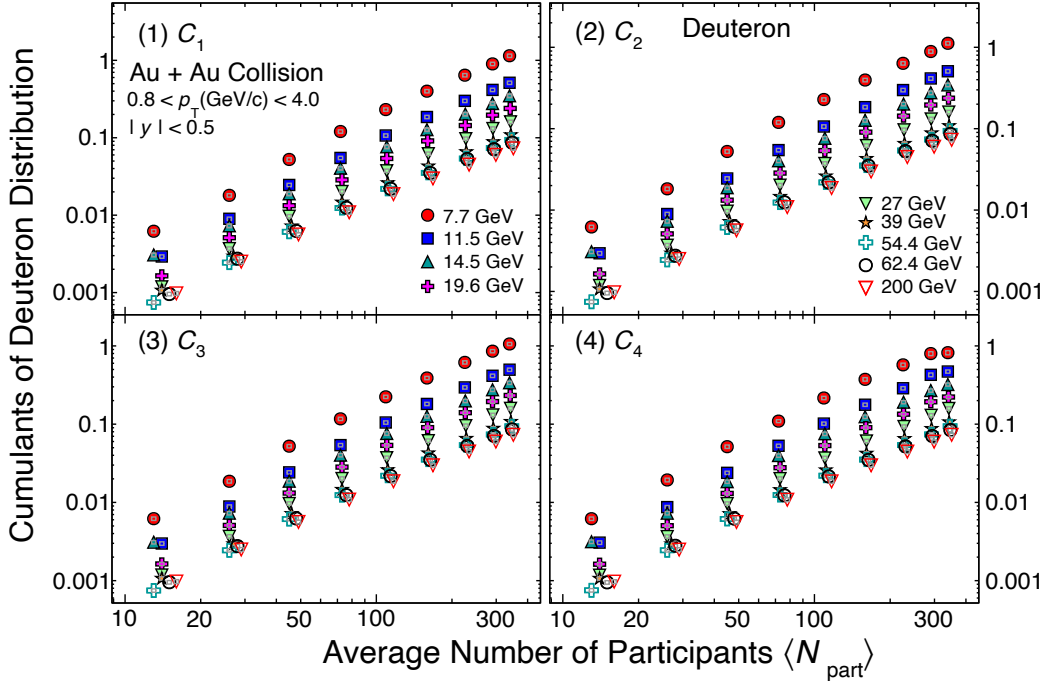


Figure 3.22: Cumulants ( $C_n$ ,  $n = 1 - 4$ ) of deuteron distributions in Au+Au collisions from  $\sqrt{s_{NN}} = 7.7 - 200$  GeV as a function of the average number of participant nucleons. Statistical and systematic uncertainties are shown.

Cumulants  $C_1$  to  $C_4$  of deuteron are calculated for different centralities and are shown in Figure 3.22. Cumulants are centrality bin-width corrected [36] to suppress the effect of initial volume fluctuation. The cumulants are also corrected for finite efficiencies for track reconstruction in the TPC and track matching efficiencies in TOF detectors. The correction is performed using the assumption of the binomial response of both the detectors for deuteron (and proton) efficiencies [35].

The statistical uncertainties on the measurements are calculated using the Monte Carlo approach called Bootstrap method [33, 37]. The systematic uncertainties at each collision energy are estimated by varying different track selections and particle identification criteria. The statistical and systematic (caps) uncertainties are presented separately in the figures.

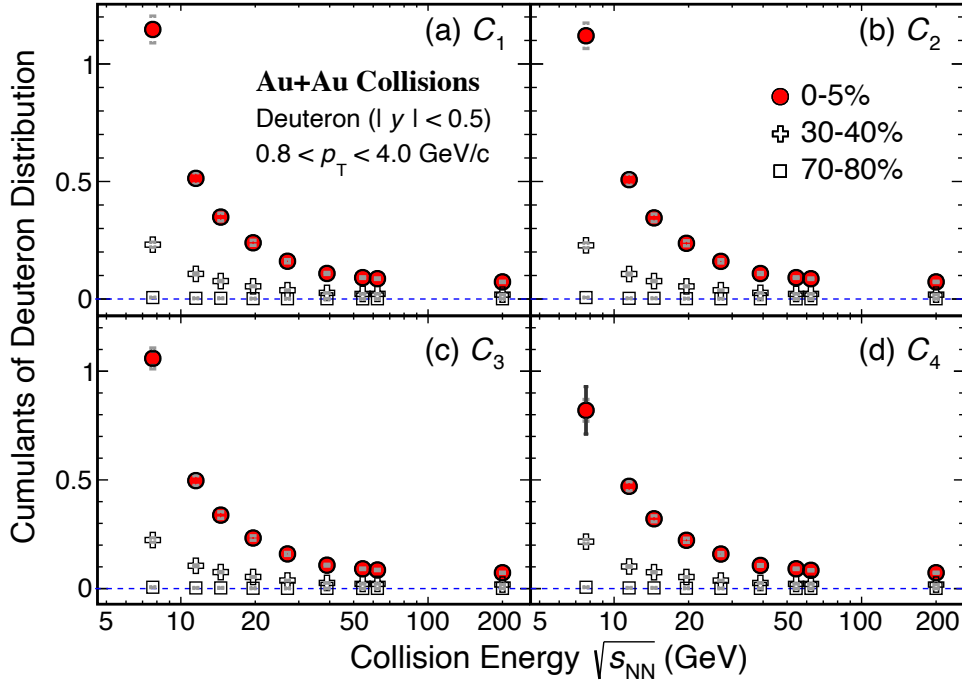


Figure 3.23: Cumulants ( $C_n$ ,  $n = 1 - 4$ ) of the deuteron distributions as a function of collision energy for central (0-5%), mid-central (30-40%), and peripheral (70-80%) Au+Au collisions were measured by STAR. Results for central, mid-central, and peripheral collisions are shown using solid circle, open cross, and open square markers, respectively. Bar and cap symbols represent the statistical and systematic uncertainties, respectively. The transverse momentum ( $p_T$ ) range for the measurements is from 0.8 to 4 GeV/c and the rapidity ( $y$ ) range is  $-0.5 < y < 0.5$ .

Results at each  $\sqrt{s_{NN}}$  are presented for nine different collision centralities *i.e.* 0-5%, 5-10%, 10-20%, 20-30%, 30-40%, 40-50%, 50-60%, 60-70%, and 70-80%. Events belonging to the 0-5% centrality class are known as the most central collision events. Similarly, events corresponding to the 70-80% centrality class are known as most peripheral collision events. The values of the average number of participants ( $\langle N_{part} \rangle$ ) obtained from the MC Glauber model represent the centralities of collision. Cumulants show a collision centrality dependence. At any given  $\sqrt{s_{NN}}$ ,  $C_1$  to  $C_4$  increase with  $\langle N_{part} \rangle$ . The larger the number of participant nucleons, the higher the energy/baryon density deposition in the initial volume of the system. Higher energy/baryon density enhances the mean yield of deuterons and

higher-order moments of their fluctuations in the final state.

Figure 3.23 shows the collision energy dependence of deuteron cumulants ( $C_n$ ,  $n = 1-4$ ) for central (0-5%), mid-central (30-40%), and peripheral (70-80%) Au+Au collisions. The statistical (shown using bars) and systematic (shown using caps) uncertainties are presented separately in the figures.

The cumulants  $C_1$  to  $C_4$  of deuteron distributions for central Au+Au collisions smoothly increase with decreasing  $\sqrt{s_{NN}}$ . One of the ways to understand the enhanced production of deuterons in the high baryon density region is by using the arguments of a thermal model. In the thermal model, baryon density dependence is given by the factor  $\sim \exp[(B\mu_B - m_d)/T]$ , where  $T$  and  $\mu_B$  are temperature and baryon chemical potential at the chemical freeze-out and  $B$  and  $m_d$  are the baryon number and mass of deuteron, respectively. As light nuclei carry multiple baryons, the contribution of the above factor is enhanced in the high baryon density region. In mid-central collisions, cumulants show a relatively weaker dependence on the collision energy. A similar energy dependence trend is also observed in 70-80% peripheral collisions. Cumulant values in peripheral collisions however are very small in magnitude.

### 3.3.3 Model Calculations

#### 3.3.3.1 Deuterons in the Thermal Model

The thermal model calculations are performed for grand-canonical and canonical ensembles using Thermal-FIST package [39]. The chemical freeze-out parameters  $T$ ,  $\mu_B$ ,  $\mu_S$ , and the volume  $V$  used in this calculation are taken from the fit of hadronic yields as published by the STAR experiment [40].  $\mu_Q$  is calculated using a parametrization from Ref. [41]. Deuterons are considered free and point particles and are produced from thermal equilibrium. The canonical ensemble set-up of Thermal-FIST uses a parameter known as

canonical correlation volume ( $V_c$ ) over which the exact conservation of the baryon number is imposed.

Figure 3.24 shows an illustration with canonical correlation volume and measurement volume in the picture. In the limit,  $V_c \rightarrow \infty$ , the nature of fluctuations in the measurement volume approach the pure grand-canonical nature. As the collision energy decreases, naturally the  $V_c$  decreases while the measurement acceptance window at most times remains the same for all  $\sqrt{s_{NN}}$ . This leads to an increased effect of conservation in low-energy measurements.  $V_c$  is varied at each collision energy for a reasonable agreement of model

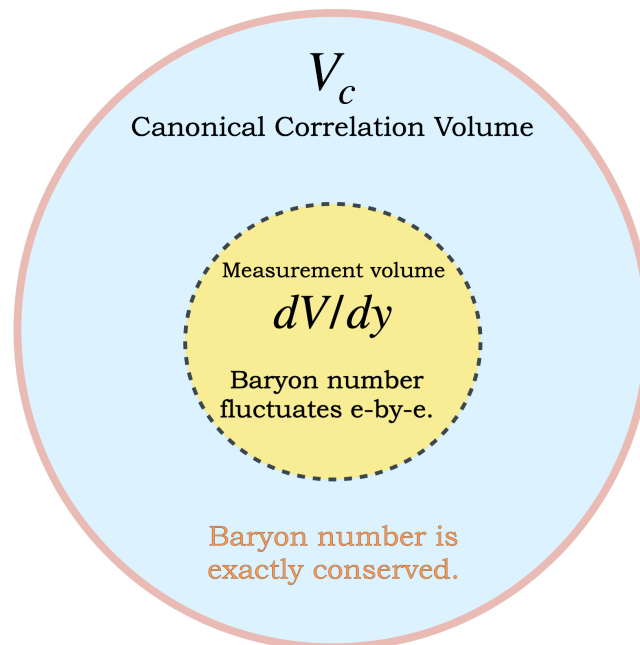


Figure 3.24: Illustration of canonical correlation volume in the canonical ensemble of a thermal model.

predictions with the measured values of deuteron cumulant ratios and Pearson coefficient. Thermal-FIST uses a blast-wave model for generating hadron momentum spectra. Deuteron cumulants and proton-deuteron correlation are calculated in the model in the same acceptance window as for the experimental measurements.

### 3.3.3.2 Deuterons in UrQMD + Phase-space Coalescence Model

The Ultra-relativistic Quantum Molecular Dynamics (UrQMD) model [42] is a microscopic transport model. UrQMD model calculations serve as suitable baselines for various final state measurements at RHIC collision energies. The model includes processes such as transportation of various degrees of freedom (e.g. baryons and mesons), interactions among them, and the production of new particles. There is no quark-hadron phase transition implemented in this model. The model takes into account effects like the decay of resonances, baryon number conservation, and baryon stopping at low energies.

Position and momentum information of protons and neutrons at the kinetic freeze-out surface of the UrQMD model is used as input to a phase-space coalescence model [43]. In the coalescence model, the relative distance ( $\Delta R$ ) and momentum ( $\Delta P$ ) between a pair of one proton and one neutron are calculated. Values of  $\Delta R$  and  $\Delta P$  have been obtained in previous phenomenological studies [43] for a reasonable agreement with experimental data. If a proton and a neutron are close enough ( $\Delta R < 3.575$  fm and  $\Delta P < 0.285$  GeV/c) to each other, a deuteron is formed and the nucleon pair is removed from the remaining list of nucleons to avoid over-counting. For each proton-neutron pair, the relative distance is calculated at the same proper time of their evolution.

### 3.3.4 Cumulant Ratios and Pearson Coefficient

As we observed in Figure 3.23 in Subsection 3.3.2, cumulants depend on the volume of the created system. In statistical physics, cumulants of the number of particles can therefore be called extensive quantities. By taking the ratio of different orders of cumulants, the trivial dependence on the system volume up to the leading order can be canceled. This also allows a direct comparison of experimental measurements to theoretical calculations.

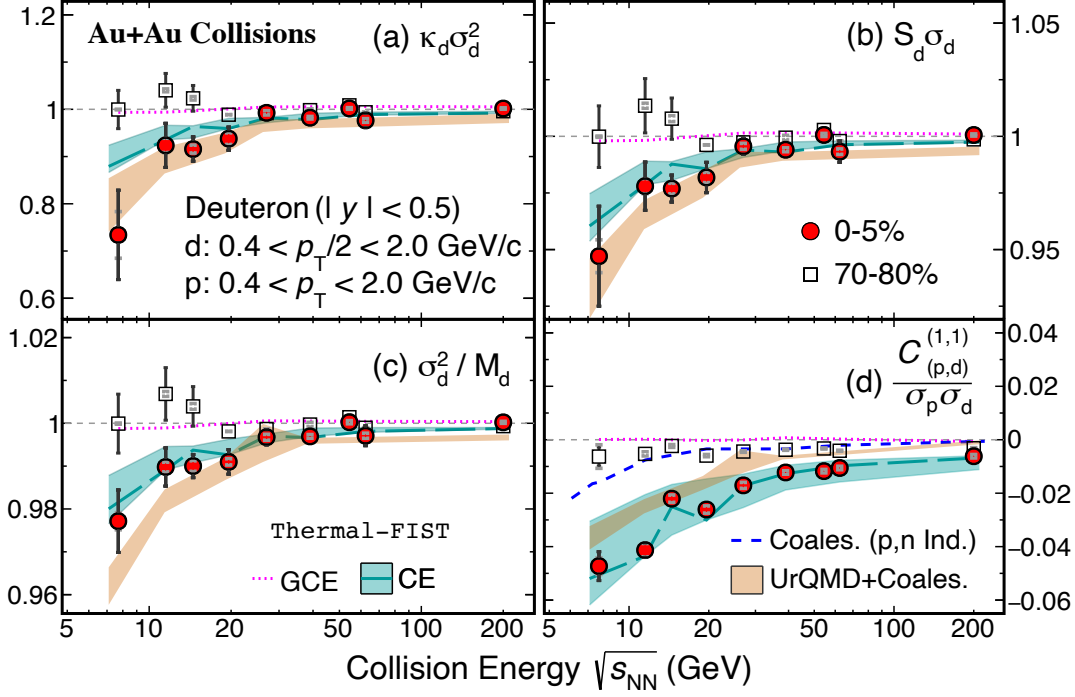


Figure 3.25: Cumulant ratios of deuteron distributions and proton-deuteron Pearson co-efficient shown as a function of  $\sqrt{s_{NN}}$ . Red solid circle and open square markers represent measurements for most central (0-5%) and peripheral (70-80%) collisions, respectively. Bar and cap symbols show the statistical and systematic uncertainties, respectively. Poisson baselines (unity for cumulant ratios and zero for Pearson coefficient) are shown by the gray dashed line. UrQMD+phase-space coalescence calculations are shown using the orange color-filled band. Thermal-FIST model calculations for GCE are shown using a magenta dashed line. The cyan color-filled band represents the CE thermal model results corresponding to the range of canonical correlation volume ( $V_c$ ) from  $2dV/dy$  to  $4dV/dy$ . CE thermal model results for  $\chi^2$  minimum fit of above four observables is shown using cyan color dashed line. In panel (d), results for one of the assumptions (independent proton and neutron distributions) in the toy model simulation of a coalescence process from Ref. [21] are shown using a blue dashed line.

Figure 3.25 shows collision energy dependence of the cumulant ratios  $\kappa\sigma^2$  ( $= C_4/C_2$ ),  $S\sigma$  ( $= C_3/C_2$ ),  $\sigma^2/M$  ( $= C_2/C_1$ ), and Pearson correlation coefficient ( $C_{(p,d)}^{(1,1)}/\sigma_p\sigma_d$ ) for central 0-5% and peripheral 70-80% Au+Au collisions.  $\kappa\sigma^2$ ,  $S\sigma$ , and  $\sigma^2/M$  in central collisions show smooth dependence on collision energy. At higher  $\sqrt{s_{NN}}$ , central 0-5% cumulant ratios are close to the Poisson baseline (unity) and deviate from unity as  $\sqrt{s_{NN}}$

decreases. The  $\kappa\sigma^2$  shows the largest deviation from unity compared to the other two ratios which involve lower-order cumulants. This suppression might arise because of global baryon number conservation. In low-energy central collisions, increased stopping of baryons and the acceptance cuts which include a larger fraction of the phase space enhance the effect of conservation. Cumulant ratios for 70-80% peripheral collision are mostly close to unity across all  $\sqrt{s_{\text{NN}}}$ .

The thermal calculations in grand-canonical and canonical ensembles are also shown in Figure 3.25. These are obtained from Thermal-FIST [39] model for the central 0-5% collisions. Grand canonical ensemble results are shown using magenta-colored dashed lines. The cyan color-filled bands correspond to the results for canonical ensemble with  $V_c$  in the ranges of 2 to 4 times the  $dV/dy$ , where  $dV/dy$  is the freeze-out volume per unit rapidity and is taken from the GCE thermal model fit of hadronic yields [40]. The cyan-colored dashed corresponds to  $\chi^2$  minimum fit results obtained from a scan of the parameter  $V_c$ . The volume parameter  $V_c$  varies between  $2dV/dy$  at the lowest energy to  $4dV/dy$  at the topmost RHIC collision energy. A slightly higher range of  $V_c$  seems to work at LHC energies for measurements from the ALICE collaboration [44, 45]. The higher value of  $V_c$  implies the part of the system under measurement is approaching the grand-canonical limit [44].

At higher collision energies, the cumulant ratios in central 0-5% show a reasonable agreement with both the thermal ensembles. However, GCE fails to describe the ratios for  $\sqrt{s_{\text{NN}}} \leq 20$  GeV. The CE thermal model with baryon number conservation implemented predicts the suppression of cumulant ratios. This suggests the importance of the canonical ensemble thermal model to understand the fluctuations in low-energy collisions. The corresponding results for 0-5% most central Au+Au collisions from a UrQMD model simulation, which incorporates law of baryon number conservation combined with a phase-space co-

alescence mechanism [43], reproduce the energy dependence trend as seen in data. With current experimental uncertainties on the cumulant ratios, both the UrQMD+Coalescence and CE thermal models seem to fairly describe the data.

In panel (d) of Figure 3.25, the Pearson correlation coefficient between proton and deuteron numbers is presented. We observe an anti-correlation across all collision energies and centralities presented. With lowering  $\sqrt{s_{NN}}$ , anti-correlation becomes stronger for central 0-5% Au+Au collisions. These measurements for peripheral Au+Au collisions do not show any energy dependence and are close to the statistical expectations. GCE thermal model fails to predict the observed anti-correlation between proton and deuteron. However, the CE thermal model calculation correctly predicts the sign and energy dependence trend of the correlation. Predictions from the simple statistical simulation of the coalescence process from Ref. [21] are also shown for central Au+Au collisions. Two different assumptions about the proton and neutron number are taken in this model such as, in one case, they are fully correlated (*i.e.*  $N_p = N_n$ , where  $N_p$  and  $N_n$  are proton and neutron multiplicities for a given event, respectively) and in the other case, they are completely independent. Neither correlated nor independent assumptions for proton and neutron numbers in the model reproduce the data. The fully correlated assumption in the model fails to predict even the sign of the correlation and we do not present those results here. On the other hand, the fair agreement of UrQMD+coalescence model predictions with the experimental data in central 0-5% collisions suggests that the phase-space density information of constituent nucleons is important for the deuteron formation process in the coalescence mechanism. ALICE collaboration recently reported measurements of proton-deuteron correlation for Pb+Pb collisions at  $\sqrt{s_{NN}} = 5.02$  TeV. The Pearson correlation coefficient was found to have small negative values and is mostly constant for all collision centralities [46]. Similar to the observations of this study, the CE thermal model calculations with baryon

number conservation implemented also explain the ALICE data for suitable choices of model parameters. The negative sign of the Pearson correlation coefficient across a range of collision energies (GeV to TeV) and centralities (central to peripheral) suggests the importance of baryon number conservation in baryon-nuclei correlations. The quality of agreement of the proton-deuteron correlation data with the CE thermal model calculation favors the canonical thermal effects over a coalescence mechanism. At the same time, there are reasonable scopes for improvement in the models presented here.

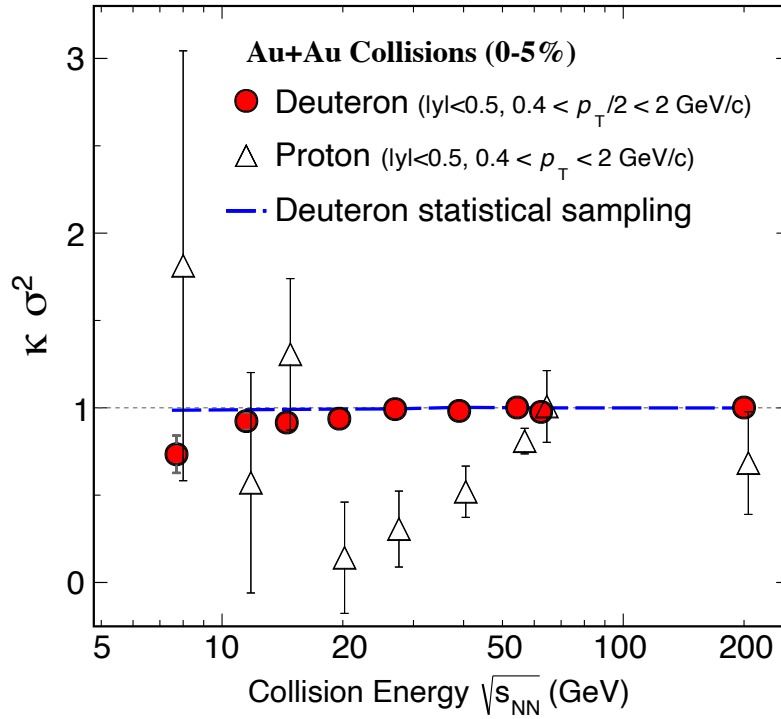


Figure 3.26:  $\kappa\sigma^2$  of deuteron and proton distribution for most central (0-5%) Au+Au collisions. Red circle and black triangle markers represent deuteron and proton data [18], respectively. The gray dashed line is the Poisson baseline (unity).  $\kappa\sigma^2$  of deuterons show smooth dependence on the collision energies in contrast to protons.

As deuterons carry two baryons, we compared deuteron cumulant ratios to that of already published measurements for protons from the STAR experiment [18]. Figure 3.26

shows the comparison of  $\kappa\sigma^2$  of deuteron multiplicity distribution to that of protons for central 0-5% Au+Au collisions. STAR experiment has shown that the net-proton  $\kappa\sigma^2$  in central collisions shows non-monotonic  $\sqrt{s_{\text{NN}}}$  dependence. This feature is similar to the theoretical predictions for the qualitative nature of net-proton cumulants near a QCD critical point [17]. The  $\kappa\sigma^2$  of the deuteron, even though deuteron carries proton and neutron, however, shows a weaker dependence on collision energy compared to that for protons. This could be due to deuterons having a very low event-by-event yield compared to protons, resulting in reduced sensitivity to any possible critical point physics. To test this possibility, we did a simple statistical toy simulation using the measured deuteron to proton yield ratios [4] and proton cumulants [18]. Using a two-component function, which is a superposition of Poisson and binomial distribution (originally developed in Ref. [47] for a different purpose), we modeled a proton distribution to reproduce the proton cumulants in central 0-5% Au+Au collisions. Then deuteron numbers are sampled on an event-by-event basis from the proton distribution using  $d/p$  ratio [4] as the binomial probability of success to form a deuteron. The values of  $\kappa\sigma^2$  calculated from this resultant deuteron distribution (shown using a blue dashed line) are near unity and close to the experimental data. This test suggests that event-by-event low yield of deuterons makes the  $\kappa\sigma^2$  come close to unity.

### 3.4 Summary

In this chapter, we have presented measurements of deuteron cumulants, their ratios, and proton-deuteron number correlation performed in Au+Au collisions with the STAR detector at RHIC, covering a wide range of baryon chemical potential ( $\mu_B$  from  $\sim 20$  to 420 MeV). The cumulant ratios in central collisions vary smoothly as a function of the collision energy and show suppression below the Poisson baseline as the colliding energy decreases. The

peripheral collision results remain overall constant with  $\sqrt{s_{NN}}$ . Anti-correlation between proton and deuteron numbers is observed across all collision energy and centrality studied. The anti-correlation becomes stronger for central Au+Au collisions as  $\sqrt{s_{NN}}$  decreases.

Important observations of our study can be summarized as follows. In central Au+Au collisions, for (A) thermal models: (i) GCE and CE models can reasonably describe the deuteron number fluctuation measurements for  $\sqrt{s_{NN}} > 20$  GeV. Only the CE thermal model correctly predicts the negative sign of the proton-deuteron correlation. (ii) CE thermal model results qualitatively agree with the data for collision energies  $\sqrt{s_{NN}} \leq 20$  GeV, while the GCE thermal model fails. Proton-deuteron correlations show better agreement with the CE thermal model results as compared to the coalescence mechanism. As the canonical ensemble explicitly conserves baryon number, our study suggests the importance of the role of baryon number conservation for fluctuation studies in low energy collisions and for (B) coalescence model: Coalescence-based model (UrQMD + phase-space coalescence) also qualitatively describe the deuteron number fluctuation and deuteron-proton correlation measurements across all collision energies. A simple toy model simulation of the coalescence process that does not take into account the baryon number conservation and phase-space information of constituent nucleons fails to describe the measured proton-deuteron number correlation.

The  $\kappa\sigma^2$  (kurtosis  $\times$  variance) of the deuteron number varies smoothly with collision energy. Proton  $\kappa\sigma^2$  shows a non-monotonic behavior with  $\sqrt{s_{NN}}$ , a qualitatively similar feature predicted by theory calculations near a critical point. Deuteron, even though carries two baryons, does not show such behavior with current experimental uncertainties. A simple statistical test suggests that the event-by-event low yields cause the multiplicity distribution of deuteron to approach the Poisson nature. Then the higher order cumulant ratio such as  $\kappa\sigma^2$  of deuteron becomes close to unity. Our measurements of cumulant

ratios of deuteron and proton-deuteron correlations will provide important inputs for future investigations of the production mechanism and freeze-out thermodynamics of light nuclei and other hadrons.

## Bibliography

- [1] R. A. Alpher, H. Bethe, and G. Gamow. “The origin of chemical elements”. *Phys. Rev.* 73 (1948), 803–804.
- [2] Jaroslav Adam et al. “Production of light nuclei and anti-nuclei in pp and Pb-Pb collisions at energies available at the CERN Large Hadron Collider”. *Phys. Rev. C* 93.2 (2016), 024917. arXiv: [1506.08951 \[nucl-ex\]](#).
- [3] T. Anticic et al. “Production of deuterium, tritium, and He3 in central Pb + Pb collisions at 20A,30A,40A,80A , and 158A GeV at the CERN Super Proton Synchrotron”. *Phys. Rev. C* 94.4 (2016), 044906. arXiv: [1606.04234 \[nucl-ex\]](#).
- [4] Jaroslav Adam et al. “Beam energy dependence of (anti-)deuteron production in Au + Au collisions at the BNL Relativistic Heavy Ion Collider”. *Phys. Rev. C* 99.6 (2019), 064905. arXiv: [1903.11778 \[nucl-ex\]](#).
- [5] J. Adamczewski-Musch et al. “Directed, Elliptic, and Higher Order Flow Harmonics of Protons, Deuterons, and Tritons in Au + Au Collisions at  $\sqrt{s_{NN}} = 2.4$  GeV”. *Phys. Rev. Lett.* 125 (2020), 262301. arXiv: [2005.12217 \[nucl-ex\]](#).
- [6] S. Mrowczynski. “Deuteron formation mechanism”. *J. Phys. G* 13.9 (1987), 1089–1097.
- [7] Rudiger Scheibl and Ulrich W. Heinz. “Coalescence and flow in ultrarelativistic heavy ion collisions”. *Phys. Rev. C* 59 (1999), 1585–1602. arXiv: [nucl-th/9809092](#).
- [8] A. Andronic, P. Braun-Munzinger, J. Stachel, et al. “Production of light nuclei, hypernuclei and their antiparticles in relativistic nuclear collisions”. *Phys. Lett. B* 697 (2011), 203–207. arXiv: [1010.2995 \[nucl-th\]](#).
- [9] Stanislaw Mrowczynski. “Production of light nuclei in the thermal and coalescence models”. *Acta Phys. Polon. B* 48 (2017), 707. arXiv: [1607.02267 \[nucl-th\]](#).

- [10] Sandeep Chatterjee and Bedangadas Mohanty. “Production of Light Nuclei in Heavy Ion Collisions Within Multiple Freezeout Scenario”. *Phys. Rev. C* 90.3 (2014), 034908. arXiv: [1405.2632 \[nucl-th\]](#).
- [11] A. Andronic, P. Braun-Munzinger, K. Redlich, et al. “Hadron yields, the chemical freeze-out and the QCD phase diagram”. *J. Phys. Conf. Ser.* 779.1 (2017). Ed. by Huan Zhong Huang, Richard Seto, Jochen Thäder, et al., 012012. arXiv: [1611.01347 \[nucl-th\]](#).
- [12] L. Adamczyk et al. “Measurement of elliptic flow of light nuclei at  $\sqrt{s_{NN}} = 200, 62.4, 39, 27, 19.6, 11.5, \text{ and } 7.7$  GeV at the BNL Relativistic Heavy Ion Collider”. *Phys. Rev. C* 94.3 (2016), 034908. arXiv: [1601.07052 \[nucl-ex\]](#).
- [13] Misha A. Stephanov, K. Rajagopal, and Edward V. Shuryak. “Event-by-event fluctuations in heavy ion collisions and the QCD critical point”. *Phys. Rev. D* 60 (1999), 114028. arXiv: [hep-ph/9903292](#).
- [14] Frithjof Karsch and Krzysztof Redlich. “Probing freeze-out conditions in heavy ion collisions with moments of charge fluctuations”. *Phys. Lett. B* 695 (2011), 136–142. arXiv: [1007.2581 \[hep-ph\]](#).
- [15] S. Borsanyi, Z. Fodor, S. D. Katz, et al. “Freeze-out parameters from electric charge and baryon number fluctuations: is there consistency?” *Phys. Rev. Lett.* 113 (2014), 052301. arXiv: [1403.4576 \[hep-lat\]](#).
- [16] Paolo Alba, Wanda Alberico, Rene Bellwied, et al. “Freeze-out conditions from net-proton and net-charge fluctuations at RHIC”. *Phys. Lett. B* 738 (2014), 305–310. arXiv: [1403.4903 \[hep-ph\]](#).
- [17] J. Adam et al. “Nonmonotonic Energy Dependence of Net-Proton Number Fluctuations”. *Phys. Rev. Lett.* 126.9 (2021), 092301. arXiv: [2001.02852 \[nucl-ex\]](#).
- [18] Mohamed Abdallah et al. “Cumulants and correlation functions of net-proton, proton, and antiproton multiplicity distributions in Au+Au collisions at energies available at the BNL Relativistic Heavy Ion Collider”. *Phys. Rev. C* 104.2 (2021), 024902. arXiv: [2101.12413 \[nucl-ex\]](#).
- [19] Sourendu Gupta, Debasish Mallick, Dipak Kumar Mishra, et al. “Limits of thermalization in relativistic heavy ion collisions”. *Phys. Lett. B* 829 (2022), 137021.

- [20] A. Pandav, D. Mallick, and B. Mohanty. “Search for the QCD critical point in high energy nuclear collisions”. *Prog. Part. Nucl. Phys.* 125 (2022), 103960. arXiv: [2203.07817 \[nucl-ex\]](#).
- [21] Zuzana Fecková, Jan Steinheimer, Boris Tomášik, et al. “Formation of deuterons by coalescence: Consequences for deuteron number fluctuations”. *Phys. Rev. C* 93.5 (2016), 054906. arXiv: [1603.05854 \[nucl-th\]](#).
- [22] Edward Shuryak and Juan M. Torres-Rincon. “Baryon clustering at the critical line and near the hypothetical critical point in heavy-ion collisions”. *Phys. Rev. C* 100.2 (2019), 024903. arXiv: [1805.04444 \[hep-ph\]](#).
- [23] Edward Shuryak and Juan M. Torres-Rincon. “Baryon preclustering at the freeze-out of heavy-ion collisions and light-nuclei production”. *Phys. Rev. C* 101.3 (2020), 034914. arXiv: [1910.08119 \[nucl-th\]](#).
- [24] Kai-Jia Sun, Lie-Wen Chen, Che Ming Ko, et al. “Probing QCD critical fluctuations from light nuclei production in relativistic heavy-ion collisions”. *Phys. Lett. B* 774 (2017), 103–107. arXiv: [1702.07620 \[nucl-th\]](#).
- [25] “Beam Energy Dependence of Triton Production and Yield Ratio ( $N_t \times N_p/N_d^2$ ) in Au+Au Collisions at RHIC” (Sept. 2022). arXiv: [2209.08058 \[nucl-ex\]](#).
- [26] *STAR Analysis Note of Net-proton  $C_4$  paper, PSN0731*. [https://drupal.star.bnl.gov/STAR/system/files/AnalysisNote\\_ver12.pdf](https://drupal.star.bnl.gov/STAR/system/files/AnalysisNote_ver12.pdf).
- [27] H. Bichsel. “A method to improve tracking and particle identification in TPCs and silicon detectors”. *Nucl. Instrum. Meth. A* 562 (2006), 154–197.
- [28] P. A. Zyla et al. “Review of Particle Physics”. *PTEP* 2020.8 (2020), 083C01.
- [29] Michael L. Miller, Klaus Reygers, Stephen J. Sanders, et al. “Glauber modeling in high energy nuclear collisions”. *Ann. Rev. Nucl. Part. Sci.* 57 (2007), 205–243. arXiv: [nucl-ex/0701025](#).
- [30] C. Loizides, J. Nagle, and P. Steinberg. “Improved version of the PHOBOS Glauber Monte Carlo”. *SoftwareX* 1-2 (2015), 13–18. arXiv: [1408.2549 \[nucl-ex\]](#).
- [31] Dmitri Kharzeev and Marzia Nardi. “Hadron production in nuclear collisions at RHIC and high density QCD”. *Phys. Lett. B* 507 (2001), 121–128. arXiv: [nucl-th/0012025](#).

- [32] Adam Bzdak and Volker Koch. “Acceptance corrections to net baryon and net charge cumulants”. *Phys. Rev. C* 86 (2012), 044904. arXiv: [1206.4286 \[nucl-th\]](#).
- [33] Xiaofeng Luo. “Unified description of efficiency correction and error estimation for moments of conserved quantities in heavy-ion collisions”. *Phys. Rev. C* 91.3 (2015). [Erratum: *Phys.Rev.C* 94, 059901 (2016)], 034907. arXiv: [1410.3914 \[physics.data-an\]](#).
- [34] Masakiyo Kitazawa. “Efficient formulas for efficiency correction of cumulants”. *Phys. Rev. C* 93.4 (2016), 044911. arXiv: [1602.01234 \[nucl-th\]](#).
- [35] Toshihiro Nonaka, Masakiyo Kitazawa, and ShinIchi Esumi. “More efficient formulas for efficiency correction of cumulants and effect of using averaged efficiency”. *Phys. Rev. C* 95.6 (2017). [Erratum: *Phys.Rev.C* 103, 029901 (2021)], 064912. arXiv: [1702.07106 \[physics.data-an\]](#).
- [36] Xiaofeng Luo, Ji Xu, Bedangadas Mohanty, et al. “Volume fluctuation and auto-correlation effects in the moment analysis of net-proton multiplicity distributions in heavy-ion collisions”. *J. Phys. G* 40 (2013), 105104. arXiv: [1302.2332 \[nucl-ex\]](#).
- [37] Ashish Pandav, Debasish Mallick, and Bedangadas Mohanty. “Effect of limited statistics on higher order cumulants measurement in heavy-ion collision experiments”. *Nucl. Phys. A* 991 (2019), 121608. arXiv: [1809.08892 \[nucl-ex\]](#).
- [38] B. Efron. “Bootstrap Methods: Another Look at the Jackknife”. *The Annals of Statistics* 7 (1979), 1–26.
- [39] Volodymyr Vovchenko and Horst Stoecker. “Thermal-FIST: A package for heavy-ion collisions and hadronic equation of state”. *Comput. Phys. Commun.* 244 (2019), 295–310. arXiv: [1901.05249 \[nucl-th\]](#).
- [40] L. Adamczyk et al. “Bulk Properties of the Medium Produced in Relativistic Heavy-Ion Collisions from the Beam Energy Scan Program”. *Phys. Rev. C* 96.4 (2017), 044904. arXiv: [1701.07065 \[nucl-ex\]](#).
- [41] J. Cleymans, H. Oeschler, K. Redlich, et al. “Comparison of chemical freeze-out criteria in heavy-ion collisions”. *Phys. Rev. C* 73 (2006), 034905. arXiv: [hep-ph/0511094](#).

- [42] M. Bleicher et al. “Relativistic hadron hadron collisions in the ultrarelativistic quantum molecular dynamics model”. *J. Phys. G* 25 (1999), 1859–1896. arXiv: [hep-ph/9909407](#).
- [43] Sukanya Sombun, Kristiya Tomuang, Ayut Limphirat, et al. “Deuteron production from phase-space coalescence in the UrQMD approach”. *Phys. Rev. C* 99.1 (2019), 014901. arXiv: [1805.11509 \[nucl-th\]](#).
- [44] Volodymyr Vovchenko, Benjamin Dönigus, and Horst Stoecker. “Canonical statistical model analysis of p-p , p -Pb, and Pb-Pb collisions at energies available at the CERN Large Hadron Collider”. *Phys. Rev. C* 100.5 (2019), 054906. arXiv: [1906.03145 \[hep-ph\]](#).
- [45] Volodymyr Vovchenko and Volker Koch. “Particlization of an interacting hadron resonance gas with global conservation laws for event-by-event fluctuations in heavy-ion collisions”. *Phys. Rev. C* 103.4 (2021), 044903. arXiv: [2012.09954 \[hep-ph\]](#).
- [46] “First measurement of antideuteron number fluctuations at energies available at the Large Hadron Collider” (Apr. 2022). arXiv: [2204.10166 \[nucl-ex\]](#).
- [47] Adam Bzdak, Volker Koch, Dmytro Oliinychenko, et al. “Large proton cumulants from the superposition of ordinary multiplicity distributions”. *Phys. Rev. C* 98.5 (2018), 054901. arXiv: [1804.04463 \[nucl-th\]](#).

## Appendix 3.A Event-by-Event Deuteron Distributions

Distributions for 0-5% and 70-80% centrality at nine different collision energies  $\sqrt{s_{NN}} = 7.7 - 200$  GeV are shown in Figures 3.1 and Figures 3.2, respectively. The deuteron number in an event is the multiplicity of the deuteron selected in the acceptance of our measurement *i.e.* within  $0.8 < p_T < 4.0$  GeV/ $c$  and  $|y| < 0.5$ . These numbers are not corrected for detection efficiency. The distributions are normalized with the number of events in a given centrality.

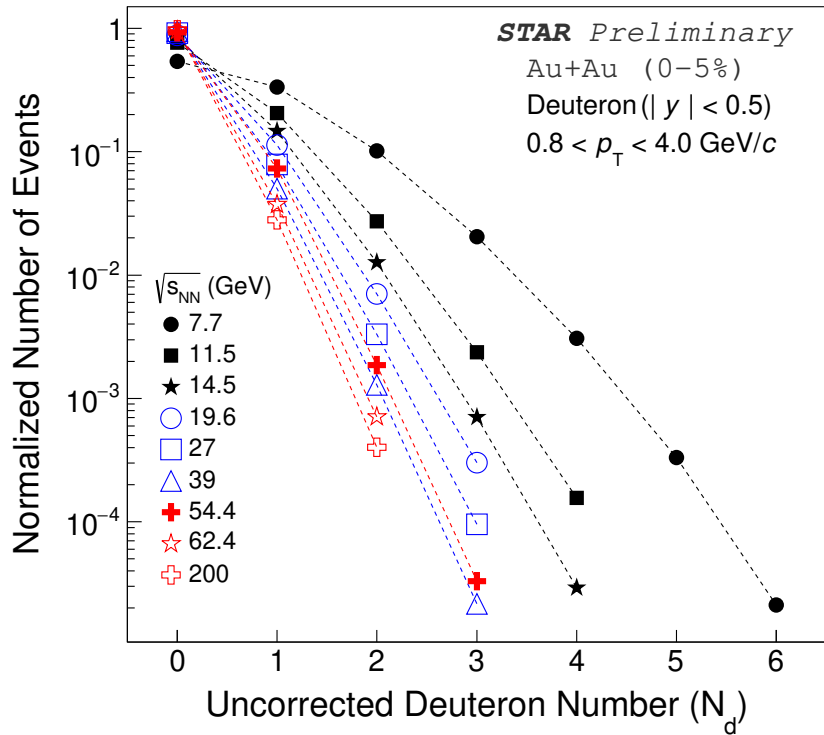


Figure 3.1: Event-by-event deuteron number distributions for 0-5% central Au+Au collisions for different collision energies,  $\sqrt{s_{NN}} = 7.7\text{--}200$  GeV measured by STAR. For each  $\sqrt{s_{NN}}$  and centrality, the event-by-event distributions are normalized to the total number of events. Lines connecting the data points are shown to guide the eye. The statistical uncertainties are within the sizes markers. The deuteron numbers shown on the  $x$ -axis are not corrected for detection efficiency.

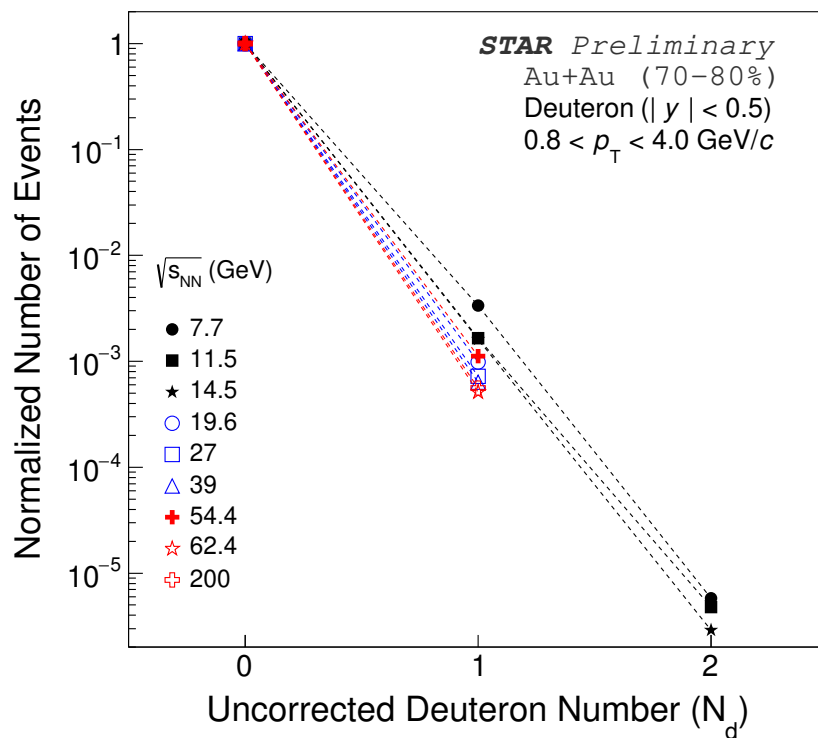


Figure 3.2: Event-by-event deuteron number distributions for 70-80% peripheral Au+Au collisions for different collision energies,  $\sqrt{s_{NN}} = 7.7\text{--}200$  GeV measured by STAR. For each  $\sqrt{s_{NN}}$  and centrality, the event-by-event distributions are normalized to the total number of events. Lines connecting the data points are shown to guide the eye. The statistical uncertainties are within the sizes markers. The deuteron numbers shown on the  $x$ -axis are not corrected for detection efficiency.



## Chapter 4

# Limits of Thermalization in Relativistic Heavy Ion Collisions

In this chapter, the study on the test of the thermal nature of the system created in heavy-ion collisions [1] is discussed. Measurements from the STAR experiment on higher order moments of event-by-event net-particle fluctuations [2–5] including the mean yields of pions, kaons, and protons (as well as their anti-particles) [6, 7] are utilized to perform the test of thermalization. These measurements are compared to the corresponding susceptibilities calculated in a Hadron Resonance Gas (HRG) model [1, 8, 9]. The effect of resonance decay and experimental acceptances are taken into account in the model calculations. Further, these thermal model calculations are compared to results from a hadronic transport (UrQMD) model [10, 11], where the thermal equilibrium of the matter produced in the heavy-ion collisions is absent. Comparison of the HRG model calculations with most central, peripheral Au+Au collisions measurements from STAR, and with the UrQMD model at seven different collision energies enables us to systematically study the thermal nature of the system formed in high-energy heavy ion collisions.

Section 4.1 gives an introduction to our current understanding of chemical freeze-out and thermalization in heavy-ion collisions that has been gained primarily via thermal model studies of mean yields and their ratios of produced particles. Section 4.2 describes the thermodynamic modeling of the Hadron Resonance Gas (HRG) model. The implementation method of resonance decay to calculate higher-order moments is also discussed in this section. This is followed by a brief discussion in Section 4.3 on the set of observables measured in the STAR experiment, which have been utilized to study the thermalization of the system. Section 4.4 describes the analysis method while the results and discussion on the findings of this study are presented in Section 4.5. Finally, the chapter ends with a conclusion in Section 4.6.

## 4.1 Chemical Freeze-out and Thermalization

Thermalization of the system created in high-energy heavy-ion collisions is one of the most used underlying assumptions in heavy-ion physics. The QCD phase diagram that is outlined by the temperature and chemical potential utilizes the scenario of thermal equilibrium to depict the phase structure of matter. Similarly, the comparison studies of theoretical calculations with the experimental measurements are performed often with the assumption that the system created in high-energy heavy-ion collisions is at/near the thermal equilibrium. For example, lattice QCD calculation assumes a thermalized system characterized by temperature and chemical potentials, and several comparisons to the experimental results have been done to determine pseudo-critical temperature ( $T_c$ ) and chemical freeze-out temperatures. Further, in the experimental search for signals of a crossover [12, 13], first-order phase transition, and a QCD critical point [4] the underlying assumption is that the fireball produced in the collisions should have come to local thermodynamic equilibrium during

its evolution [14, 15].

However, there is no apparent physical reason or theoretical proof that thermalization has to be achieved in heavy-ion collisions [16]. Experimental tests of thermalization are non-trivial for these femto-scale systems created in heavy-ion collisions: not just because the systems are small, but also because they are expanding [7].

Quantum processes that produce particles in high-energy heavy-ion collisions, do not create them into thermal equilibrium. Local equilibrium (both thermal and chemical) requires multiple collisions among the particles and the means of globally conserved quantities reaching their local equilibrium values faster than fluctuations in them [1]. In cosmology, the study of fluctuations is widely utilized to understand the thermodynamic nature of the early universe [17, 18].

Attaining and maintaining local thermodynamic equilibrium in a fast-expanding system like in heavy-ion collisions is non-trivial. The scales such as local volume and the rate at which equilibrium is reached are determined by the microscopic dynamics of the system, while the global properties like the expansion rate and system size are determined by the conditions under which the system is set up. Local equilibrium in the femto-scale systems created in heavy-ion collisions can be characterized by a temperature  $T$ , and three chemical potentials  $\mu_B$ ,  $\mu_S$ , and  $\mu_Q$ . The chemical potentials correspond to the conserved quantities that are net-baryon number ( $B$ ), strangeness ( $S$ ), and electric charge ( $Q$ ).

*A priori*, though there is no physical reason for thermal equilibrium, the chemical freeze-out parameters which give the best agreement between particle yields (i.e means of produced particle number distributions) in a statistical thermal model of an ideal gas of hadrons and resonances (HRG) [9, 19–22], are commonly quoted as thermodynamic variables. However, these HRG models also seem to describe (though with a relatively higher value of  $\chi^2$ ) mean yield data in  $e^+e^-$  and pp collisions, where one does not expect

enough interactions among the constituents for a thermalized matter to be formed [23–25]. Similarly, yields of protons, kaons, and pions in peripheral collisions, as well as the production of heavy quarks [26] and light nuclei [27], are described by thermal models. These claims introduce severe uncertainty in the physical interpretation of the freeze-out parameters derived using mean yields in terms of thermal equilibrium conditions.

In this study, we performed a test whether a common thermodynamic equilibrium description is possible to describe higher order moments of net-particle fluctuations and mean particle number in heavy-ion collisions. If the medium is thermalized well enough to produce heavy quarkonia and nuclei in chemical equilibrium, then the higher-order cumulants which represent the tails of a distribution can also be explained purely from thermodynamic effects.

## 4.2 Thermodynamic Modeling of Heavy-Ion Collisions

### 4.2.1 Hadron Resonance Gas (HRG) model

The Hadron Resonance Gas model considers a gas of hadrons and resonances in a static thermal and chemical equilibrium. The ideal HRG model conventionally treats its constituents as non-interacting. The thermal abundance of particles is determined by their mass, degeneracy, and thermodynamic conditions of the gas. Resonance decay further can modify the particle numbers. The Grand Canonical Ensemble (GCE) setup of the HRG model allows the fluctuations in conserved numbers. If the acceptance window in the experimental measurement is sufficiently small compared to the full system size, the mean and higher order fluctuations of measured conserved quantities can be effectively considered to be grand canonical in nature. On the contrary, if the data is for the full  $4\pi$  coverage, then a micro-canonical treatment with exact conservation of charges and energy would have

been appropriate. GCE approach has been extensively used to study the yields [7, 28, 29] as well as fluctuations [30–32] of produced hadrons in the field of high-energy heavy-ion collisions. As discussed in Ref. [33], the effect of global conservation of charges on different order of cumulants depends on the fraction of charges falling in the measurement acceptance. This fraction is found to be small and within the experimental uncertainties for the data up to the third-order cumulant used in the current study.

In the GCE framework, the logarithm of the partition function is obtained as a sum of all hadrons and resonances and their antiparticles, which can be split into contributions from baryons and mesons [9],

$$\ln Z(T, \mu, V) = \sum_M \ln Z_i(T, \mu_i, V) + \sum_B \ln Z_i(T, \mu_i, V) \quad (4.1)$$

where

$$\ln Z_i(T, \mu_i, V) = \pm \frac{V g_i}{2\pi^2} \int p^2 dp \ln \{1 \pm \exp[(\mu_i - E)/T]\} \quad (4.2)$$

$T$  is the fireball temperature,  $V$  is the volume of the system,  $\mu_i$  is the chemical potential, and  $g_i$  is the degeneracy factor of the  $i^{\text{th}}$  particle. If the system is in chemical equilibrium then the values of  $\mu_i$  are fixed by chemical potentials corresponding to conserved charges of the overall system. The total chemical potential of the particle,  $\mu_i = B_i \mu_B + Q_i \mu_Q + S_i \mu_S$ , where  $B_i$ ,  $Q_i$ , and  $S_i$  are the baryon, electric charge, and strangeness number of the  $i^{\text{th}}$  particle.  $\mu_B$ ,  $\mu_Q$ , and  $\mu_S$  are the chemical potentials corresponding to the conserved charges. The  $+ve$  and  $-ve$  signs are for baryons and mesons, respectively.

In the limit of large volume, the thermodynamic pressure ( $P$ ) can then be obtained from logarithm of the partition function as:

$$P(T, \mu_i, V) = \frac{T}{V} \ln Z_i = \pm \frac{T g_i}{2\pi^2} \int p^2 dp \ln \{1 \pm \exp(\mu_i - E)/T\} \quad (4.3)$$

In the HRG model, constituents of the fireball obey the free particle dispersion relation [34]. For a particle of mass  $m$ , with transverse momentum  $p_T$ , pseudo-rapidity  $\eta$  and azimuthal angle  $\phi$ , the volume element ( $d^3p$ ) and energy ( $E$ ) can be written as  $d^3p = p_T m_T \cosh \eta dp_T d\eta d\phi$  and  $E = m_T \cosh \eta$ , respectively, where  $m_T = \sqrt{p_T^2 + m^2}$ . One can choose proper integration ranges in  $\eta$ ,  $p_T$ , and  $\phi$  to reflect the constrained phase space coverage of the detector. The fluctuations of the conserved numbers are obtained from the derivatives of the thermodynamic pressure with respect to the corresponding chemical potentials.

The  $n$ -th order generalized susceptibilities ( $\chi_X^{(n)}$ ), where  $X$  represents baryon, electric charge, or strangeness indices, can be expressed as,

$$\chi_X^{(n)} = \frac{d^n [P(T, \mu)/T^4]}{d(\mu_X/T)^n} \quad (4.4)$$

For mesons,  $\chi_X$  can be expressed as

$$\begin{aligned} \chi_{X,meson}^{(n)} &= \frac{X^n}{VT^3} \int p^2 dp \sum_{k=0}^{\infty} (k+1)^{n-1} \\ &\times \exp\left\{-\frac{(k+1)E}{T}\right\} \exp\left\{\frac{(k+1)\mu}{T}\right\}. \end{aligned} \quad (4.5)$$

and for baryons,

$$\begin{aligned} \chi_{X,baryon}^{(n)} &= \frac{X^n}{VT^3} \int p^2 dp \sum_{k=0}^{\infty} (-1)^k (k+1)^{n-1} \\ &\times \exp\left\{-\frac{(k+1)E}{T}\right\} \exp\left\{\frac{(k+1)\mu}{T}\right\}, \end{aligned} \quad (4.6)$$

where  $X$  represents either  $B_i$ ,  $Q_i$  or  $S_i$  of the  $i$ -th particle. The total susceptibility will be the sum of contributions from mesons and baryons as  $\chi_X^n = \sum \chi_{X,mesons}^n + \sum \chi_{X,baryons}^n$ .

For any conserved charge of type  $X$ , the first derivative is related to the mean value  $C_1^X$  as,

$$C_1^X \equiv \langle X \rangle = VT^3 \chi_X^{(1)}, \quad (4.7)$$

The second derivative with respect to  $\mu_X/T$  gives the average of squared number fluctuations  $\langle(\delta X)^2\rangle$  or namely variance as,

$$C_2^X \equiv \langle(\delta X)^2\rangle = VT^3 \chi_X^{(2)} \quad (4.8)$$

where  $\delta X = X - \langle X \rangle$ . The third  $\chi_X^{(3)}$  and the fourth  $\chi_X^{(4)}$  order susceptibilities are related to  $C_3^X$  and  $C_4^X$ , respectively as follows:

$$C_3^X \equiv \langle(\delta X)^3\rangle = VT^3 \chi_X^{(3)}, \quad (4.9)$$

$$C_4^X \equiv \langle(\delta X)^4\rangle - 3(\langle(\delta X)^2\rangle)^2 = VT^3 \chi_X^{(4)}. \quad (4.10)$$

The covariances are related to the off-diagonal susceptibilities

$$C_{1,1}^{X,Y} = VT^3 \chi_{X,Y}^{(1,1)} = VT^3 \frac{d^2[P(T, \mu)/T^4]}{d(\mu_x/T)d(\mu_y/T)}. \quad (4.11)$$

The hadrons and resonances with mass up to 2.5 GeV listed in the Particle Data Group (PDG) booklet [35] are included in the model. Usually, ratios of susceptibilities are calculated in order to remove the ambiguously known system volume dependence and for direct comparison with the experimental data. Ratios of susceptibilities are related to the cumulants ratios as follows.

$$\frac{C_2}{C_1} = \frac{\sigma^2}{M} = \frac{\chi^{(2)}}{\chi^{(1)}}, \quad \frac{C_3}{C_2} = S\sigma = \frac{\chi^{(3)}}{\chi^{(2)}}, \quad \frac{C_4}{C_2} = \kappa\sigma^2 = \frac{\chi^{(4)}}{\chi^{(2)}} \quad (4.12)$$

Different variants of the HRG models are also used to study freeze-out in heavy-ion collisions [19, 20, 36–42]. In this study, we have used the ideal HRG model in the GCE framework which has the least number of thermodynamic parameters.

Susceptibilities defined using Equations 4.4 and 4.11 are “*primordial*” in nature. The effect of resonance decay on them is discussed in the next subsection.

## 4.2.2 Resonance decay contributions

The generalized susceptibilities,  $\chi_X^n$ , as defined in the previous subsection are various order derivatives of the equilibrium pressure with respect to chemical potentials. These susceptibilities give the primordial part of the number fluctuations under given thermodynamic conditions. The observed final cumulants include fluctuations arising due to the decay of resonances. As these two sources of fluctuations are uncorrelated, the probabilities factorize, and then the partition functions may be multiplied. The number susceptibility of the final state particles in total includes the primordial part and resonance decay contributions as,  $\chi_{X, total}^{(n)} = \chi_{X, primordial}^{(n)} + \chi_{X, reso. dec.}^{(n)}$ . In the following, considering the facts that (a) resonance number fluctuates due to pure thermal effects, and (b) their decay processes are probabilistic in nature, we derive expressions for susceptibilities up to 4<sup>th</sup>-order of the number fluctuation of daughter particles.

### 4.2.2.1 Single Resonance Decay

Suppose there is  $N$  number of resonances of type  $\alpha$  that are thermally produced in the system. Assume that there are  $L$  different decay channels for the mother resonance  $\alpha$  decay to daughters of type  $\beta$ . A decay channel labelled  $r$  (with  $1 \leq r \leq L$ ) has branching ratio  $b_r$  and produces  $n_r$  number of  $\beta$  daughters. The sum of branching ratios satisfy  $\sum_{r=1}^L b_r = 1$ ; total probability being unity. If  $N_r$  of type  $\alpha$  decay in channel  $r$ , then the probability distribution of  $N_r$  is binomial with probability  $b_r$ . We can make use of vector  $\mathbf{N}$  to represent  $N_r$ . Since each decay is independent of the others, the joint distribution of  $N_r$  for all  $L$  channels denoted as,  $P(\mathbf{N}) \equiv P(N_1, N_2, \dots, N_r, \dots, N_L)$  is given by the multinomial distribution as,

$$P(\mathbf{N}) = N! \left( \prod_{r=1}^L \frac{b_r^{N_r}}{N_r!} \right) \times \delta \left( N - \sum_{r=1}^L N_r \right), \quad (4.13)$$

with the delta function imposing the constraint that the total number of mother resonance  $\alpha$  which decay must be equal to the number produced thermally.

As the number of  $\beta$ s produced in channel  $r$  is  $n_r$ , we can use a vector  $\mathbf{n}$  to represent them. Then the total number of  $B$  type daughters produced in total is  $n = \mathbf{N} \cdot \mathbf{n}$ . Let the probability distribution of  $n$  denoted by  $P(n)$  and is related to  $P(\mathbf{N})$  as

$$P(n) = \sum_{\mathbf{N}} P(\mathbf{N}) \times \delta(n - \mathbf{N} \cdot \mathbf{n}), \quad (4.14)$$

where the sum is over all values of  $\mathbf{N}$  which are possible given a total  $N$ . The generating function for  $n$  can be written using the usual expression:  $G(\mu) = \sum_n P(n)e^{\mu n}$ , where  $\mu$  is an auxiliary variable. Using Equation 4.14 we find

$$G(\mu) = \left( \sum_{r=1}^L b_r e^{\mu n_r} \right)^N, \quad \text{and} \quad C_m = \left. \frac{d^m G(\mu)}{d\mu^m} \right|_{\mu=0}. \quad (4.15)$$

for the cumulants of  $n$ . The first and second-order cumulants for example are,

$$C_1 = N \sum_{r=1}^L b_r n_r = N\bar{n}, \quad \text{and} \quad (4.16)$$

$$C_2 = N \left[ \sum_{r=1}^L b_r n_r^2 - (\bar{n})^2 \right] = N \overline{(\Delta n)^2}, \quad (4.17)$$

where the bar symbol above a quantity denotes averaging with probabilities  $b_r^\alpha$  and  $\Delta n = n - \bar{n}$ . Using Equation 4.15 higher order cumulants of fluctuations in the number of  $\beta$  due to decays can be derived, if they only come from decays of a single mother resonance  $\alpha$ .

#### 4.2.2.2 Decays of Multiple Resonances

In practice, all daughters of different types of  $\beta$  can come from several types of mother resonances  $\alpha$ . As the decay of each mother resonance is independent of others, the generalized generating function can be written as the product over each. One has to add

subscripts  $\alpha$  and  $\beta$  to keep track of multiple types of resonances and daughter particles.

Then  $G(\mu) \equiv G(\mu_1, \mu_2, \dots, \mu_d)$  takes the form [43]

$$G(\mu) = \prod_{\alpha} \left( \sum_{r=1}^L b_r^{\alpha} \prod_{\beta=1}^d e^{\mu_{\beta} n_{\beta,r}^{\alpha}} \right)^{N_{\alpha}}, \quad (4.18)$$

where  $N_{\alpha}$  is number of resonances of type  $\alpha$  produced in thermal equilibrium,  $b_r^{\alpha}$  is the branching ratio of  $r^{th}$  decay channel of resonance  $\alpha$ ,  $\mu_{\beta}$  is auxiliary parameter corresponding to  $\beta$  daughter type.  $n_{\beta,r}^{\alpha}$  is the number of  $\beta$  daughter particles coming from  $r^{th}$  decay channel of one  $\alpha$  type resonance. Various orders of moments for the daughter numbers can be extracted by taking derivatives of the generalized moment-generating function as follows. For simplicity, let us define  $m^{th}$  order derivative as:  $D_{\beta}^{(m)} \equiv \left( \frac{\partial}{\partial \mu_{\beta}} \right)^m$ . The first and second-order moments of  $\beta$  type daughter particle are,

$$N_{\beta} = D_{\beta}^{(1)}(G(\mu)) \Big|_{\mu=0} = \sum_{\alpha} N_{\alpha} \times \sum_{r=1}^L b_r^{\alpha} n_{\beta,r}^{\alpha} = \sum_{\alpha} N_{\alpha} \overline{n_{\beta}^{\alpha}}, \quad (4.19)$$

$$N_{\beta}^2 = D_{\beta}^{(2)}(G(\mu)) \Big|_{\mu=0} = \sum_{\alpha} \left[ N_{\alpha} (N_{\alpha} - 1) (\overline{n_{\beta}^{\alpha}})^2 + N_{\alpha} \overline{(n_{\beta}^{\alpha})^2} \right], \quad (4.20)$$

where,  $\overline{(\dots)}$  symbol denotes average over decay branches. Higher-order moments are similarly obtained by taking higher derivatives of the generating function. The mixed moment between  $\beta$  and  $\gamma$  types of daughters can be obtained by taking simultaneous derivative w.r.t.  $\mu_{\beta}$  and  $\mu_{\gamma}$ . These moments encode contributions only coming from the probabilistic nature of decay.

#### 4.2.2.3 Inclusion of Thermal Fluctuations

In addition to the probabilistic nature of resonance decay, the number of resonances,  $N_{\alpha}$ , undergo usual grand canonical fluctuations in the thermodynamic equilibrium. These fluctuations have to be included along with the fluctuations in the decays. Since fluctuations

in  $N_\alpha$  are independent of the decays, the number fluctuations of  $N_\alpha$  and  $n_{\beta,r}^\alpha$  are independent. For thermal averaging in GCE, we employ the notation as  $\langle(\dots)\rangle \equiv \langle(\dots)\rangle_{GCE}$ . Moments up to  $2^{nd}$  order mentioned in Equations 4.19 and 4.20, after thermal averaging take the form as

$$\langle N_\beta \rangle = \sum_\alpha \langle N_\alpha \rangle \overline{n_\beta^\alpha}, \quad (4.21)$$

$$\langle N_\beta^2 \rangle = \sum_\alpha \left[ \left( \langle N_\alpha^2 \rangle - \langle N_\alpha \rangle \right) (\overline{n_\beta^\alpha})^2 + \langle N_\alpha \rangle \overline{(n_\beta^\alpha)^2} \right]. \quad (4.22)$$

Using the expressions for moments, the cumulants up to  $2^{nd}$  order for  $\beta$  type daughter particles originating from resonance decay can be written as,

$$C_1^{\beta, Res. dec.} = \langle N_\beta \rangle = \sum_\alpha \langle N_\alpha \rangle \overline{n_\beta^\alpha}, \quad (4.23)$$

$$C_2^{\beta, Res. dec.} = \langle N_\beta^2 \rangle - (\langle N_\beta \rangle)^2 = \sum_\alpha \left( \langle (\Delta N_\alpha)^2 \rangle (\overline{n_\beta^\alpha})^2 + \langle N_\alpha \rangle \overline{(\Delta n_\beta^\alpha)^2} \right), \quad (4.24)$$

where we used the relations:  $\langle (\Delta N_\alpha)^2 \rangle = \langle N_\alpha^2 \rangle - \langle N_\alpha \rangle^2$  and  $\overline{(\Delta n_\beta^\alpha)^2} = \overline{(n_\beta^\alpha)^2} - (\overline{n_\beta^\alpha})^2$ . The cumulants of fluctuations of mother resonance numbers *i.e.*,  $\langle N_\alpha \rangle$ ,  $\langle (\Delta N_\alpha)^2 \rangle$  are expressible in terms of susceptibilities in GCE as:  $\langle N_\alpha \rangle = VT^3 \chi_\alpha^{(1)}$  and  $\langle (\Delta N_\alpha)^2 \rangle = VT^3 \chi_\alpha^{(2)}$ , where  $\chi_\alpha^{(m)} = \frac{\partial^m [P/T^4]}{\partial (\mu_\alpha/T)^m}$ . The chemical potential of mother resonance is given by  $\mu_\alpha = B_\alpha \mu_B + S_\alpha \mu_S + Q_\alpha \mu_Q$ , where  $B_\alpha$  is its baryon number,  $Q_\alpha$  its charge, and  $S_\alpha$  its strangeness.

Following the above approach, further higher-order diagonal and off-diagonal cumulants of daughter particle number fluctuations can be obtained. Below, we write down the expressions for diagonal cumulants up to fourth-order and first-order off-diagonal cumulants

for resonance decay contributions.

$$C_1^{\beta, Res. dec.} = VT^3 \sum_{\alpha} \left[ \chi_{\alpha}^{(1)} \overline{n_{\beta}^{\alpha}} \right], \quad (4.25)$$

$$C_2^{\beta, Res. dec.} = VT^3 \sum_{\alpha} \left[ \chi_{\alpha}^{(2)} (\overline{n_{\beta}^{\alpha}})^2 + \chi_{\alpha}^{(1)} \overline{(\Delta n_{\beta}^{\alpha})^2} \right], \quad (4.26)$$

$$C_3^{\beta, Res. dec.} = VT^3 \sum_{\alpha} \left[ \chi_{\alpha}^{(3)} \overline{n_{\beta}^{\alpha}}^3 + 3\chi_{\alpha}^{(2)} \overline{n_{\beta}^{\alpha}} \overline{(\Delta n_{\beta}^{\alpha})^2} + \chi_{\alpha}^{(1)} \overline{(\Delta n_{\beta}^{\alpha})^3} \right], \quad (4.27)$$

$$C_4^{\beta, Res. dec.} = VT^3 \sum_{\alpha} \left[ \chi_{\alpha}^{(4)} \overline{n_{\beta}^{\alpha}}^4 + 6\chi_{\alpha}^{(3)} \overline{n_{\beta}^{\alpha}}^2 \overline{(\Delta n_{\beta}^{\alpha})^2} + \chi_{\alpha}^{(2)} \left[ 3 \overline{(\Delta n_{\beta}^{\alpha})^2}^2 + 4\overline{n_{\beta}^{\alpha}} \overline{(\Delta n_{\beta}^{\alpha})^3} \right] + \chi_{\alpha}^{(1)} \overline{(\Delta n_{\beta}^{\alpha})^4} \right], \quad (4.28)$$

and the off-diagonal cumulant is,

$$C_{1,1}^{\beta,\gamma, Res. dec.} = \langle \Delta N_{\beta} \Delta N_{\gamma} \rangle = VT^3 \sum_{\alpha} \left[ \chi_{\alpha}^{(2)} \overline{n_{\beta}^{\alpha}} \overline{n_{\gamma}^{\alpha}} + \chi_{\alpha}^{(1)} \overline{(\Delta n_{\beta}^{\alpha} \Delta n_{\gamma}^{\alpha})} \right], \quad (4.29)$$

where the term  $\overline{(\Delta n_{\beta}^{\alpha})^4}$  in Equation 4.28 denotes the 4<sup>th</sup> order cumulant of  $n_{\beta}^{\alpha}$  and can be written as:  $\overline{(\Delta n_{\beta}^{\alpha})^4} - 3 \overline{(\Delta n_{\beta}^{\alpha})^2}^2$ .

The final cumulant of any order is:  $C_n^{\beta, Total} = C_n^{\beta, Primordial} + C_n^{\beta, Res. dec.}$ . We employ the above expressions to calculate the cumulants in this study.

### 4.3 Experimental Observables

STAR experiment using the Beam Energy Scan phase-I (BES-I) data has performed measurements on higher-order cumulants of net-charge, net-proton, and net-kaon distributions at several collision energies *i.e.*,  $\sqrt{s_{NN}} = 7.7$  to 200 GeV. Event-by-event net-charge (the difference in the total number of positive charges and negative charges in an event) distributions were obtained using the TPC detector at STAR in momentum range  $0.2 < p_T < 2.0$  GeV/*c* and a pseudo-rapidity range of  $|\eta| < 0.5$  [2]. Similarly, the net kaon [3] and net

all observables	$C_1^{\pi^\pm}, C_1^{K^\pm}, C_1^p, C_1^{\bar{p}},$ $C_2^{NQ}/C_1^{NQ}, C_2^{NK}/C_1^{NK}, C_2^{NP}/C_1^{NP}, C_{1,1}^{NP,NK}/C_2^{NK},$ $C_3^{NQ}/C_2^{NQ}, C_3^{NK}/C_2^{NK}, C_3^{NP}/C_2^{NP},$ $C_4^{NQ}/C_2^{NQ}, C_4^{NK}/C_2^{NK}, C_4^{NP}/C_2^{NP}.$
13 observable set	$C_1^{\pi^\pm}, C_1^{K^\pm}, C_1^p, C_1^{\bar{p}},$ $C_2^{NQ}/C_1^{NQ}, C_2^{NK}/C_1^{NK}, C_2^{NP}/C_1^{NP}, C_{1,1}^{NP,NK}/C_2^{NK},$ $C_3^{NQ}/C_2^{NQ}, C_3^{NK}/C_2^{NK}, C_3^{NP}/C_2^{NP}.$
11 observable set	$C_1^{\pi^\pm}, C_1^{K^\pm}, C_1^p, C_1^{\bar{p}},$ $C_2^{NQ}/C_1^{NQ}, C_2^{NK}/C_1^{NK}, C_{1,1}^{NP,NK}/C_2^{NK},$ $C_3^{NQ}/C_2^{NQ}, C_3^{NK}/C_2^{NK}.$

Table 4.1: The full set of observables constructed from distributions of event-to-event fluctuations of hadrons by the STAR experiment are shown in the first row. We use 13 of these observables for the test of thermalization. The fourth-order cumulants are used for independent verification of the hypothesis of thermodynamic equilibrium. At lower collision energies where the full thermodynamic equilibrium of all listed observables is not supported, we use the 11 observable sets as an effective measure to extract the freeze-out conditions.

proton [4] distributions were measured using both TPC and Time-of-Flight detector within momentum ranges of  $0.2 < p_T < 1.6$  GeV/c and  $0.4 < p_T < 2.0$  GeV/c, respectively.

STAR experiment has also published [5] the covariance <sup>1</sup>  $C_{1,1}^{NP,NK}$  that is measured within  $|\eta| < 0.5$  and  $0.4 < p_T < 1.6$  GeV/c. The cumulants of distributions are corrected for detector inefficiencies and other analysis artifacts (details discussed in Chapter 3). Similarly, the mean yields of the pion, kaon, and proton were also measured in Au+Au collisions at several collision energies [6, 7]. The measurements for small impact parameter collisions (called central 0-5%) are of main interest in this study. The list of the full set of observables available from the experiment is shown in Table 4.1, along with the subsets that are used in this analysis.

<sup>1</sup>The measured covariances  $C_{1,1}^{NQ,NP}$  and  $C_{1,1}^{NQ,NK}$  were under investigation in the STAR collaboration for the method of efficiency correction, while this study was performed. Subsequently, the revised results were published in [44]

## 4.4 Analysis Method

At each collision energy ( $\sqrt{s_{\text{NN}}}$ ), the experimental observables are compared with their corresponding calculations from the HRG model. The chemical freeze-out parameters, namely  $T$ ,  $\mu_B$ ,  $\mu_S$  and  $\mu_Q$ , are varied to minimize

$$\chi^2 = \sum_{i=1}^N \left( \frac{\Delta_i}{E_i} \right)^2, \quad \text{where } \Delta_i = R_i^{\text{Exp}} - R_i^{\text{HRG}}, \quad (4.30)$$

where  $N$  is the number of observables used in this calculation.  $R_i^{\text{Exp}}$  and  $R_i^{\text{HRG}}$  are experimental measurements and HRG model calculations, respectively, for the  $i^{\text{th}}$  observable, and  $E_i$  is the statistical uncertainty of the measurement. The value of  $\chi^2$  defined in Equation 4.30 determines the goodness of comparison. It is used to find the values and errors of the five parameters,  $V$ ,  $T$ ,  $\mu_B$ ,  $\mu_S$ , and  $\mu_Q$  in the thermodynamic model.

In the existing literature, reported conclusions about the freezeout of fluctuations are often established on the analysis of a few selected experimental fluctuation observables and lack any detailed or comprehensive study of the fluctuation data. In this study, we used extensive datasets from the STAR experiment and then subjected them to the test of thermalization. We include cumulants up to the third order of different net particles and a correlation observable to extract the freeze-out parameters and utilize the fourth-order cumulants for further independent checks of the model. The resulting thirteen observable sets are listed in Table 4.1.

At first, to check whether the HRG model can diagnose the known non-thermal final states of a transport model such as UrQMD [10, 11], we generated around one million events for central (0–5%) Au+Au collisions at each  $\sqrt{s_{\text{NN}}}$ . Large values of  $\chi^2$  ( $\chi^2/\text{NDF} \sim O(100 - 10000)$ ) obtained using Equation 4.30 ruled out a thermal equilibrium description of the transport model. Further, the possible freeze-out parameters obtained from the cumulants of different orders are quite different from each other (shown in detail later

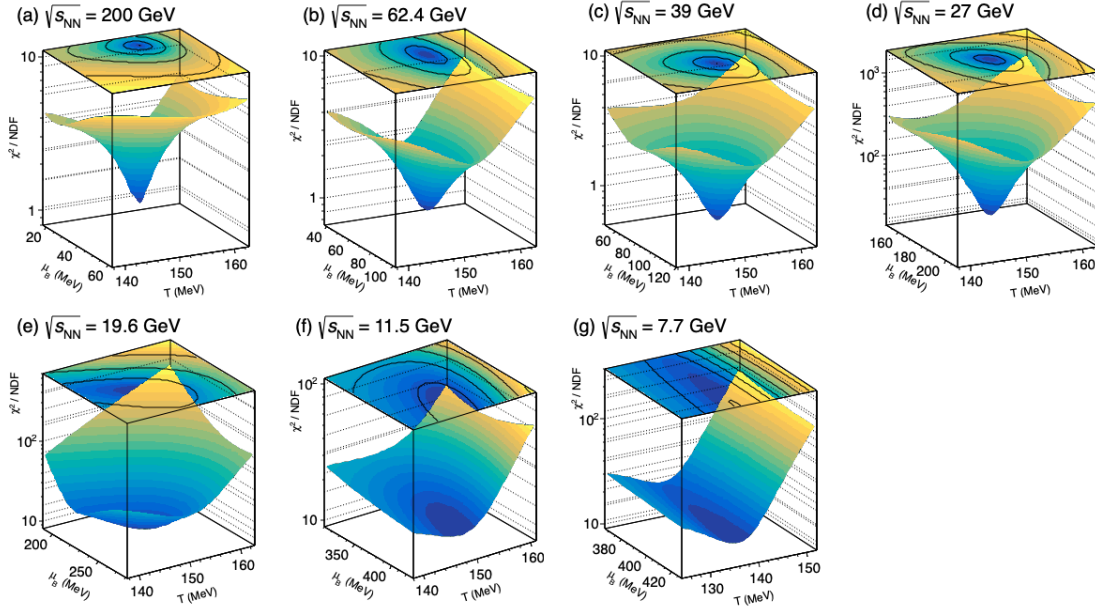


Figure 4.1:  $\chi^2/\text{NDF}$  defined using Equation 4.30 are shown as a function of  $T$  and  $\mu_B$  to represent the nature agreement of data with HRG model expectations.  $\mu_Q$  and  $\mu_S$  are held fixed to their best fit values. Shown results correspond to thirteen observable fit for the data measured in the STAR experiment for the most central (0-5%) Au+Au collisions at energies  $\sqrt{s_{\text{NN}}} = 7.7\text{--}200$  GeV.

in Figure 4.6). We repeated the analysis for the simulated data for Au+Au collisions at  $\sqrt{s_{\text{NN}}} = 200$  GeV generated using a different non-thermal model A Multi-Phase Transport (AMPT) [45]. Note that this model includes the Partonic degrees of freedom. A thermal fit of higher moments from this model also ruled out a thermodynamic description.

Figure 4.1 shows  $\chi^2/\text{NDF}$  as a function of  $T$  and  $\mu_B$  from the fit of experimental data for 0-5% Au+Au central collisions at  $\sqrt{s_{\text{NN}}} = 7.7\text{--}200$  GeV with the HRG model. The magnitude of  $\chi^2/\text{NDF}$  implies that the notion of thermodynamic equilibrium at the chemical freeze-out is admissible at the highest energies, and is less likely at lower  $\sqrt{s_{\text{NN}}}$ . Starting from  $\sqrt{s_{\text{NN}}} = 27$  to 7.7 GeV, the fit of 13 observables seems to be non-thermal in nature. Therefore we need to probe this region further.

The uncertainties on the chemical freeze-out parameters include statistical errors ob-

tained from the fits along with systematic errors estimated by varying model assumptions such as effects of radial flow, interactions through excluded volume effects, and resonance decays through including the widths of resonances [9].

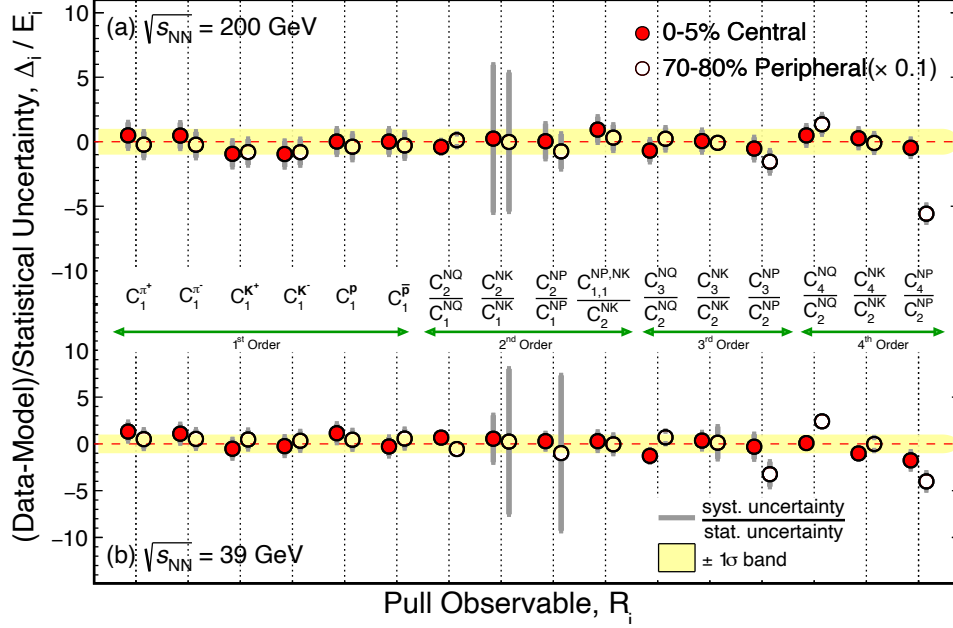


Figure 4.2: All observables studied are shown in Au+Au collisions at two representative collision energies  $\sqrt{s_{NN}} = 200$  GeV in panel (a) and  $\sqrt{s_{NN}} = 39$  GeV in panel (b). The difference between data and the HRG model values (from the best fit of 13 observables) divided by the statistical uncertainty in the data is plotted on the y-axis. Observables are mentioned along the x-axis. Note that the values for central collisions are much smaller than for peripheral. The latter is shown as open circles and is presented in the figure after scaling down by a factor of ten. The figure also shows a comparison of the magnitudes of systematic and statistical uncertainties.

## 4.5 Results and Discussion

The quality of agreement between the model and data is shown in Figure 4.2 in terms of the statistical standard deviation. The thirteen observables at their best fit values for  $\sqrt{s_{NN}} = 39$  and 200 GeV. The fourth-order cumulants which were not used in the fit are also calculated in the model, and their deviations from the data are also shown in Figure 4.2. The

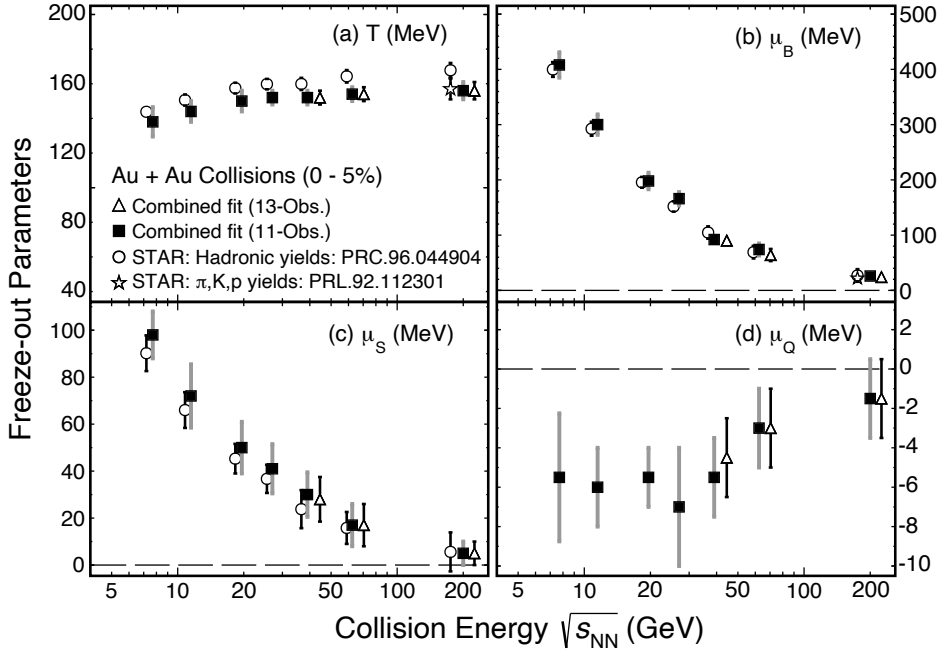


Figure 4.3: The best-fit values and errors on the chemical freeze-out parameters of the HRG model at  $\sqrt{s_{NN}} = 7.7, 11.5, 19.6, 27, 39, 62.4,$  and  $200$  GeV are obtained by the comparison of central Au+Au collisions data with the thermal model. Open triangles show results for 13 observable fits at collision energies where the fit quality is good. Solid square markers represent results for 11 observable fits at all energies. Open circles (markers slightly displaced to the left along the x-axis for clarity of presentation) represent freeze-out conditions from [7] obtained using only the mean yields of several hadrons in the STAR experiment. Also shown using open star markers parameters at  $\sqrt{s_{NN}} = 200$  GeV obtained by the fit of the mean yields of only  $\pi^\pm, K^\pm$  and  $p(\bar{p})$  [6].

deviation represented by the quantity  $\Delta_i/E_i$ , shown on the right-hand side of Equation 4.30 is plotted on the y-axis against the corresponding observable on the x-axis. One can see that the fourth-order cumulants, which were not used to extract the freeze-out parameters, remain in good agreement with the thermal description. This good agreement between measurements and calculations from the thermal equilibrium strongly suggests that the system formed in central Au+Au collisions at the highest collision energies of RHIC reaches thermal equilibrium at the chemical freeze-out stage. The peripheral collision data is quite different from the thermal equilibrium predictions.

At collision energies,  $\sqrt{s_{NN}} = 27, 19.6, 11.5,$  and  $7.7$  GeV, out of all thirteen observables the second and third-order moments of net-proton distribution show disagreement with the thermal model and hence do not allow a simultaneous description of different orders of moments. Non-thermal behavior of net-proton higher moments could be linked to the presence of a possible QCD critical point. Search for a critical point in heavy-ion collisions will require further efforts to understand the effects of finite time and size and the dynamical evolution of different orders of fluctuations.

$\sqrt{s_{NN}}$ (GeV)	Stat.Err. $\chi^2$	$\frac{\chi^2}{\text{NDF}}$	$T$ (MeV)	$\mu_B$ (MeV)	$\mu_S$ (MeV)	$-\mu_Q$ (MeV)	$R$ (fm)
7.7	34.8	4.98	138(8.5)	408(23)	98(10)	5.5(3.25)	6.6(0.5)
11.5	6.5	0.92	144(6)	300(18.5)	72(13.5)	6(2)	6.7(0.6)
19.6	14.8	2.11	150(6)	198(15)	50(11)	5.5(1.5)	7.03(0.6)
27	9.01	1.28	152(4)	166(12)	41(10)	7(3)	6.9(0.1)
39	7.38	0.85	152(4)	90(7)	28(9.5)	4.5(2)	7.08(0.5)
62.4	13.1	1.4	154(4)	64(11)	17(9)	3(2)	7.6(0.6)
200	4.17	0.46	156(5)	24(6)	5(5)	1.5(2)	8.4(0.7)

Table 4.2: Freeze-out conditions and their uncertainties are summarized for different collision energies. For  $\sqrt{s_{NN}} = 39 - 200$  GeV, the freeze-out conditions are obtained from the 13-observable fit while for  $\sqrt{s_{NN}} = 27 - 7.7$  GeV, those are obtained from the 11-observable fit.

In the collision energy region  $\sqrt{s_{NN}} = 7.7$  to  $27$  GeV, we test the thermal nature of the remaining 11 observable sets given in Table 4.1. In this test, we find that  $\chi^2/\text{NDF}$  is close to unity except at  $\sqrt{s_{NN}} = 7.7$  GeV, where it is 4.9. This implies that even though net-proton higher-order moments show an apparent deviation from thermal equilibrium, an effective thermal description of the system formed in lower collision energies at RHIC is still possible. For the sake of completeness, we performed the fit also at the remaining higher energies.

Figure 4.3 shows the best fit values of thermodynamic parameters  $T$ ,  $\mu_B$ ,  $\mu_S$ , and  $\mu_Q$  as a

function of  $\sqrt{s_{NN}}$ . At energies 200, 62.4, and 39 GeV, the thirteen observable fit results are shown with open triangle markers. Results from eleven observable sets are shown using solid square markers. Thermodynamic conditions for combined fits are in good agreement with those extracted using only the mean yields of produced hadrons (shown using open circles) in the STAR experiment [7]. The temperature values are slightly higher in Ref. [7] because of the inclusion of multi-strange hadron yields in the fits. The  $T$  and  $\mu_B$  from fits of the mean yields of  $\pi^\pm$ ,  $K^\pm$  and  $p(\bar{p})$  for  $\sqrt{s_{NN}} = 200$  GeV (shown using open stars) has better agreement with results of our study. Chemical freeze-out parameters for  $\sqrt{s_{NN}} = 39 - 200$  GeV obtained from the 13-observable fit and those for  $\sqrt{s_{NN}} = 27 - 7.7$  GeV, obtained from the 11-observable fit are also summarized in Table 4.2.

Further, using the chemical freeze-out parameters in this study, we tried to predict the transverse momentum spectra of particles. It is important to note that the mean yields and moments of fluctuations in particle numbers are  $p_T$  integrated observables. The transverse momentum spectrum is a differential measurement and provides important information about the system. Freeze-out parameters presented here have been used as inputs to a thermal model known as THERMINATOR [46] where the radial flow effect in heavy-ion collisions is implemented.

In a Blast-Wave set-up of the THERMINATOR model, the freeze-out is characterized by the model parameters such as: (1) Proper time ( $\tau_{FO}$ ), (2) Maximum transverse radius ( $\rho_{max}$ ), (3) Average transverse velocity ( $\langle\beta_T\rangle$ ), (4) Freeze-out temperature ( $T$ ), (5) Baryonic chemical potential ( $\mu_B$ ), (6) Isospin chemical potential ( $\mu_I$ ), (7) Strangeness chemical potential ( $\mu_S$ ), and (8) Charm chemical potential ( $\mu_C$ ). The parameters  $T$ ,  $\mu_B$ ,  $\mu_S$ ,  $\mu_I (= \mu_Q)$ , and  $\rho_{max} (= R)$  are fixed to the best fit values obtained from the fit of 11-observables our study at both  $\sqrt{s_{NN}} = 200$  and 19.6 GeV. The charm chemical potential is set to zero at both energies. Parameters  $\tau_{FO}$  and  $\langle\beta_T\rangle$  are varied in the THERMINATOR model to

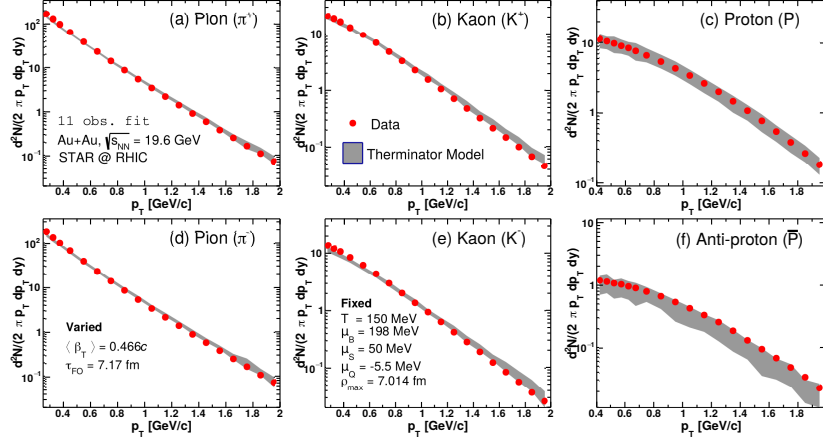


Figure 4.4: Solid markers represent  $p_T$  distribution of pion, kaon, proton, and their anti-particles for most central Au+Au collisions at  $\sqrt{s_{NN}} = 19.6$  GeV measured in the STAR experiment [7] at RHIC. Thermal model calculations using freeze-out parameters extracted in this study and average radial flow velocity  $\langle\beta\rangle = 0.466c$  is shown using the grey shaded band.

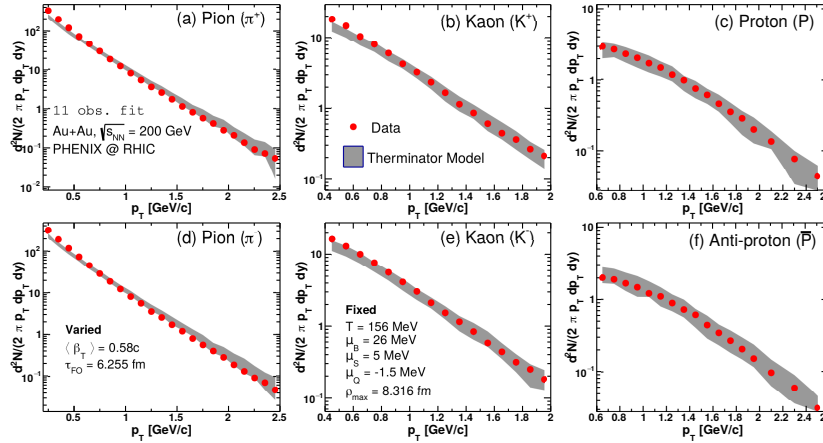


Figure 4.5: Solid markers represent transverse momentum ( $p_T$ ) spectra of pion, kaon, proton, and their anti-particles for most central Au+Au collisions at  $\sqrt{s_{NN}} = 200$  GeV measured in the PHENIX experiment [47] at RHIC. Thermal model calculations using freeze-out parameters extracted in this study and average radial flow velocity  $\langle\beta\rangle = 0.58c$ , are shown using the grey-shaded band.

describe the experimental  $p_T$  data on transverse momentum spectra. Figures 4.4 and 4.5 show comparison of most central Au+Au collisions data at  $\sqrt{s_{NN}} = 19.6$  and 200 GeV, respectively, from STAR [7] and PHENIX [47] experiments at RHIC. The shaded gray

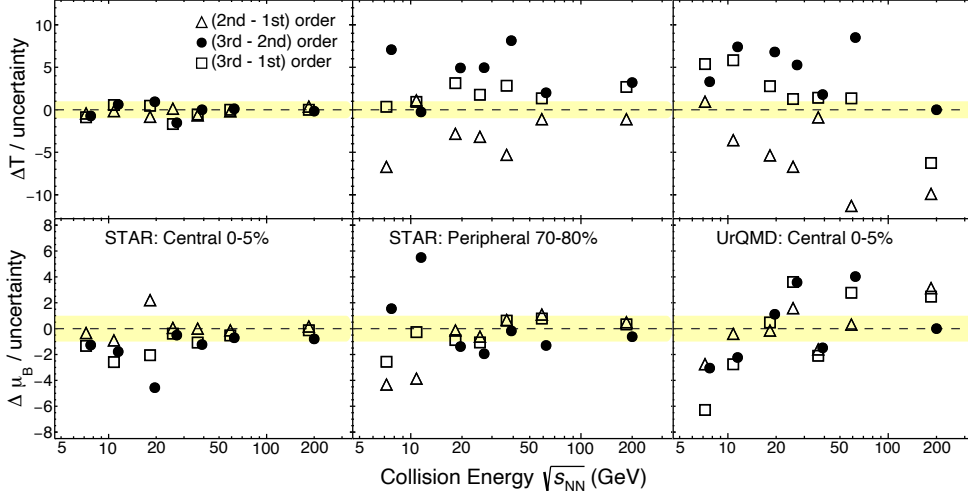


Figure 4.6: Comparison of freeze-out conditions from the fit of different orders of moments. Differences in freeze-out temperatures ( $\Delta T$  in the top row) and baryon chemical potential ( $\Delta\mu_B$  in the bottom row) are shown. The difference in temperature ( $\Delta T$ ) and baryon chemical potential ( $\Delta\mu_B$ ) from the second order to the first order, third order to second order, and third order to first order moments are shown as filled-circles, open-triangles, and open-squares, respectively. For central Au+Au collisions in STAR (shown in the left column), freeze-out conditions of different orders of moments show very good agreement with each other except at lower  $\sqrt{s_{NN}}$ . For peripheral Au+Au collisions in STAR (shown in the middle column) and for the UrQMD model (shown in the right column) fits of different orders of moments give very different results, implying that thermalization is not seen.

band represents the error on  $p_T$  spectra corresponding to the uncertainty on  $T$ ,  $\mu_B$ ,  $\mu_S$ , and  $\mu_Q$  for 1-sigma contour obtained in the HRG model fit. The average radial flow velocities at  $\sqrt{s_{NN}} = 19.6$  and 200 GeV are found to be  $\langle\beta\rangle = 0.466c$  and  $0.58c$ , respectively.

If a distribution is thermal in nature, then all orders of its moments can be explained using a common set of thermodynamic parameters. This implies a comparison of the freeze-out conditions extracted from different orders of moments should serve as a detailed test of thermal behavior. Different sets of observables can be grouped as follows. The set of first-order cumulants *i.e.*, the mean yields,  $C_1^{\pi^\pm}$ ,  $C_1^{K^\pm}$ ,  $C_1^p$  and  $C_1^{\bar{p}}$ , set of the second order cumulants  $C_2^{NQ}/C_1^{NQ}$ ,  $C_2^{NK}/C_1^{NK}$ ,  $C_2^{NP}/C_1^{NP}$ , and  $C_{1,1}^{NP,NK}/C_2^{NK}$ , and the set of the third

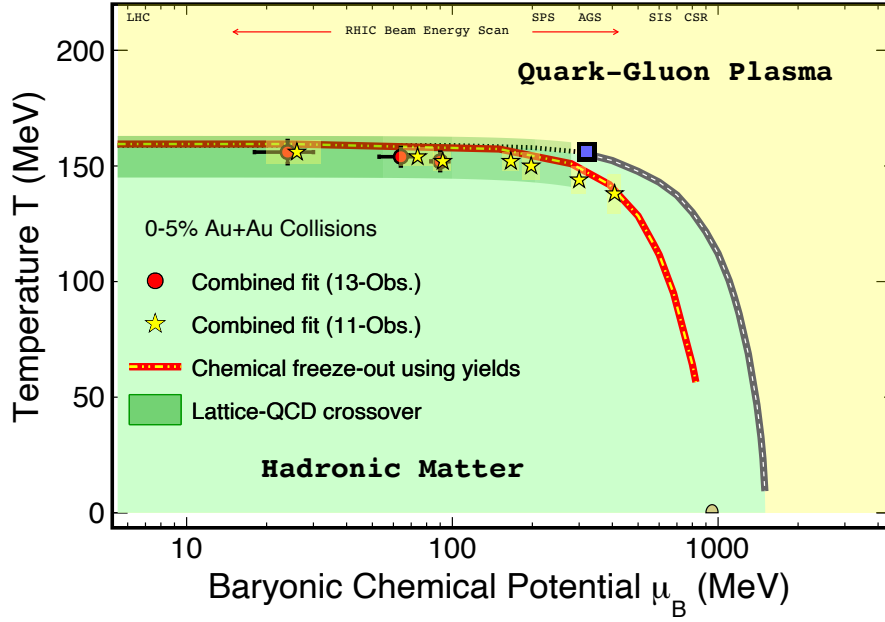


Figure 4.7: Freeze-out conditions in terms of temperature  $T$  and baryon chemical potential  $\mu_B$  for 0–5% most central Au+Au collision at  $\sqrt{s_{NN}} = 7.7\text{--}200$  GeV. The red circles show the  $T$  and  $\mu_B$  values obtained from thirteen observables fit while star markers represent those for eleven observables. Chemical freeze-out results using only hadron yield data are shown as dashed red line [19, 20]. Representing the smooth crossover region are the Lattice QCD results shown as green-band [48]. The dotted black line, blue square, and gray band represent the conjectured phase boundary in terms of crossover, speculated critical point, and first-order phase transition, respectively.

order cumulants  $C_3^{NQ}/C_2^{NQ}$ ,  $C_3^{NK}/C_2^{NK}$ , and  $C_3^{NP}/C_2^{NP}$ . For only this test, the  $\mu_s$  at each  $\sqrt{s_{NN}}$  is fixed to their values as published by the STAR experiment [7] and  $\mu_Q$  values are zero. The differences in the freeze-out parameters written as  $\Delta T$  and  $\Delta\mu_B$ , normalized by total uncertainty (errors added in quadrature), are shown in Figure 4.6.

Results for central and peripheral collisions at RHIC are shown in the left and middle panels, respectively. The right panel shows results for central collisions in the UrQMD model. For central collisions at RHIC, for  $\sqrt{s_{NN}} = 39$  GeV and above, the freeze-out parameters from different sets are in good agreement with each other within uncertainties. This suggests the matter produced in central Au+Au collisions at RHIC has attained

thermalization at least for  $\sqrt{s_{\text{NN}}} = 39$  GeV and above. Results for peripheral collisions at RHIC do not favor the thermal equilibrium scenario. Also, the disagreement of freeze-out parameters of different sets of observables for UrQMD central Au+Au collisions simulated data does not support a thermal picture.

Finally, Figure 4.7 shows a schematic presentation of the QCD phase diagram with the chemical freeze-out conditions extracted in our study.  $T$  and  $\mu_B$  from thirteen observables fit are shown for  $\sqrt{s_{\text{NN}}} = 200, 62.4$  and  $39$  GeV. Those from eleven observables fit are shown for  $\sqrt{s_{\text{NN}}} = 7.7\text{--}200$  GeV.  $T$  values in our study are lower compared to a parametrization of  $T$  and  $\mu_B$  obtained from the fit of only mean yields [19], however, are consistent within current uncertainties. The chemical freeze-out temperature is found to be close to the crossover temperature estimated in Lattice-QCD [48]. Freeze-out of fluctuations near the phase transition has important consequences for searches of QCD cross-over transition via experimental measurement of higher order moment of the fluctuations [12, 13].

## 4.6 Conclusion

We studied thermalization at the last scattering surface of the system formed in heavy-ion collisions at the RHIC for several collision energies. We found that by using a thermal gas of hadrons and resonances, a simultaneous description of measured mean yields, as well as several order moments of fluctuation is possible. This approach takes a stricter view of thermalization by investigating not only the peak regions but also the tails of the particle distributions. We found that this stricter definition helps bring clarity to the interpretation of chemical freeze-out parameters as thermal conditions. Observables included in this study are all cumulants up to the third order of the distribution of event-to-event fluctuations of various quantities in central Au-Au collisions. The fourth-order cumulants are used as

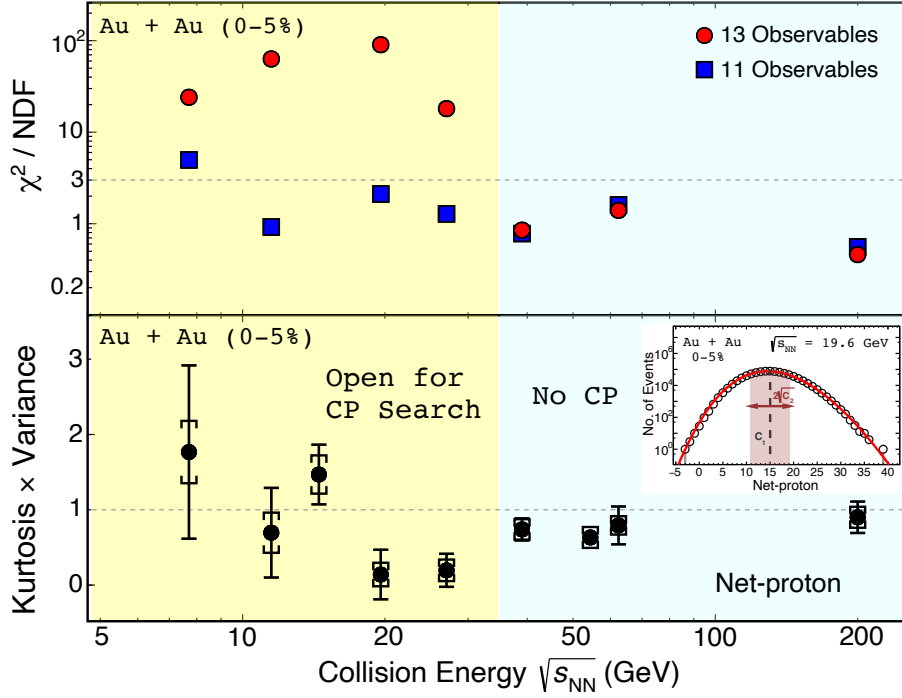


Figure 4.8: In the collision energy range at RHIC, this figure shows the regions where thermodynamic equilibrium can be verified at the chemical freeze-out surface and where it cannot. Collision energy  $\sqrt{s_{NN}}$  dependence of  $\chi^2/\text{NDF}$  obtained from the fits of thirteen observable sets listed in table 4.1 (shown with filled red circles) and the eleven observable sets (shown with filled blue squares). The lower panel shows the dependence on  $\sqrt{s_{NN}}$  of  $C_4/C_2 = \kappa\sigma^2$  for the net-proton distribution in the most central Au+Au collisions measured in the STAR experiment [4]. The inset shows the measured net-proton distribution for most central collisions at  $\sqrt{s_{NN}} = 19.6$  GeV. The red line corresponds to the statistical baseline of net-proton distribution known as the Skellam distribution. The color filling in both the top and bottom panels tentatively divides the range of collision energies into regions that are clearly in agreement with the predictions of an ideal gas of resonances, and therefore cannot contain the QCD critical point (labeled “No CP”) and one which is not in agreement with such a thermodynamic model, and therefore remains open for search. This is consistent with predictions from recent lattice QCD calculations which also disfavor the high energy region for the critical point search [49, 50].

independent checks of the results.

Our first observation is that commonly used transport model event generators show fluctuations that are not consistent with thermal behavior with stricter criteria. Similarly, fluctuations measured in peripheral heavy-ion collisions do not satisfy the stricter test for

thermalization. A detailed test for consistency of freeze-out parameters for different orders of moments (shown in Figure 4.6) imply non-thermal nature.

Our second observation is that in most central Au+Au collisions at the top three energies namely,  $\sqrt{s_{NN}} = 200, 62.4, \text{ and } 39 \text{ GeV}$ , the mean yields as well as fluctuations can be described using common thermodynamic conditions. This enables us to extract  $\mu_Q$  and  $\mu_S$  entirely from the experimental data. The extracted freeze-out conditions are also in good agreement with those obtained from mean yields of hadrons in previous studies [6]. At  $\sqrt{s_{NN}} = 200 \text{ GeV}$ , the freeze-out temperature  $T_{CFO} = 156 \pm 5 \text{ MeV}$  matches with the pseudo-critical temperature  $T_C(0) = 156.5 \pm 1.5 \text{ MeV}$  [51] estimated at  $\mu_B = 0$ , for QCD crossover in the lattice QCD. This agreement helps in the experimental search for signals of a crossover.

Our third observation is that at lower  $\sqrt{s_{NN}}$  a common thermal description of mean yields and fluctuations tends to fail. However, after the exclusion of net-proton higher moments, an effective thermal picture of the system is still possible by remaining observables. From these observations, we tentatively divide the range of collision energies in Figure 4.8 into two regions for the search for the QCD critical point. The collision energies where mean yields, as well as higher moments, can be described from pure thermal effects are labeled as “No CP” (the region of Figure 4.8 shade in cyan) region. The “Open for CP Search” region represents  $\sqrt{s_{NN}}$  values, where higher moments of protons tend to fall out of thermal equilibrium. In the inset of the bottom panel in Figure 4.8, a comparison of Skellam distribution with the measured net-proton distribution for  $\sqrt{s_{NN}} = 19.6 \text{ GeV}$  is shown. This reveals that the higher-order cumulants which are sensitive to the tails of a distribution are also sensitive probes of fluctuations away from equilibrium.

## Bibliography

- [1] Sourendu Gupta, Debasish Mallick, Dipak Kumar Mishra, et al. “Limits of thermalization in relativistic heavy ion collisions”. *Phys. Lett. B* 829 (2022), 137021.
- [2] L. Adamczyk et al. “Beam energy dependence of moments of the net-charge multiplicity distributions in Au+Au collisions at RHIC”. *Phys. Rev. Lett.* 113 (2014), 092301. arXiv: [1402.1558 \[nucl-ex\]](#).
- [3] L. Adamczyk et al. “Collision Energy Dependence of Moments of Net-Kaon Multiplicity Distributions at RHIC”. *Phys. Lett. B* 785 (2018), 551–560. arXiv: [1709.00773 \[nucl-ex\]](#).
- [4] J. Adam et al. “Nonmonotonic Energy Dependence of Net-Proton Number Fluctuations”. *Phys. Rev. Lett.* 126.9 (2021), 092301. arXiv: [2001.02852 \[nucl-ex\]](#).
- [5] Jaroslav Adam et al. “Collision-energy dependence of second-order off-diagonal and diagonal cumulants of net-charge, net-proton, and net-kaon multiplicity distributions in Au + Au collisions”. *Phys. Rev. C* 100.1 (2019). [Erratum: *Phys.Rev.C* 105, 029901 (2022)], 014902. arXiv: [1903.05370 \[nucl-ex\]](#).
- [6] J. Adams et al. “Identified particle distributions in pp and Au+Au collisions at  $\sqrt{s(NN)} = 200$  GeV”. *Phys. Rev. Lett.* 92 (2004), 112301. arXiv: [nucl-ex/0310004](#).
- [7] L. Adamczyk et al. “Bulk Properties of the Medium Produced in Relativistic Heavy-Ion Collisions from the Beam Energy Scan Program”. *Phys. Rev. C* 96.4 (2017), 044904. arXiv: [1701.07065 \[nucl-ex\]](#).
- [8] Frithjof Karsch and Krzysztof Redlich. “Probing freeze-out conditions in heavy ion collisions with moments of charge fluctuations”. *Phys. Lett. B* 695 (2011), 136–142. arXiv: [1007.2581 \[hep-ph\]](#).
- [9] P. Garg, D. K. Mishra, P. K. Netrakanti, et al. “Conserved number fluctuations in a hadron resonance gas model”. *Phys. Lett. B* 726 (2013), 691–696. arXiv: [1304.7133 \[nucl-ex\]](#).
- [10] M. Bleicher et al. “Relativistic hadron hadron collisions in the ultrarelativistic quantum molecular dynamics model”. *J. Phys. G* 25 (1999), 1859–1896. arXiv: [hep-ph/9909407](#).

- [11] Hannah Petersen, Marcus Bleicher, Steffen A. Bass, et al. “UrQMD v2.3: Changes and Comparisons” (May 2008). arXiv: [0805.0567 \[hep-ph\]](#).
- [12] Mohamed Abdallah et al. “Measurement of the Sixth-Order Cumulant of Net-Proton Multiplicity Distributions in Au+Au Collisions at  $\sqrt{s_{\text{NN}}} = 27, 54.4, \text{ and } 200 \text{ GeV}$  at RHIC”. *Phys. Rev. Lett.* 127.26 (2021), 262301. arXiv: [2105.14698 \[nucl-ex\]](#).
- [13] “Beam Energy Dependence of Fifth and Sixth-Order Net-proton Number Fluctuations in Au+Au Collisions at RHIC” (July 2022). arXiv: [2207.09837 \[nucl-ex\]](#).
- [14] B. Friman, F. Karsch, K. Redlich, et al. “Fluctuations as probe of the QCD phase transition and freeze-out in heavy ion collisions at LHC and RHIC”. *Eur. Phys. J. C* 71 (2011), 1694. arXiv: [1103.3511 \[hep-ph\]](#).
- [15] Misha A. Stephanov, K. Rajagopal, and Edward V. Shuryak. “Event-by-event fluctuations in heavy ion collisions and the QCD critical point”. *Phys. Rev. D* 60 (1999), 114028. arXiv: [hep-ph/9903292](#).
- [16] Rajiv V. Gavai. “The QCD critical point: an exciting Odyssey in the Femto-world”. *Contemp. Phys.* 57.3 (2016), 350–365.
- [17] George F. Smoot et al. “Structure in the COBE differential microwave radiometer first year maps”. *Astrophys. J. Lett.* 396 (1992), L1–L5.
- [18] E. Komatsu et al. “Seven-Year Wilkinson Microwave Anisotropy Probe (WMAP) Observations: Cosmological Interpretation”. *Astrophys. J. Suppl.* 192 (2011), 18. arXiv: [1001.4538 \[astro-ph.CO\]](#).
- [19] J. Cleymans, H. Oeschler, K. Redlich, et al. “Comparison of chemical freeze-out criteria in heavy-ion collisions”. *Phys. Rev. C* 73 (2006), 034905. arXiv: [hep-ph/0511094](#).
- [20] A. Andronic, P. Braun-Munzinger, and J. Stachel. “Hadron production in central nucleus-nucleus collisions at chemical freeze-out”. *Nucl. Phys. A* 772 (2006), 167–199. arXiv: [nucl-th/0511071](#).
- [21] F. Becattini, M. Gazdzicki, A. Keranen, et al. “Chemical equilibrium in nucleus nucleus collisions at relativistic energies”. *Phys. Rev. C* 69 (2004), 024905. arXiv: [hep-ph/0310049](#).

- [22] Anton Andronic, Peter Braun-Munzinger, Krzysztof Redlich, et al. “Decoding the phase structure of QCD via particle production at high energy”. *Nature* 561.7723 (2018), 321–330. arXiv: [1710.09425 \[nucl-th\]](#).
- [23] Francesco Becattini. “A Thermodynamical approach to hadron production in e+ e- collisions”. *Z. Phys. C* 69.3 (1996), 485–492.
- [24] F. Becattini and Ulrich W. Heinz. “Thermal hadron production in p p and p anti-p collisions”. *Z. Phys. C* 76 (1997). [Erratum: *Z.Phys.C* 76, 578 (1997)], 269–286. arXiv: [hep-ph/9702274](#).
- [25] Sabita Das, Debadeepti Mishra, Sandeep Chatterjee, et al. “Freeze-out conditions in proton-proton collisions at the highest energies available at the BNL Relativistic Heavy Ion Collider and the CERN Large Hadron Collider”. *Phys. Rev. C* 95.1 (2017), 014912. arXiv: [1605.07748 \[nucl-th\]](#).
- [26] A. Andronic, F. Beutler, P. Braun-Munzinger, et al. “Statistical hadronization of heavy flavor quarks in elementary collisions: Successes and failures”. *Phys. Lett. B* 678 (2009), 350–354. arXiv: [0904.1368 \[hep-ph\]](#).
- [27] A. Andronic, P. Braun-Munzinger, J. Stachel, et al. “Production of light nuclei, hypernuclei and their antiparticles in relativistic nuclear collisions”. *Phys. Lett. B* 697 (2011), 203–207. arXiv: [1010.2995 \[nucl-th\]](#).
- [28] Peter Braun-Munzinger and Johanna Stachel. “The quest for the quark-gluon plasma”. *Nature* 448 (2007), 302–309.
- [29] Francesco Becattini, Marcus Bleicher, Thorsten Kollegger, et al. “Hadron Formation in Relativistic Nuclear Collisions and the QCD Phase Diagram”. *Phys. Rev. Lett.* 111 (2013), 082302. arXiv: [1212.2431 \[nucl-th\]](#).
- [30] R. V. Gavai and Sourendu Gupta. “Lattice QCD predictions for shapes of event distributions along the freezeout curve in heavy-ion collisions”. *Phys. Lett. B* 696 (2011), 459–463. arXiv: [1001.3796 \[hep-lat\]](#).
- [31] A. Bazavov et al. “Freeze-out Conditions in Heavy Ion Collisions from QCD Thermodynamics”. *Phys. Rev. Lett.* 109 (2012), 192302. arXiv: [1208.1220 \[hep-lat\]](#).
- [32] S. Borsanyi, Z. Fodor, S. D. Katz, et al. “Freeze-out parameters from electric charge and baryon number fluctuations: is there consistency?” *Phys. Rev. Lett.* 113 (2014), 052301. arXiv: [1403.4576 \[hep-lat\]](#).

- [33] Adam Bzdak, Volker Koch, and Vladimir Skokov. “Baryon number conservation and the cumulants of the net proton distribution”. *Phys. Rev. C* 87.1 (2013), 014901. arXiv: [1203.4529 \[hep-ph\]](#).
- [34] Peter Braun-Munzinger, Krzysztof Redlich, and Johanna Stachel. “Particle production in heavy ion collisions” (Apr. 2003). Ed. by Rudolph C. Hwa and Xin-Nian Wang, 491–599. arXiv: [nucl-th/0304013](#).
- [35] K. A. Olive et al. “Review of Particle Physics”. *Chin. Phys. C* 38 (2014), 090001.
- [36] S. Chatterjee, R. M. Godbole, and Sourendu Gupta. “Strange freezeout”. *Phys. Lett. B* 727 (2013), 554–557. arXiv: [1306.2006 \[nucl-th\]](#).
- [37] R. Venugopalan and M. Prakash. “Thermal properties of interacting hadrons”. *Nucl. Phys. A* 546 (1992), 718–760.
- [38] Granddon D. Yen, Mark I. Gorenstein, Walter Greiner, et al. “Excluded volume hadron gas model for particle number ratios in A+A collisions”. *Phys. Rev. C* 56 (1997), 2210–2218. arXiv: [nucl-th/9711062](#).
- [39] S. Chatterjee, R. M. Godbole, and Sourendu Gupta. “Stabilizing hadron resonance gas models”. *Phys. Rev. C* 81 (2010), 044907. arXiv: [0906.2523 \[hep-ph\]](#).
- [40] Volodymyr Vovchenko, Mark I. Gorenstein, and Horst Stoecker. “van der Waals Interactions in Hadron Resonance Gas: From Nuclear Matter to Lattice QCD”. *Phys. Rev. Lett.* 118.18 (2017), 182301. arXiv: [1609.03975 \[hep-ph\]](#).
- [41] Subhasis Samanta and Bedangadas Mohanty. “Criticality in a Hadron Resonance Gas model with the van der Waals interaction”. *Phys. Rev. C* 97.1 (2018), 015201. arXiv: [1709.04446 \[hep-ph\]](#).
- [42] Sandeep Chatterjee, Debadepti Mishra, Bedangadas Mohanty, et al. “Freezeout systematics due to the hadron spectrum”. *Phys. Rev. C* 96.5 (2017), 054907. arXiv: [1708.08152 \[nucl-th\]](#).
- [43] V. V. Begun, Mark I. Gorenstein, M. Hauer, et al. “Multiplicity Fluctuations in Hadron-Resonance Gas”. *Phys. Rev. C* 74 (2006), 044903. arXiv: [nucl-th/0606036](#).

- [44] J. Adam et al. “Erratum: Collision-energy dependence of second-order off-diagonal and diagonal cumulants of net-charge, net-proton, and net-kaon multiplicity distributions in Au + Au collisions [Phys. Rev. C 100, 014902 (2019)]”. *Phys. Rev. C* 105.5 (2022), 029901.
- [45] Zi-Wei Lin, Che Ming Ko, Bao-An Li, et al. “A Multi-phase transport model for relativistic heavy ion collisions”. *Phys. Rev. C* 72 (2005), 064901. arXiv: [nucl-th/0411110](#).
- [46] Mikolaj Chojnacki, Adam Kisiel, Wojciech Florkowski, et al. “THERMINATOR 2: THERMal heavy IoN generATOR 2”. *Comput. Phys. Commun.* 183 (2012), 746–773. arXiv: [1102.0273 \[nucl-th\]](#).
- [47] S. S. Adler et al. “Identified charged particle spectra and yields in Au+Au collisions at  $S(NN)^{1/2} = 200$ -GeV”. *Phys. Rev. C* 69 (2004), 034909. arXiv: [nucl-ex/0307022](#).
- [48] A. Bazavov et al. “The chiral and deconfinement aspects of the QCD transition”. *Phys. Rev. D* 85 (2012), 054503. arXiv: [1111.1710 \[hep-lat\]](#).
- [49] Saumen Datta, Rajiv V. Gavai, and Sourendu Gupta. “Quark number susceptibilities and equation of state at finite chemical potential in staggered QCD with  $N_t=8$ ”. *Phys. Rev. D* 95.5 (2017), 054512. arXiv: [1612.06673 \[hep-lat\]](#).
- [50] A. Bazavov et al. “The QCD Equation of State to  $\mathcal{O}(\mu_B^6)$  from Lattice QCD”. *Phys. Rev. D* 95.5 (2017), 054504. arXiv: [1701.04325 \[hep-lat\]](#).
- [51] A. Bazavov et al. “Chiral crossover in QCD at zero and non-zero chemical potentials”. *Phys. Lett. B* 795 (2019), 15–21. arXiv: [1812.08235 \[hep-lat\]](#).

# Chapter 5

## Summary and Conclusions

In this thesis, we present some interesting results of the first measurements of higher order moments of deuteron fluctuations and proton-deuteron correlation in Au+Au collisions at  $\sqrt{s_{\text{NN}}} = 7.7, 11.5, 14.5, 19.6, 27, 39, 54.4, 62.4,$  and 200 GeV using the STAR detector at RHIC and the study on the test of thermalization of the matter formed in heavy-ion collisions. The first set of results corresponds to the study to probe the production mechanism of deuterons in heavy-ion collisions and to search for a critical point in the QCD phase diagram. The data set used for this study was taken with the STAR detector at RHIC from the year 2010 to 2017 as phase-I of the Beam Energy Scan program covering a wide range of baryon chemical potential ( $\mu_B \sim 20$  MeV to 420 MeV) in the QCD phase diagram. Deuterons were identified using the STAR TPC and TOF detectors. Cumulants (up to 4<sup>th</sup> order) of event-by-event deuteron distributions were presented as a function of collision energies and centralities. For any given centrality of the collision, as the collision energy decreases the mean, variance, and higher-order cumulants of the deuteron number are enhanced. This is due to the fact that the baryon density or baryon chemical potential is enhanced as colliding energy is decreased. Similarly, for any given collision energy,

cumulants of all order of deuteron number increase as the collision centrality change from being peripheral to central, reflecting the associated increase in the energy/baryon density deposition in the initial state of a collision. Cumulant ratios *i.e.*  $\kappa\sigma^2$ ,  $S\sigma$ , and  $\sigma^2/M$  in higher  $\sqrt{s_{\text{NN}}}$  are found to be close to Poissonian and grand-canonical thermal model baselines. However, in central and mid-central collisions, for  $\sqrt{s_{\text{NN}}} \leq 20$  GeV, these ratios show suppression with respect to the Poisson baseline (unity) and the grand-canonical thermal model calculations. The suppression is predicted by a canonical ensemble of the thermal model which implements the baryon number conservation. A transport model (UrQMD) combined with a phase-space coalescence mechanism also predicts the collision energy dependence of these ratios. This highlights the fact that the effects of baryon number conservation are important for fluctuation measurements in low-energy collisions. Results for most peripheral (70-80%) collisions do not show any dependence with  $\sqrt{s_{\text{NN}}}$  and are always close to unity.  $\kappa\sigma^2$  of deuterons in 0-5% most central collisions show a smooth dependence with  $\sqrt{s_{\text{NN}}}$  in contrast to that observed for protons (proton  $\kappa\sigma^2$  shows a non-monotonic energy dependence with  $3.1\sigma$  statistical significance). Even though a deuteron carries two baryons, higher moments of deuteron number fluctuation might not be sensitive to a possible critical point.

In addition, we present results on the proton-deuteron correlation measured by the Pearson correlation coefficient for 0-5% and 70-80% Au+Au collisions at  $\sqrt{s_{\text{NN}}} = 7.7$  to 200 GeV. We observe an anti-correlation between proton and deuteron numbers for all collision energies and centralities presented. The anti-correlation is the strongest in central 0-5% collisions and becomes increasingly negative as  $\sqrt{s_{\text{NN}}}$  decreases. A thermal model with a grand-canonical ensemble fails to predict the observed anti-correlation between proton and deuteron. In canonical ensemble, the thermal model calculation correctly predicts the sign and energy dependence trend of the correlation. A simple statistical simulation of the

coalescence process (which does not take into account the phase space density information of nucleons and the effect of baryon number conservation) also does not predict the observed magnitude of the anti-correlation. On the other hand, the UrQMD+coalescence model calculations match well with the experimental data in central 0-5% collisions. This suggests that the phase-space density information of constituent nucleons and baryon number conservation are important for the deuteron formation process in the coalescence picture. Within current uncertainties on the measurements, both the UrQMD+coalescence model and canonical ensemble thermal model are able to fairly predict the measurements on cumulants up to 4<sup>th</sup> order and proton-deuteron correlation. Further, utilizing our experimental measurements, we extract the volume parameter in a canonical ensemble over which baryon number conservation is imposed. The volume parameter  $V_c$  varies between  $2dV/dy$  at the lowest energy ( $\sqrt{s_{NN}} = 7.7$  GeV) to  $4dV/dy$  at the topmost RHIC collision energy ( $\sqrt{s_{NN}} = 200$  GeV).

Our measurements can be utilized further to study the chemical freeze-out thermodynamics of deuterons and to constrain the light nuclei production model parameters. In the future, with higher event statistics and improved acceptance,  $p_T$  and rapidity differential measurements of light nuclei fluctuation and hadron-nuclei correlation with better statistical and systematic precision are possible in the STAR experiment. This will improve the nature of comparison with model calculations to resolve the nuclei production puzzle in high-energy heavy-ion collisions.

The next set of results we presented corresponds to the study of thermalization in high-energy heavy-ion collisions. By utilizing a large set of measurements of higher order cumulants (starting from the mean up to 4<sup>th</sup> order) of net-proton, net-kaon, and net-charge distributions and correlations, we studied the chemical freeze-out thermodynamics of the system created in Au+Au collisions for  $\sqrt{s_{NN}} = 7.7$  to 200 GeV. First, we compare results of

cumulant ratios from the transport models to corresponding susceptibility ratios calculated in a thermal model and observe that the fluctuations are not consistent with thermal behavior with stricter criteria. Similarly, fluctuations measured in peripheral heavy-ion collisions do not satisfy the stricter test for thermalization.

Our second observation is that at the top three collision energies namely,  $\sqrt{s_{\text{NN}}} = 200$ , 62.4, and 39 GeV for the system formed in central Au+Au collisions, the mean yields as well as fluctuations can be described using common thermodynamic conditions. We extract freeze-out conditions  $T$ ,  $\mu_B$ ,  $\mu_S$ , and  $\mu_Q$  that are also in good agreement with those obtained from mean yields of hadrons in previous studies. It is worth noting that at  $\sqrt{s_{\text{NN}}} = 200$  GeV, the chemical freeze-out temperature  $T_{ch} = 156$  MeV matches with the pseudo-critical temperature  $T_C(0) = 156$  MeV estimated at  $\mu_B = 0$ , for QCD crossover in the lattice QCD. This agreement suggests that the crossover from QGP to the hadronic phase happens near the chemical freeze-out of the system and therefore the signals of crossover might be observed in the experiment.

Further, we observe that at lower  $\sqrt{s_{\text{NN}}}$  a common thermal description of mean yields and fluctuations tends to fail. For  $\sqrt{s_{\text{NN}}} \leq 27$  GeV, even though higher moments of net-proton seem to fall out of thermal equilibrium, an effective thermodynamic description is still possible with remaining observables. From these observations, we tentatively divide the range of collision energies in BES-I into two regions: one where mean yields, as well as higher moments, can be described from pure thermal equilibrium effects and the other where higher moments of protons tend to fall out of thermal equilibrium. Departures from thermodynamic equilibrium in the final state are interesting and open up new directions in the search for a QCD critical point.